

Università degli Studi di Bologna

FACOLTÀ DI SCIENZE MATEMATICHE, FISICHE E NATURALI

Dipartimento di Astronomia

**THE SCALING RELATIONS
OF ELLIPTICAL GALAXIES:
CONSTRAINTS FROM
STELLAR DYNAMICS**

CARLO NIPOTI

Supervisore: **Prof. GIANCARLO SETTI**

Correlatori: **Prof. LUCA CIOTTI**

Dott. PASQUALE LONDRILLO

Coordinatore: **Prof. GABRIELE GIOVANNINI**

DOTTORATO DI RICERCA IN ASTRONOMIA

XV CICLO [1999–2002]

Università degli Studi di Bologna

FACOLTÀ DI SCIENZE MATEMATICHE, FISICHE E NATURALI

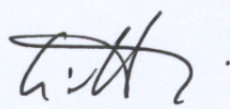
Dipartimento di Astronomia

THE SCALING RELATIONS OF ELLIPTICAL GALAXIES: CONSTRAINTS FROM STELLAR DYNAMICS

CARLO NIPOTI

Supervisore: Prof. GIANCARLO SETTI

Correlatori: Prof. LUCA CIOTTI



Dott. PASQUALE LONDRILLO

Coordinatore: Prof. GABRIELE GIOVANNINI

DOTTORATO DI RICERCA IN ASTRONOMIA

XV CICLO [1999–2002]

Università degli Studi di Bologna

FACOLTÀ DI SCIENZE MATEMATICHE, FISICHE E NATURALI

Dipartimento di Astronomia

**THE SCALING RELATIONS
OF ELLIPTICAL GALAXIES:
CONSTRAINTS FROM
STELLAR DYNAMICS**

CARLO NIPOTI

Supervisore: **Prof. GIANCARLO SETTI**

Correlatori: **Prof. LUCA CIOTTI**

Dott. PASQUALE LONDRILLO

Coordinatore: **Prof. GABRIELE GIOVANNINI**

DOTTORATO DI RICERCA IN ASTRONOMIA

XV CICLO [1999–2002]

Where was the chap I saw in that picture somewhere? Ah, in the dead sea, floating on his back, reading a book with a parasol open. Couldn't sink if you tried: so thick with salt. Because the weight of the water, no, the weight of the body in the water is equal to the weight of the. Or is it the volume is equal of the weight? It's a law something like that.

James Joyce, "Ulysses"

Contents

Abstract	V
1. Introduction	1
1.1 Scaling laws of ellipticals and galaxy formation scenarios	2
1.2 Effects of radial orbital anisotropy on the projected central velocity dispersion	3
1.3 Radial orbital anisotropy and the Fundamental Plane	4
1.4 Dissipationless merging and the scaling relations of ellipticals	5
1.5 Formation of Brightest Cluster Galaxies	7
2. Empirical scaling relations of elliptical galaxies	9
2.1 The Fundamental Plane	9
2.2 The Faber-Jackson relation	11
2.3 The Kormendy relation	13
2.4 The $M_{\text{BH}}\text{-}\sigma_0$ and the Magorrian relations	14
3. Galaxy models	17
3.1 One-component models	17
3.2 Two-component models	18
3.3 Physical scales	19
4. The numerical method	23
4.1 Computational methods for collisionless systems	23
4.2 N -body codes used for our simulations	25
4.2.1 The Barnes & Hut tree-code	26
4.2.2 GADGET	27
4.2.3 FVFPS: a parallel implementation of Dehnen's $O(N)$ force algorithm	29
4.3 Choosing the parameters of the codes	33
4.3.1 The softening length	33
4.3.2 The time-step	34

4.3.3	The opening parameter	36
4.4	Numerical tests	37
4.4.1	Isolated one-component $\gamma = 1$ model	37
4.4.2	Merging of two $\gamma = 1$ models	39
4.4.3	Performance of the FVFPS code	41
5.	Radial orbital anisotropy and the Fundamental Plane of elliptical galaxies	47
5.1	Introduction	47
5.2	Numerical simulations	50
5.3	Orbital anisotropy and the FP thinness	51
5.3.1	One-component models	53
5.3.2	Two-component models	58
5.4	Orbital anisotropy and the FP tilt	60
5.4.1	One-component models	61
5.4.2	Two-component models	63
5.5	Discussion and conclusions	63
6.	Galaxy merging, the Fundamental Plane of elliptical galaxies, and the $M_{\text{BH}}\text{-}\sigma_0$ relation	65
6.1	Introduction	65
6.2	Numerical simulations	67
6.2.1	Initial conditions	68
6.3	The results: equal mass merging	69
6.3.1	Fundamental Plane	71
6.3.2	Faber–Jackson and Kormendy relations	73
6.4	The results: accretion	75
6.4.1	Fundamental Plane	76
6.4.2	Faber–Jackson and Kormendy relations	76
6.5	Dissipationless merging and the $M_{\text{BH}}\text{-}\sigma_0$ relation	77
6.6	Discussion and conclusions	80
7.	Galactic cannibalism in the galaxy cluster C0337-2522 at $z \simeq 0.59$	83
7.1	Introduction	83
7.2	Observations and data reduction	85
7.3	Models	85

7.4	Numerical simulations	86
7.4.1	Initial conditions	86
7.4.2	Numerical methods	89
7.5	Results: merging statistics and time-scales	89
7.6	Results: properties of the end-products	93
7.6.1	Structural and dynamical parameters	94
7.6.2	Surface brightness profiles	95
7.6.3	Fundamental Plane and Faber–Jackson relations	96
7.7	Multiple merging and the $M_{\text{BH}}\text{-}\sigma_0$ relation	99
7.8	Metallicity gradients	102
7.9	Discussion and conclusions	103
8.	Conclusions	107
	Appendix	113
A.1	Numerical realization of the Osipkov-Merritt models	113
A.2	Diagnostics of the numerical simulations end-products	114
A.3	Surface brightness profiles fitting	118
	Acknowledgments	121
	Bibliography	123
	Related publications	129

Abstract

The scaling relations of elliptical galaxies (Es) are expected to impose strong constraints on their structure and dynamics, and thus to contain important information on the processes of galaxy formation and evolution. In the present work we explore whether a few mechanisms, which are supposed to have an important role in the formation of Es, are actually compatible with their global scaling laws.

We first focus on the relations between the Fundamental Plane (FP) and the amount of *radial orbital anisotropy* in Es. By using N -body simulations, we explore the impact of radial orbital anisotropy on the FP thickness and tilt, also considering the presence of galactic dark matter (DM) halos. The numerical results indicate that the observed FP thickness is compatible with whatever spread of radial orbital anisotropy in Es, when the effects of *radial orbit instability* is taken into account. In addition, we find that a systematic increase of radial orbital anisotropy with galaxy luminosity cannot explain by itself the whole FP tilt.

As a second investigation, we explore the effects of *dissipationless* merging on the FP and other scaling laws of Es. With the aid of N -body simulations, we consider the two extreme cases of galaxy growth by *accretion* of small stellar systems and *equal mass merging*, both with and without DM. Curiously, we find that the FP is preserved by major merging, while the accretion scenario is only marginally compatible with the edge-on FP thickness. In any case, the Faber-Jackson and Kormendy relations are *not* reproduced. In addition, we find that dissipationless merging is unable to reproduce the $M_{\text{BH}}\text{-}\sigma_0$ relation, if black hole (BH) masses add linearly; on the contrary, BH merging with substantial emission of gravitational waves is consistent with the $M_{\text{BH}}\text{-}\sigma_0$ relation, but violates the Magorrian relation.

Finally, we consider a concrete example of Brightest Cluster Galaxy (BCG) formation through *galactic cannibalism*. We have identified a candidate for the early stage of this process: a group of five Es in the core of the cluster C0337-2522 at $z \simeq 0.59$. On the basis of our ESO-VLT data, and using N -body simulations, we study the dynamical evolution of this system up to $z = 0$, for reasonable assumptions on the cluster structure and dynamics. We find that a multiple merging event will take place in the next few Gyrs. The merger remnant will be similar in its main properties to the observed BCGs (without cD halo). In particular, this multiple merging process is expected to preserve the FP and (marginally) the Faber-Jackson relation, while its behavior with respect to the $M_{\text{BH}}\text{-}\sigma_0$ relation is quite sensitive to the details of BH merging.

As a whole, our results point towards a major role of *dissipation* in the formation of normal Es and in the growth of their central supermassive BHs. On the other hand, it seems reliable that BCGs are the end-product of a few (dissipationless) merging events.

The numerical simulations cited above require high resolution, and thus an efficient N -body code. For this reason, we have implemented in a parallel Fortran-90 N -body code, the algorithms recently proposed by W. Dehnen, resulting in a fast and accurate Poisson solver, with effective $O(N)$ computational complexity. We use this code in most of our simulations.

1. Introduction

Elliptical galaxies are a remarkably regular family of stellar systems. They are quite similar in their main structural and dynamical properties, as apparent from both photometric and spectroscopic observations. However, a more detailed analysis reveals that many relevant observable quantities of ellipticals (hereafter Es) depend systematically on some of their global properties, such as their total mass or luminosity. In other words, Es satisfy a few *empirical scaling relations*, among which the most studied, and probably the most important, is the Fundamental Plane relation (hereafter FP; Djorgovski & Davis 1987, Dressler et al. 1987).

Clearly, the very uniform nature of Es strongly suggests a common formation history for this family of astrophysical objects. In any case, every scenario proposed for the formation of Es must also be able to reproduce *all* their observed scaling laws. In other words, it is necessary that the involved formation mechanisms produce a systematic variation of the galactic properties from the small to the large scales. Of course, this is definitely not a trivial requirement, because the scaling relations are expected to put strong constraints on the galaxy structure and dynamics.

Taking into account the considerations above, in the present work we try to gain new insights on the complex question of elliptical galaxy formation. Adopting the point of view of stellar dynamics, and with the aid of N -body numerical simulations, we will explore whether a few mechanisms (which are supposed to have an important role in the formation process of Es) are actually compatible with their global scaling laws. In particular, the main goal of our research is to investigate whether a major role of *hierarchical dissipationless merging* in elliptical galaxy formation can be reconciled with the very existence of the FP and with other empirical scaling relations. As a preliminary, strictly related problem, we will also study the interplay between the FP and the *orbital anisotropy* in the internal dynamics of Es, also considering the effects of radial orbit instability. Finally, with a specific, concrete example of *galactic cannibalism*, we will explore whether multiple dissipationless merging is a viable mechanism for the formation of the peculiar Brightest Cluster Galaxies (BCGs), and in particular cD galaxies, observed in the center of galaxy clusters.

Before introducing our research in more detail, in the following Sections we will outline what are the scenarios proposed for the formation of Es. In addition, we will recall the main characteristics of a few relevant empirical scaling relations of Es, which are of interest for the present work. Some of the questions raised when interpreting these scaling laws in the context of stellar dynamics are also discussed below.

1.1 Scaling laws of ellipticals and galaxy formation scenarios

Elliptical galaxy formation scenarios

Two distinct scenarios have been proposed to describe the formation of Es. Roughly speaking, according to the *monolithic scenario* each elliptical galaxy is formed at high redshift as a consequence of the dissipative collapse of a huge mass of gas. During this collapse the galaxy experiences a single, enormous burst of star formation, in which all of its stars are formed (see, e.g., Eggen, Lynden-Bell & Sandage 1962, Larson 1975). On the other hand, in the *hierarchical merging scenario* spheroidal systems are the end-products of several merging processes of smaller galaxies, the last major merger occurring in relatively recent times, i.e., at $z \lesssim 1$. In this latter picture the stars are produced in different episodes of star formation, taking place in the various sub-units, and then assembled through dissipationless merging of stellar systems already formed (see, e.g., White & Rees 1978, Baugh, Cole & Frenk 1996, Kauffmann 1996).

Of course this distinction is too rough, as galaxy formation is a very complex process, including both mass assembly and star formation, and is strictly interwoven with galaxy evolution. For this reason, even the definition of the epoch of formation of a galaxy is not unambiguous in the literature. In some cases the time of formation of the stars is considered, while in other cases the time of mass assembly. It has been suggested to define the epoch of formation of a galaxy as the time at which occurs “the assembly of more than half the material now in the luminous parts of a galaxy” (Peebles 2002). Thus, it seems that a more interesting and meaningful distinction is between scenarios in which merging has a substantial role in the assembly of most of the stellar mass of the galaxies up to relatively low redshift, and scenarios in which galaxies evolve mainly as isolated systems, and interaction and merging events are rare, and can be considered as perturbations during their lifetime.

Observed scaling relations

As outlined above, we know from an observational point of view that Es satisfy several (more or less tight) scaling relations. The FP relation, already mentioned, involves their circularized effective radius, mean effective surface brightness, and central velocity dispersion, and is characterized by a remarkably small scatter. The Faber–Jackson relation (hereafter FJ, Faber & Jackson 1976) and the Kormendy relation (Kormendy 1977) indicate that the galaxy luminosity increases systematically as a function of the central velocity dispersion, and of the circularized effective radius, respectively. Even the characteristics of the stellar populations of Es (such as their age and metallicity) are strictly correlated with their total luminosity and internal dynamics, as shown by the color–magnitude relation (Bower, Lucey & Ellis 1992) and by the $M_{g_2}-\sigma_0$ relation (see, e.g., Burstein et al. 1988, Bender, Burstein & Faber 1993). In addition, it is now widely accepted that central supermassive black holes (hereafter BHs) are a common characteristic of spheroidal stellar systems (see, e.g., Kormendy & Richstone 1995, van der Marel 1999, de Zeeuw 2001). It has also been found that their mass (M_{BH}) is linearly proportional to the stellar mass (luminosity) of the host galaxy or bulge (the so-called Magorrian

relation; Magorrian et al. 1998), and it is even more correlated with the spheroid central stellar velocity dispersion through the $M_{\text{BH}}\text{-}\sigma_0$ relation (Gebhardt et al. 2000, Ferrarese & Merritt 2000).

Structural and dynamical constraints from the scaling laws

The existence of the scaling laws cited above is of great importance in the context of galaxy formation and evolution studies. The fact that they break the scale-free nature of gravity indicates that they contain clues on the not purely dynamical mechanisms responsible for galaxy formation and evolution (see, e.g., Bertin 2000, and reference therein). In other words, a dynamical theory is unable to predict, for example, whatever correlation between mass and length scales, or mass and velocity scales, as instead observed in real galaxies. Therefore, it should be clear that the global scaling laws of Es are teaching us something about how these stellar systems were formed and evolved in a cosmological context.

Thus, in principle, we can use these global laws as powerful tests for whatever proposed galaxy formation scenario, because they constrain the galactic structure and dynamics. In particular, some of the quantities involved in the scaling relations of Es (namely the circularized effective radius and the projected central velocity dispersion) are related, in a more or less complex way, to their intrinsic structural and dynamical properties. It is remarkable that these parameters are tightly coupled, through the cited scaling laws, to other quantities (such as the galaxy luminosity and metallicity) in principle independent of the galactic structure and dynamics, and instead sensitive to the properties of the stellar populations. At the present moment, from a theoretical point of view, no simple physical reasons are known for which these correlations should be expected. In fact, it is recognized that the proposed galaxy formation models are not able to produce *all* these features as natural consequences of reasonable basic assumptions.

1.2 Effects of radial orbital anisotropy on the projected central velocity dispersion

How non-homology can influence the projected central velocity dispersion

Due to its important role in many of the observed scaling relations of Es (namely, the $\text{Mg}_2\text{-}\sigma_0$, the FP, the FJ, and the $M_{\text{BH}}\text{-}\sigma_0$ relations), their *projected central velocity dispersion* σ_0 is a very interesting quantity to be studied in the picture presented above. It is well known that σ_0 in principle can be *strongly* dependent on both the dynamical and structural properties of the galaxies. For example, the central velocity dispersion of structurally homologous spherical stellar systems can be affected by *dynamical non-homology*, i.e., by the presence of *orbital anisotropy* in the stellar velocity distribution. At fixed virial velocity dispersion, radially and tangentially anisotropic systems have, respectively, higher and lower σ_0 , with respect to systems with the same structure, but with isotropic velocity dispersion tensor. On the other hand, also *structural non-homology* can affect σ_0 : if two systems have different structure *then* they have different internal dynamics. In other words, structural non-homology necessarily implies dynamical non-homology. In addition, we note

that σ_0 depends also on the aperture used in its measure and, if non spherically symmetric stellar systems are considered, on the line-of-sight direction, i.e., it is sensitive to projection effects. Of course, this makes still more striking the existence of *tight* scaling relations involving σ_0 .

Radial orbital anisotropy and radial orbit instability

We know from observations that *radial* orbital anisotropy is a more common feature in luminous Es than *tangential* orbital anisotropy (see, e.g. Gerhard et al. 2001). In addition, radial orbital anisotropy in the outer parts of Es is also predicted, from a theoretical point of view, by studies of the dynamical processes that could lead to the formation of Es, both in case of dissipationless collapse (see, e.g., van Albada 1982) and in case of merging between pairs of galaxies (see, e.g., Barnes 1992, Hernquist 1993). For these reasons, in the present work we focus on radially anisotropic galaxies.

As already pointed out, stellar systems (even structurally homologous and with the same virial velocity dispersion) with a spread in the amount of radial orbital anisotropy can span a wide range in central velocity dispersion. On the other hand, the existence of the previously cited scaling relations involving σ_0 , and in particular of the FP, characterized by a very small scatter, tells us that galaxies of similar luminosity cannot have very different amount of radial anisotropy. A natural question to be addressed is then what physical principle or evolutionary process limits the range of orbital anisotropies shown by real galaxies. It has been suggested that *radial orbit instability* could be the limiting factor of the FP thickness (Ciotti & Lanzoni 1997): indeed, many studies have shown that strongly radially anisotropic stellar systems are actually unstable (see, e.g., Fridman & Polyachenko 1984, Bertin et al. 1994, and references therein).

1.3 Radial orbital anisotropy and the Fundamental Plane

Radial orbital anisotropy and the Fundamental Plane thickness

A first point we want to address in this work is whether the presence of a substantial spread in radial orbital anisotropy, among Es of similar luminosity, is compatible with the observed small *thickness* of the FP. We stress that in this kind of analysis we will take explicitly into account the effects of radial orbit instability. In particular, assuming that isotropic galaxies lie on the FP, we want to compare the deviation of *stable* anisotropic galaxies from the edge-on FP, with the observed FP scatter. In addition, since unstable radially anisotropic stellar systems, after the onset of instability, evolve into new stable configurations, we want to study the behavior of these end-products with respect to the FP. Clearly, in order to address the previous questions, we have to consider self-consistent radially anisotropic galaxy models and N -body numerical simulations are needed to determine whether the studied models are stable and, in case they are not, to know the properties of their end-products.

Radial orbital anisotropy and the Fundamental Plane tilt

A strictly related problem is the existence of the so-called FP *tilt*, which in principle can be ascribed to a few different effects. Possible causes of the tilt are a dependence on galaxy luminosity of the stellar mass-to-light ratio, a systematic variation in structural and/or dynamical non-homology, or a combination of these two effects (see, e.g., Renzini & Ciotti 1993). It is interesting to explore the possibility that the tilt is due *only* to structural and/or dynamical non-homology, especially when considering a *dissipationless* merging scenario of galaxy formation (where, by definition, the stellar mass-to-light ratio is independent of galaxy luminosity). Thus, as a preliminary investigation, we focus on the hypothesis that the FP tilt is a consequence of purely dynamical non-homology due to a systematic increase of radial orbital anisotropy with galaxy luminosity, again taking into account the limits posed by radial orbit instability, with the aid of N -body simulations.

1.4 Dissipationless merging and the scaling relations of ellipticals

Galaxy merging and the Fundamental Plane

It should be clear that the problem posed by the explanation of the observed amount of radial orbital anisotropy is important for all the proposed mechanisms of Es formation. However, this is not the only problem to be faced in this context: the existence of the scaling relations of Es raises specific problems for each particular galaxy formation scenario. For example, a natural question to ask is how well *dissipationless merging* is able to produce and maintain these relations. In the present work we consider merging without dissipation, so that we can check whether gas dissipation is necessary in a picture in which Es are built mainly through combination of smaller systems. In addition, we recall that a few merging episodes between gas poor early-type galaxies have been observed at $z < 1$ (as in the cluster MS 1054-03, van Dokkum et al. 1999). Again we concentrate first on the FP, because it is a very tight correlation and involves galaxies in a large range of luminosity. In practice, we would like to investigate whether the end-products of merging of galaxies, initially lying on the FP, lie on the FP (in a line of work already started; see, e.g., Pentericci, Ciotti & Renzini 1995; Capelato, de Carvalho & Carlberg 1995; Bekki 1998; Evstigneeva, Reshetnikov & Sotnikova 2002). As well as in the study of radial orbit instability, also in this case N -body numerical simulations are needed, because, owing to possible structural and/or dynamical non-homology and to projection effects, one cannot predict with simple theoretical arguments how the (projected) circularized effective radius and central velocity dispersion evolve as consequence of merging.

Major and minor mergers

According to the hierarchical merging scenario, the luminous Es observed today are the end-products of a substantial number of both *major* and *minor mergers*¹ (see, e.g., Baugh et al. 1996, Kauffmann 1996). In principle, there is no reason to expect that hierarchies of major and minor mergers produce similar effects on the galactic structure and dynamics² (and then similar effects on some of the quantities involved in the observed scaling relations). Thus, in every investigation of the hierarchical merging scenario it is fundamental to explore both kinds of mergers. In particular, in the present work, we consider the two extreme situations of a hierarchy of *equal mass mergings* and a hierarchy of *accretion* of small stellar systems. These explorations should bracket a more realistic history of major and minor mergers, giving a quite fair picture of the effects of a merging hierarchy on the scaling relations of Es.

Galaxy merging, the Faber–Jackson and the Kormendy relations

We recall here that the preservation of the FP, though certainly a strong requirement, is by far not a sufficient test for the dissipationless merging scenario. Indeed, the fact that a galaxy lies on the FP (i.e., satisfies the edge-on FP relation) does not imply that it follows the FJ and the Kormendy relations too. The two latter scaling relations, though often considered simple projections of the FP, of course contain additional information with respect to the edge-on view of the FP, as they are also related to the distribution of the galaxies within the FP (i.e., to its face-on view). Therefore, the FJ and Kormendy relations need a separate investigation in our study. In practice, we want to verify whether these two relations, as well as the FP relation, are closed with respect to dissipationless merging, i.e., if the end-products of a merging hierarchy, whose seed galaxies satisfy the FJ and the Kormendy relations, follow these two scaling relations, as well.

Galaxy merging, the $M_{\text{BH}}\text{-}\sigma_0$ and the Magorrian relations

A specific discussion is necessary for the investigation, in the context of hierarchical merging, of the empirical relations involving the mass of the central supermassive BH, such as the very tight $M_{\text{BH}}\text{-}\sigma_0$ relation and the Magorrian relation. As a starting point, we can make the observationally motivated assumption that each merging galaxy contains a central supermassive BH with mass such that the $M_{\text{BH}}\text{-}\sigma_0$ and Magorrian relations are satisfied. In this picture, when two galaxies merge their BHs are expected to spiral, owing to the dynamical friction against the surrounding stellar sea, towards the center of the merger remnant, where they form a BH binary. Then the binary hardens as a consequence of the interaction with the background stars, and eventually the two BHs coalesce via emission of gravitational waves (Begelman, Blanford & Rees 1980). In this picture, it could seem natural that the mass of the central BH increases with the stellar mass of the host galaxy or

¹From a quantitative point of view, a merger is usually defined major when the mass ratio between the involved objects exceeds 1/3, and minor otherwise.

²Interestingly, Subramanian, Cen & Ostriker (2000), and Ricotti (2002) find that the details of the merging history strongly influence the density profiles of dark matter halos in hierarchical structure formation scenarios.

bulge. On the other hand, no simple predictions can be done on the $M_{\text{BH}}\text{-}\sigma_0$, due to the uncertainties on the evolution of σ_0 in galaxy merging, discussed above. In any case, some important effects have to be taken into account. The mass of the final BH depends critically on the amount of energy emitted as gravitational waves during BH merging (see, e.g., Flanagan & Hughes 1998). In addition, the BHs can be expelled from the galaxy as a consequence of the kick velocity or for the so-called slingshot effect (see, e.g., Ciotti & van Albada 2001 and reference therein). All these problems make difficult to understand the connection between the scaling relations involving the mass of the central BH and galaxy merging, mainly because merging between BHs is still a poorly understood physical process. In particular, open problems are the determination of the characteristic time of BH merging (Yu 2002), and the effect of BH binaries on the inner stellar density profiles (Milosavljevic & Merritt 2001). Aware of all these uncertainties (and although our galaxy models *do not* contain central BHs), we will try to obtain from our N -body simulations some indications about the effects of dissipationless merging on the $M_{\text{BH}}\text{-}\sigma_0$ and the Magorrian relations.

1.5 Formation of Brightest Cluster Galaxies

Multiple merging and the formation of Brightest Cluster Galaxies

Clearly, denser environments (such as galaxy clusters) are the preferred locations for galaxy interactions. However, a high interaction rate does not necessarily imply a high merging rate, because galaxy density is only one of the factors determining the merging rate. In particular, many galaxy encounters in clusters, being characterized by relative velocities higher than the galaxy internal velocity dispersion, do not lead to merging, but to the tidal disruption of the involved galaxies. In fact, it is well known that the velocity dispersion is significantly lower in galaxies than in clusters. However, the dynamical friction of the galaxies against the diffuse cluster dark matter can be effective in reducing the galaxy velocity in clusters, leading to low relative velocity encounters, and eventually to galaxy mergers. In this picture, the core of galaxy clusters are expected to host *multiple merging* events. Therefore, a natural application of our research is the study of this kind of process with respect to the existence of the global scaling laws of Es.

In particular, according to the galactic cannibalism model (Ostriker & Tremaine 1975, Hausman & Ostriker 1978) BCGs and cD galaxies³ are formed in the center of galaxy clusters by mergers of massive galaxies and by accretion of smaller stellar systems. Numerical simulations have shown that galactic cannibalism is able to reproduce many properties of the observed BCGs (see, e.g., Miller 1983, Merritt 1984, Malumuth & Richstone 1984). However, there are still some significant discrepancies between the predictions of these simulations and the observations: for example, the fraction of cD galaxies in clusters is in general significantly underpredicted (Dressler 1984). Observational tracers of the *late stages* of cD galaxy formation have already been found: in particular, the high frequency of

³In the literature, the definition of cD galaxies is not unambiguous. In the present work we define BCGs all the superluminous Es observed in the center of galaxy clusters, and cDs the subsample of BCGs characterized by extended low surface brightness stellar halo (see, e.g., Tonry 1987).

multiple nuclei in cD galaxies is considered an indication of recent merging (see, e.g., Matthews, Morgan & Schmidt 1964, Schneider, Gunn & Hoessel 1983). However, observational examples of the *initial stages* of cD galaxy formation are lacking. In accordance with the scenario depicted above, such systems would appear as groups of galaxies located near the center of clusters, not surrounded by a common stellar halo and spiraling, as an effect of dynamical friction, towards the center of the cluster potential.

A concrete example of galactic cannibalism: C0337-2252

We have identified a candidate for the phase before merging of BCG formation: a group of five elliptical galaxies that are observed in the core of the cluster C0337-2522 at redshift $z \simeq 0.59$. A natural question to ask is whether this system is going to collapse (in a time interesting from a cosmological point of view) and form a superluminous galaxy. Then, in our investigation, we try to estimate how many, if any, of the five galaxies merge before $z = 0$.

In case of merging, it is interesting to study the properties of the remnant and explore whether they are compatible with those of BCGs, and in particular of cD galaxies, characterized by diffuse, low surface brightness halos. In addition, we would check if some features of elliptical galaxies, such as the FJ relation, the FP, the $M_{\text{BH}}-\sigma_0$ relation, and the metallicity gradient (Peletier 1989, Carollo, Danziger & Buson 1993) are preserved during the (multiple) merging process. This kind of investigation is motivated by the fact that BCGs, both giant Es and cDs, follow quite closely the FP relation determined by less luminous Es (see, e.g., Oegerle & Hoessel 1991). They also roughly follow the FJ relation, though there are indications that a significant fraction of BCGs are brighter than would be expected from their velocity dispersion and an extrapolation of the FJ relation of normal Es (Malumuth & Kirshner 1981, 1985). In addition, BCGs have metallicity gradients consistent with those of normal Es (Fisher, Franx & Illingworth 1995), and those for which the mass of the central supermassive black hole (BH) has been measured do follow the $M_{\text{BH}}-\sigma_0$ relation (e.g., M87; Gebhardt et al. 2000, Ferrarese & Merritt 2000).

The following Chapters are organized as follows. The observed scaling relations of Es are presented in Chapter 2. In Chapter 3 and 4 we describe the galaxy models, and the numerical codes, respectively. Our simulations relative to radial orbital anisotropy are presented in Chapter 5. In Chapter 6 we discuss the results about the effects of galaxy merging on the scaling relations. The study of the process of galactic cannibalism in the galaxy cluster C0337-2522 is reported in Chapter 7. The main conclusions are summarized in Chapter 8.

2. Empirical scaling relations of elliptical galaxies

We present in this Chapter the main properties of the empirical scaling relations of Es that are of interest for the present work: we limit here our discussion to the observational properties of these relations.

2.1 The Fundamental Plane

The Fundamental Plane (FP) of elliptical galaxies (Djorgovski & Davis 1987, Dressler et al. 1987) is a scaling relation involving three of their basic *observational* properties: the circularized effective radius $\langle R \rangle_e \equiv \sqrt{a_e b_e}$ (where a_e and b_e are the major and minor semi-axis of the effective isophotal ellipse), the central velocity dispersion σ_0 (usually measured within an aperture of radius $\langle R \rangle_e/8$), and the mean effective surface brightness $\langle I \rangle_e \equiv L_B/2\pi\langle R \rangle_e^2$ (where L_B is the luminosity of the galaxy, for example in the Johnson B-band). The FP relation can be written in the form

$$\log \langle R \rangle_e = \alpha \log \sigma_0 + \beta \log \langle I \rangle_e + \gamma. \quad (2.1)$$

For their sample of early-type galaxies, Jørgensen, Franx & Kjaergaard (1996; hereafter JFK96) find values of the best-fitting coefficients (in the B-band) $\alpha = 1.20$ and $\beta = -0.83$, with a scatter around this best-fit of 0.071 in $\log \langle R \rangle_e$ (when adopting respectively, kpc, km s⁻¹ and $L_{B\odot}$ pc⁻² as length, velocity and surface brightness units). We recall here that, for the FP in the form (2.1), the numerical value of the intercept γ depends on the distance of the considered galaxy cluster.

An interesting parameterization of the FP has been introduced by Bender, Burstein & Faber (1992, hereafter BBF92):

$$k_1 \equiv \frac{\log \sigma_0^2 + \log \langle R \rangle_e}{\sqrt{2}}, \quad (2.2)$$

$$k_2 \equiv \frac{\log \sigma_0^2 + 2 \log \langle I \rangle_e - \log \langle R \rangle_e}{\sqrt{6}}, \quad (2.3)$$

$$k_3 \equiv \frac{\log \sigma_0^2 - \log \langle I \rangle_e - \log \langle R \rangle_e}{\sqrt{3}}. \quad (2.4)$$

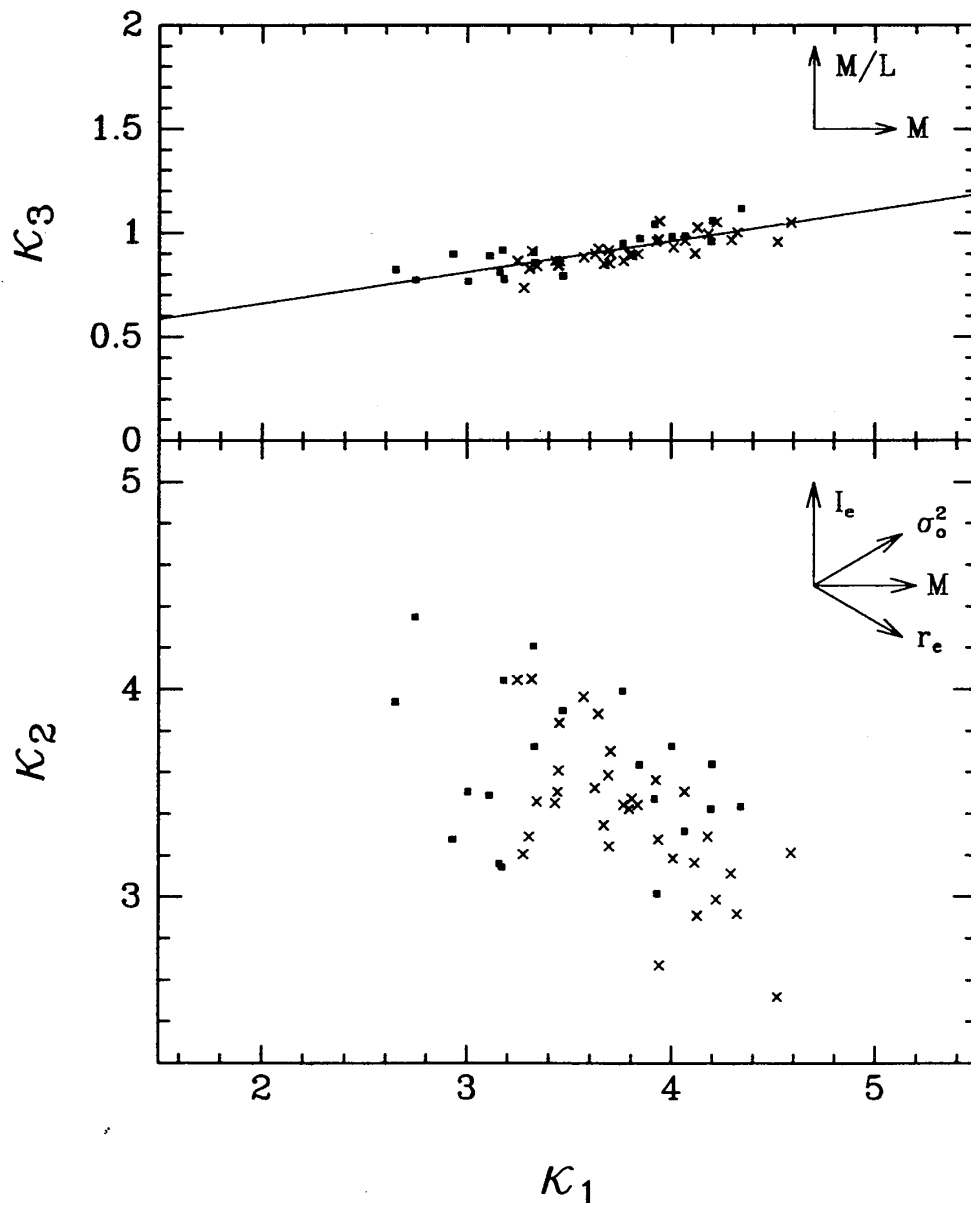


Figure 2.1: *Top:* k_3 versus k_1 in the B-band for BBF92 elliptical galaxies in the Virgo Cluster (squares) and the Coma Cluster (crosses). The solid line indicates the best-fitting relation for the subsample of Virgo galaxies (equation 2.5). *Bottom:* k_2 versus k_1 for the same sample. [Diagram from BBF92]

In particular, when projected on the (k_1, k_3) plane, the FP is seen almost edge-on and it is remarkably thin, while the distribution of galaxies in the (k_1, k_2) plane is considerably broader. For example, Virgo ellipticals studied by BBF92 are distributed on the (k_1, k_3) plane according to the best-fit relation

$$k_3 = 0.15k_1 + 0.36 \quad (2.5)$$

(where the units are the same as in equation 2.1), with a very small dispersion of r.m.s. $(k_3) \simeq 0.05$ over all the range spanned by the data, $2.6 \lesssim k_1 \lesssim 4.6$ (and so $0.75 \lesssim k_3 \lesssim 1.05$; see, e.g., Ciotti, Lanzoni & Renzini 1996). This interval corresponds to a range in luminosity $0.2 \lesssim L_B \lesssim 40$, in units of $10^{10} L_{B\odot}$. In Fig. 2.1 we report the diagram from BBF92 showing the data relative to their whole sample in the (k_1, k_3) and (k_1, k_2) planes. Equation (2.5) is represented by the solid line in the upper panel of Fig. 2.1, while in the lower panel it is apparent that the galaxies are observed in a two-dimensional region, roughly defined by $k_1 + k_2 \lesssim 7.8$ (BBF92).

By combining equations (2.2) and (2.4) with equation (2.5) the FP relation of BBF92 is then obtained directly in terms of the observables (equation 2.1): the coefficients for $\log \sigma_0$ and $\log \langle I \rangle_e$ are in good agreement with those derived (always in the Johnson B-band) by JFK96, reported above.

We recall that the slope of the best-fit FP relation is found to be dependent on the observation waveband. In particular, the coefficient α in equation (2.1) increases for increasing wavelength, up to values as high as ~ 1.5 in the K-band. Curiously, when using the k -space, the coefficient for k_1 in equation (2.5) in the K-band is only slightly different from 0.15, with a reported value of 0.147 (Pahre, Djorgovski & de Carvalho 1998).

2.2 The Faber-Jackson relation

The FJ relation is an empirical correlation between the total luminosity (for example, in the Blue band) and the projected central velocity dispersion of elliptical galaxies. This relation involves two of the three variables that define the space in which lies the FP. Thus, it can be seen as a projection in the space σ_0 - L_B of the galaxy distribution in the FP. The FJ relation is not as tight as the FP, but it contains information about the distribution of Es within the FP itself (i.e., in the k_1 - k_2 plane). Roughly speaking, the FJ relation indicates that the projected central velocity dispersion of Es increases with galaxy luminosity. The original form of the FJ relation is

$$L_B \propto \sigma_0^n, \quad (2.6)$$

with $n \simeq 4$ (Faber & Jackson 1976).

Davies et al. (1983) suggested that low and high luminosity Es could have a different behavior in the σ_0 - L_B space and proposed a double-slope fit for the relation between luminosity and central velocity dispersion, which can be written in the form

$$\frac{L_B}{10^{11} L_{B\odot}} = 0.23 \left(\frac{\sigma_0}{300 \text{ km s}^{-1}} \right)^{2.4} + 0.62 \left(\frac{\sigma_0}{300 \text{ km s}^{-1}} \right)^{4.2}. \quad (2.7)$$

The “critical” velocity dispersion separating the two slopes is $\sim 170 \text{ km s}^{-1}$; for small galaxies and bulges ($\sigma_0 \lesssim 170 \text{ km s}^{-1}$) the exponent is ~ 2.4 , considerably smaller

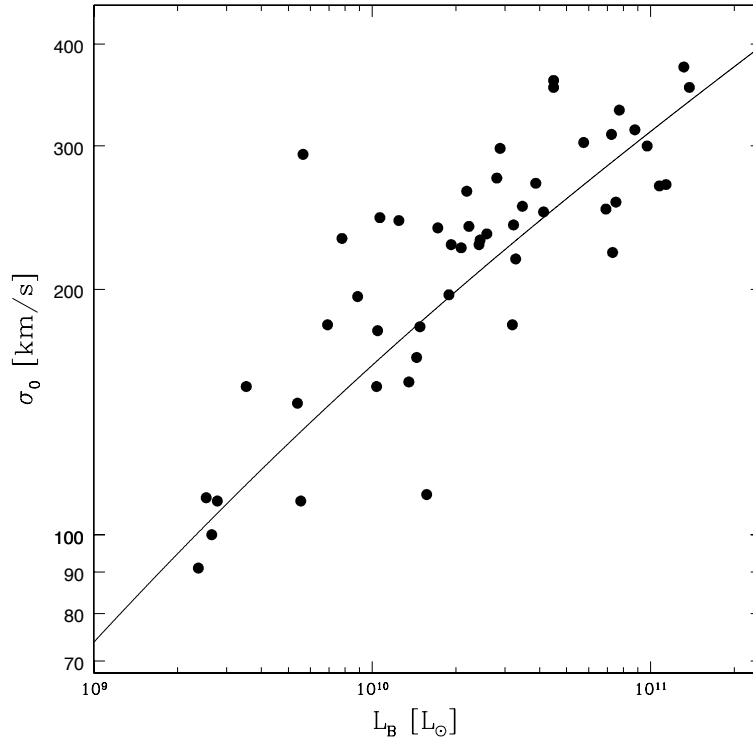


Figure 2.2: Central velocity dispersion versus total Blue luminosity for the sample of elliptical galaxies of Davies et al. (1983). The solid line represents their double-slope best-fitting relation (equation 2.7).

than 4. However, we note that this double slope is only marginally significant (the uncertainties on the two exponents are $\simeq 0.9$), and, in addition, low values of velocity dispersion are in general more affected by measurements errors. In Fig. 2.2 the data relative to the sample of ellipticals of Davies et al. (1983) are plotted with the best-fitting relation given by equation (2.7).

Other authors found reasonably good single-slope fits of the σ_0 - L_B relation over the whole observed luminosity range. For example, Dressler et al. (1987) for their sample of Virgo galaxies obtained

$$\log L_B = 3.51 \log \sigma_0 + 2.09 \pm 0.23, \quad (2.8)$$

where L_B is expressed in $L_{B\odot}$ and σ_0 in km s^{-1} . On the other hand, very recent surveys seem to indicate a value $n \simeq 4$ for the FJ exponent in equation (2.6) (Bernardi et al. 2003, and references therein).

It follows from this picture that the slope of the FJ relation does not seem to be universally determined. Nevertheless, the increase of σ_0 with luminosity, whatever the exact slope of the relation, *has* strong observational evidence. For the purpose of our investigation we will assume as fiducial FJ relation the expression in equation (2.6), with reference values of the exponent in the range $3.5 \lesssim n \lesssim 4$.

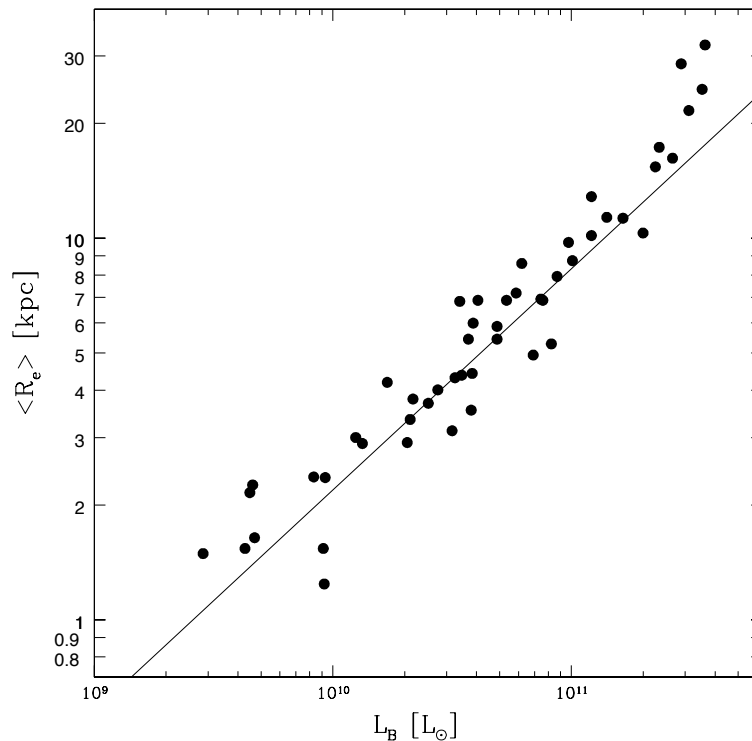


Figure 2.3: Effective radius as a function of total Blue luminosity. The data are from Davies et al. (1983). The solid line represents their best-fitting relation (equation 2.10).

2.3 The Kormendy relation

The Kormendy (1977) relation involves the effective radius and the total luminosity (or, in another equivalent form, the effective radius and the mean effective surface brightness) of elliptical galaxies. As well as the FJ relation, the Kormendy relation is a projection of the galaxy distribution within the FP and, though quite dispersed, it contains additional information with respect to the edge-on FP (equation 2.5). The Kormendy relation indicates that the effective radius increases with the galaxy luminosity (for example in the B-band) as a power-law, and can be written in the form

$$\langle R \rangle_e \propto L_B^a. \quad (2.9)$$

As it happens for the FJ relation, also the exponent a of the best-fit Kormendy relation is not exactly determined. In the literature the estimates of the slope of this power-law are various and they often differ significantly, depending in general on the method used in measuring $\langle R \rangle_e$ ($R^{1/4}$ -fitting or growth curves) and on the details of the fitting procedure (for a discussion see Davies et al. 1983). For example Kormendy (1977), measuring $\langle R \rangle_e$ with the $R^{1/4}$ -fitting, found for his sample of Es a best-fit $\langle R \rangle_e \propto L_B^{0.8 \pm 0.3}$. On the other hand, the more complete sample of Davies et al. (1983), who adopted the growth curves method, is well fitted by

$$\log \langle R \rangle_e = (0.58 \pm 0.03) \log L_B - 5.46 \pm 0.25, \quad (2.10)$$

where $\langle R \rangle_e$ is expressed in kpc and L_B in $L_{B\odot}$. More recent studies (e.g., Ziegler et al. 1999) showed that the exponent in equation (2.9) is strongly dependent also on the considered galaxy sample, and is found in the range $0.88 \lesssim a \lesssim 1.62$. Note however that a lower value ($a \sim 0.75$) is reported by Bernardi et al. (2003), who consider a quite large sample of Es. In Fig. 2.3 we plot, as an example, the effective radius as a function of the total Blue luminosity for the Es belonging to the sample of Davies et al. (1983) and, as a solid line, the corresponding best-fitting relation (equation 2.10).

2.4 The M_{BH} - σ_0 and the Magorrian relations

Supermassive BHs are found at the center of most elliptical galaxies and bulges of spiral galaxies (see, e.g., Kormendy & Richstone 1995, van der Marel 1999, de Zeeuw 2001). The mass of these objects is in the range $10^6 - 10^9 M_\odot$ and is correlated with a few properties of the host galaxies. In particular Kormendy & Richstone (1995) and Magorrian et al. (1998) individuated a linear relation between the mass of the central BH (M_{BH}) and the total luminosity of the host bulge or elliptical galaxy. This relation, usually known as Magorrian relation, is characterized by a quite large intrinsic scatter. This can be seen in the upper panel of Fig. 2.4, where we plot the Blue absolute magnitude of the spheroidal component of the galaxy as a function of the BH mass, for the sample of galaxies of Tremaine et al. (2002).

In the last years it has been found that the mass of the central BH correlates very well with the central velocity dispersion of the host spheroid (Gebhardt et al. 2000; Ferrarese & Merritt 2000). This very tight M_{BH} - σ_0 relation can be written in the form

$$\log \left(\frac{M_{BH}}{M_\odot} \right) = \alpha \log \left(\frac{\sigma_0}{200 \text{ km s}^{-1}} \right) + \beta, \quad (2.11)$$

where the exact value of the coefficients, and in particular of the slope α , are debated. The first estimates were given by Gebhardt et al. (2000), who found $\alpha = 3.75 \pm 0.3$, and Ferrarese & Merritt (2000), who found instead $\alpha = 4.8 \pm 0.5$. In more recent works, authors belonging to these two groups have found more similar values of the slope. The best-fitting coefficient is $\alpha = 4.58 \pm 0.52$ according to Ferrarese (2002), while $\alpha = 4.02 \pm 0.32$ for Tremaine et al. (2002). The possible sources of the difference in the values of the slope have been discussed by Merritt & Ferrarese (2001) and Tremaine et al. (2002). However, the question is still open. Nevertheless there is diffuse agreement on the fact that the M_{BH} - σ_0 relation, whatever the exact value of the slope, has a very small *intrinsic* dispersion (about $0.25 - 0.3$ dex in BH mass for fixed σ_0). In the lower panel of Fig. 2.4 we plot, as an example, the central velocity dispersion as a function of BH mass for the same sample as in the upper panel (Tremaine et al. 2002). The solid line represents their best-fitting relation.

In order to take into account the discussed uncertainties on the slope α , in what follows we will consider the M_{BH} - σ_0 relation in the form of equation (2.11), assuming the coefficient α in the range $4 \lesssim \alpha \lesssim 5$. For the numerical value of the intercept β , we recall that $\beta = 8.13 \pm 0.06$, and $\beta = 8.22 \pm 0.08$ are found by Tremaine et al. (2002) and Ferrarese (2002), respectively.

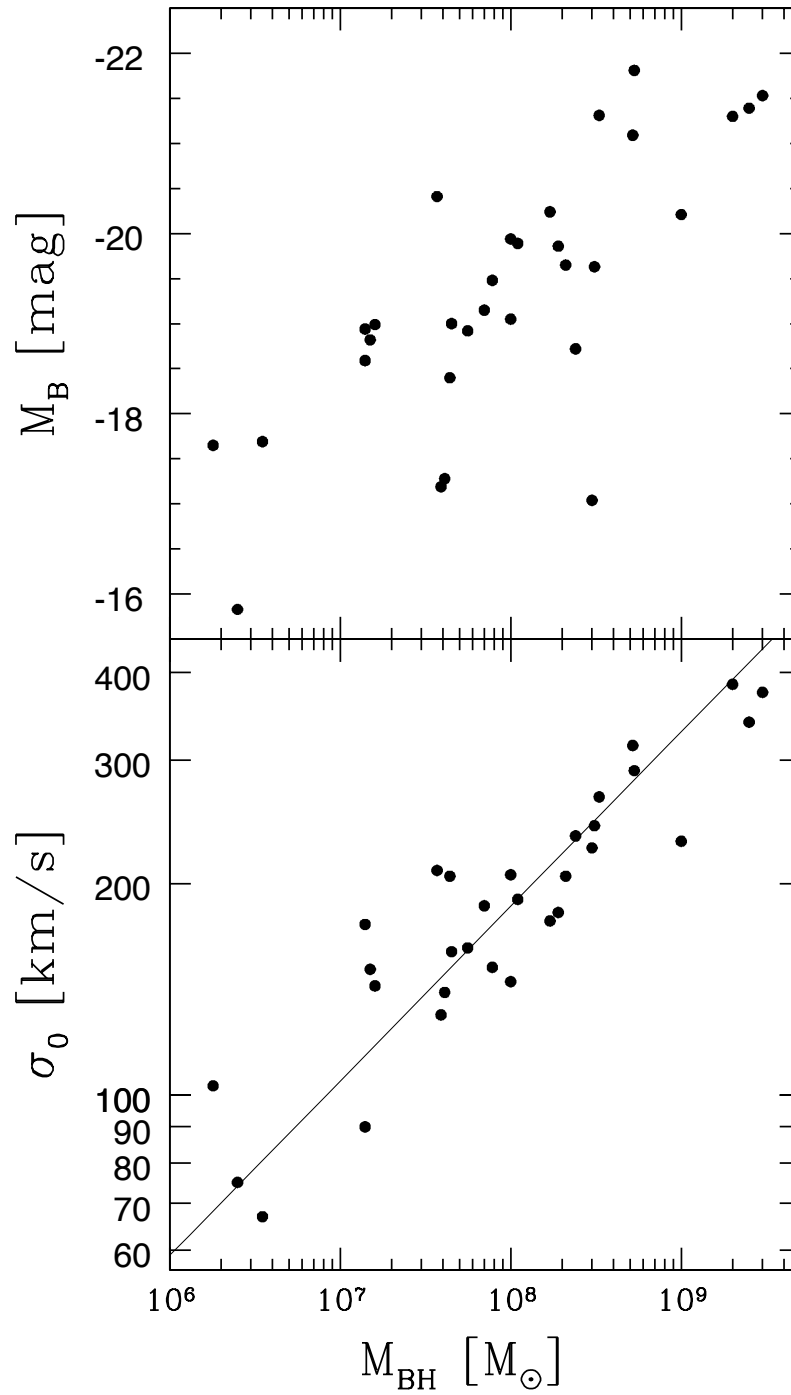


Figure 2.4: *Top:* Blue absolute magnitude versus BH mass for the sample of galaxies of Tremaine et al. (2002). Magnitudes refers to the spheroidal component of the galaxy only. *Bottom:* central velocity dispersion versus BH mass for the same sample as in the upper panel. The solid line represent the best-fitting relation (equation 2.11 with $\alpha = 4.02$, $\beta = 8.13$).

3. Galaxy models

As initial conditions for the N -body simulations we use one and two-component spherical galaxy models. The one-component models represent the case of galaxies with stellar component only (or with dark and luminous matter following the same density profile and internal dynamics). The two-component case corresponds to a galaxy with a stellar component and a dark halo with different spatial distributions and/or internal dynamics. The considered models allow for the presence of radial anisotropy in the orbital distribution.

3.1 One-component models

For the one-component case, we use spherically symmetric γ -models (Dehnen 1993; Tremaine et al. 1994). The density, mass, and relative (positive) potential profiles of the stellar component are then given by

$$\rho_*(r) = \frac{3-\gamma}{4\pi} \frac{M_* r_c}{r^\gamma (r_c + r)^{4-\gamma}} \quad (0 \leq \gamma < 3), \quad (3.1)$$

$$\frac{M_*(r)}{M_*} = \left(\frac{r}{r_c + r} \right)^{3-\gamma}, \quad (3.2)$$

$$\Psi_*(r) = \frac{GM_*}{r_c(2-\gamma)} \left[1 - \left(\frac{r}{r_c + r} \right)^{2-\gamma} \right] \quad (\gamma \neq 2), \quad (3.3)$$

$$\Psi_*(r) = \frac{GM_*}{r_c} \ln \frac{r_c + r}{r} \quad (\gamma = 2), \quad (3.4)$$

where M_* is the total stellar mass, and r_c is a scale parameter usually called “core radius”. The $\gamma = 1$ and $\gamma = 2$ cases correspond to Hernquist (1990) and Jaffe (1983) density distributions, two reasonable approximations (when projected) of the $R^{1/4}$ law (de Vaucouleurs 1948).

For simplicity, radial anisotropy in the stellar orbital distribution is introduced by using the Osipkov-Merritt (OM) parameterization (Osipkov 1979; Merritt 1985). In this case the distribution function (DF) is given by

$$f_*(Q) = \frac{1}{\sqrt{8\pi^2}} \frac{d}{dQ} \int_0^Q \frac{dQ_*}{d\Psi_T} \frac{d\Psi_T}{\sqrt{Q - \Psi_T}}, \quad (3.5)$$

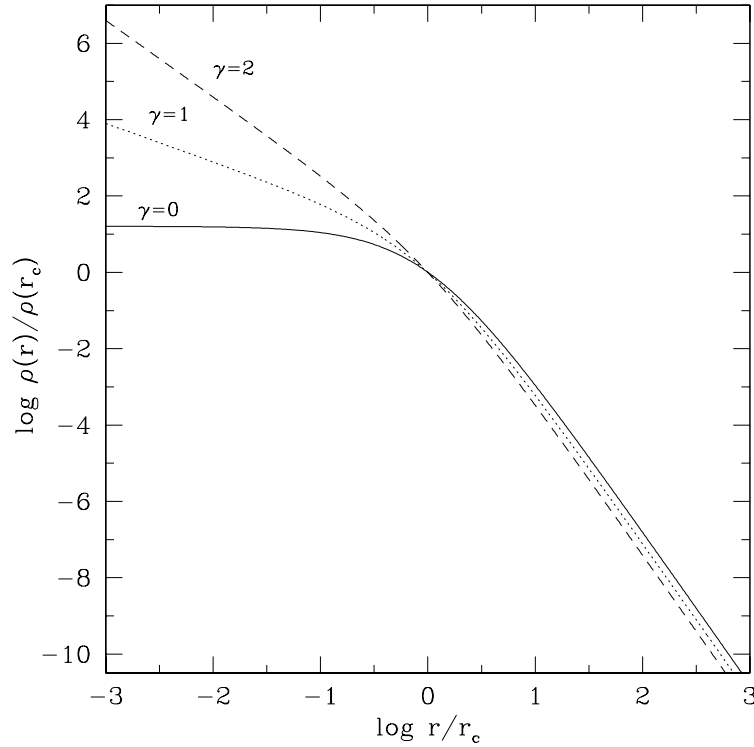


Figure 3.1: Density profiles of the one-component $\gamma = 0$ (solid curve), $\gamma = 1$ (dotted curve) and $\gamma = 2$ (dashed curve) models.

where

$$\varrho_*(r) = \left(1 + \frac{r^2}{r_a^2}\right) \rho_*(r). \quad (3.6)$$

The variable Q is defined as $Q \equiv \mathcal{E} - L^2/2r_a^2$, where the relative (positive) energy is given by $\mathcal{E} = \Psi_* - v^2/2$, v is the modulus of the velocity vector, $\Psi_T = \Psi_*$ is the relative total potential, L is the angular momentum modulus per unit mass, and $f_*(Q) = 0$ for $Q \leq 0$. The quantity r_a is the so-called “anisotropy radius”: for r larger than r_a the velocity dispersion tensor is mainly radially anisotropic, while for $r \ll r_a$ the tensor is nearly isotropic. Isotropy is realized at the model center, independently of the value of r_a ; in the limit $r_a/r_c \rightarrow \infty$, $Q = \mathcal{E}$ and the velocity dispersion tensor becomes globally isotropic.

Fig. 3.1 shows the density profiles corresponding to equation (3.1) for $\gamma = 0$ (solid curve), $\gamma = 1$ (dotted curve) and $\gamma = 2$ (dashed curve); in Fig. 3.2 the radial velocity dispersion profiles of the corresponding isotropic models are represented (see, e.g., Tremaine et al. 1994).

3.2 Two-component models

We consider two-component models belonging to the family of the spherically symmetric (γ_1, γ_2) models (Ciotti 1996, 1999). In these models both the stellar

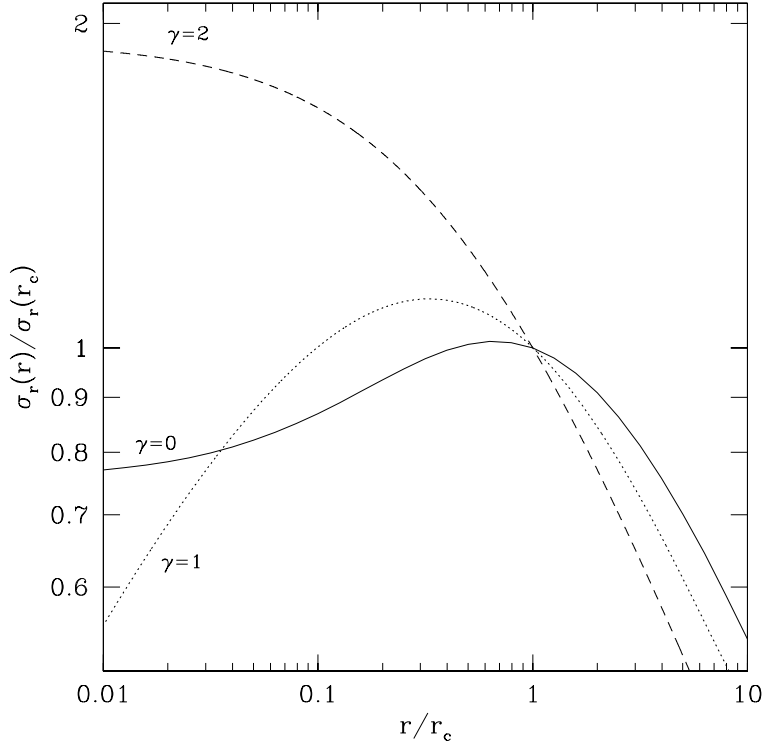


Figure 3.2: Radial component of the velocity dispersion tensor as a function of radius for the isotropic one-component $\gamma = 0$ (solid curve), $\gamma = 1$ (dotted curve) and $\gamma = 2$ (dashed curve) models.

component and the dark matter (DM) halo have density, mass and potential profiles of the same family of γ -models. γ_1 and γ_2 are the values of the dimensionless parameter γ for the two components. The DM halo is described by $\rho_h(r)$, $M_h(r)$ and $\Psi_h(r)$ profiles of the same family of equations (3.1)-(3.4), with mass M_h and core radius r_h related to stellar mass M_* and core radius r_c by $M_h \equiv \mu M_*$ and $r_h \equiv \beta r_c$.

The distribution function of the stellar component is given by equation (3.5), where now the relative total potential is $\Psi_T = \Psi_* + \Psi_h$. In order to reduce the dimensionality of the parameter space, the orbital distribution of the DM halos is assumed isotropic in all our two-component models; as a consequence the DF for the DM halo component is a function of the relative energy only and is given by

$$f_h(\mathcal{E}) = \frac{1}{\sqrt{8}\pi^2} \frac{d}{d\mathcal{E}} \int_0^{\mathcal{E}} \frac{d\rho_h(r)}{d\Psi_T} \frac{d\Psi_T}{\sqrt{\mathcal{E} - \Psi_T}}, \quad (3.7)$$

where, again, $\Psi_T = \Psi_* + \Psi_h$.

3.3 Physical scales

According to the given definitions, from the structural and dynamical point of view the one-component models are completely determined by four quantities: the two

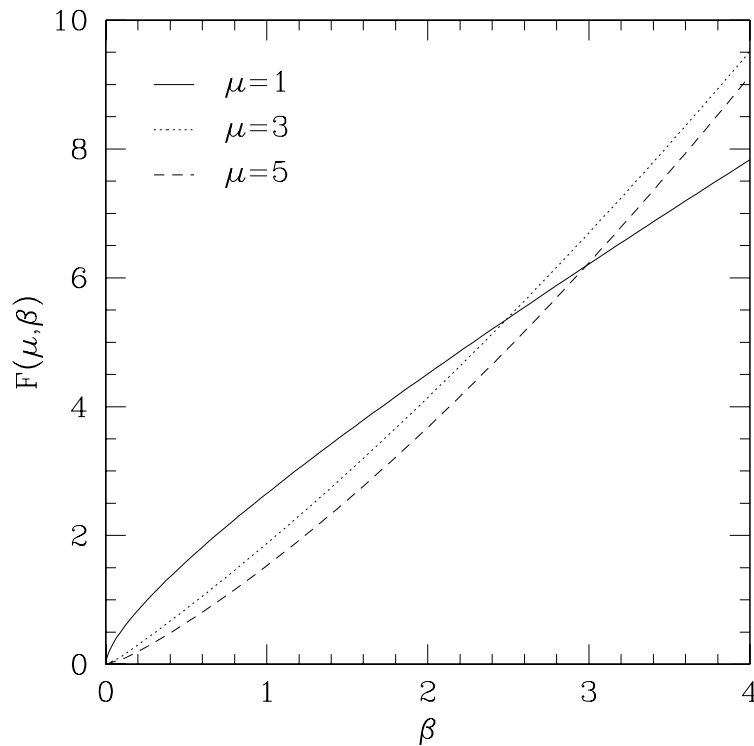


Figure 3.3: Normalized dynamical time $F(\mu, \beta) = T_{\text{dyn}}/\pi\sqrt{r_c^3/2GM_*}$ vs. β for two-component (1,1) models with $\mu = 1, 3, 5$.

physical scales M_* and r_c , and the two dimensionless parameters γ and $s_a \equiv r_a/r_c$.

In the numerical simulations M_* , r_c and T_{dyn} are adopted as mass, length and time scales. T_{dyn} is the half-mass dynamical time, defined as

$$T_{\text{dyn}} \equiv \sqrt{\frac{3\pi}{16G\rho_M}} = \pi\sqrt{\frac{r_c^3}{2GM_*}}F(\gamma), \quad (3.8)$$

where $\rho_M = 3M_*/8\pi r_M^3$ is the mean density inside the half-mass radius r_M and

$$F(\gamma) = \left(2^{\frac{1}{3-\gamma}} - 1\right)^{-\frac{3}{2}}. \quad (3.9)$$

Note that at fixed M_* and r_c the half-mass dynamical time depends strongly on γ . For example, $F(0)/F(1) \simeq 2.0$ and $F(1)/F(2) \simeq 3.8$. Finally, the velocity scale is given by

$$v_c \equiv \frac{r_c}{T_{\text{dyn}}} = \frac{1}{\pi F(\gamma)} \sqrt{\frac{2GM_*}{r_c}}. \quad (3.10)$$

In the case of two-component galaxies we limit our present study to (1,1) models, i.e., to two-component Hernquist models (Ciotti 1996). In this way the DM halo is similar (in the central region) to the Navarro, Frenk & White (1996)

profile. (1,1) models are characterized by five quantities, the two physical scales M_* and r_c , and the three dimensionless parameters s_a , μ and β . Their T_{dyn} depends on μ and β : from definition (3.8), where now $\rho_M = 3(1 + \mu)M_*/(8\pi r_M^3)$ and r_M is the half-mass radius of the total (stellar plus dark) density distribution, it results that

$$T_{\text{dyn}} = \pi \sqrt{\frac{r_c^3}{2GM_*}} F(\mu, \beta), \quad (3.11)$$

where $F = x^{3/2}(\mu, \beta)/\sqrt{1 + \mu}$, and x is the solution of

$$\left(\frac{x}{1+x}\right)^2 + \mu \left(\frac{x}{\beta+x}\right)^2 = \frac{1+\mu}{2}. \quad (3.12)$$

The three curves in Fig. 3.3 correspond to $F(\mu, \beta)$ as a function of β , for $\mu = 1$ (solid line), $\mu = 3$ (dotted line), and $\mu = 5$ (dashed line).

Finally note that, once the dimensionless numbers s_a and γ (for one-component models) and s_a , μ , and β (for two-component models) are fixed, the results of the numerical simulations can be rescaled for arbitrary values of r_c , M_* , and L_B (modulo the free parameter $\Upsilon_* \equiv M_*/L_B$, i.e., the *stellar* mass to light ratio, in the Blue band).

4. The numerical method

4.1 Computational methods for collisionless systems

When dealing with systems characterized by a very large number of particles, and where the cumulative effects of two-particles correlations are negligible, the one-particle distribution function (DF) in the system phase-space $f(\mathbf{x}, \mathbf{v}, t)$ evolves according to the collisionless Boltzmann equation (CBE)

$$\frac{\partial f}{\partial t} + \frac{\partial f}{\partial \mathbf{x}} \cdot \mathbf{v} - \frac{\partial f}{\partial \mathbf{v}} \cdot \nabla \Phi = 0, \quad (4.1)$$

where the potential is

$$\Phi(\mathbf{x}, t) = -G \int \frac{d^3 \mathbf{x}'}{||\mathbf{x} - \mathbf{x}'||} \int f(\mathbf{x}', \mathbf{v}, t) d^3 \mathbf{v}, \quad (4.2)$$

for self-gravitating systems, $||\mathbf{x} - \mathbf{x}'||^2 = \langle \mathbf{x} - \mathbf{x}', \mathbf{x} - \mathbf{x}' \rangle$, and \langle, \rangle is the standard inner product.

Numerically, the CBE is usually treated by sampling the DF with a large number of particles N , which is however orders of magnitude smaller than the number of bodies in whatever physical collisionless system. Thus, writing the DF as the average of a set of discrete realizations of N particles, given by

$$f(\mathbf{x}, \mathbf{v}, t) = \frac{1}{N} \langle \sum_{i=1}^N m_i \delta[\mathbf{x}_i(t) - \mathbf{x}] \delta[\mathbf{v}_i(t) - \mathbf{v}] \rangle, \quad (4.3)$$

with m_i the mass of the i -th particle, the integration of the CBE reduces to integrate the Hamiltonian equations

$$\frac{d\mathbf{x}_i}{dt} = \mathbf{v}_i, \quad (4.4)$$

$$\frac{d\mathbf{v}_i}{dt} = -\nabla \Phi(\mathbf{x}_i, t). \quad (4.5)$$

Combining equations (4.2) and (4.3), the potential results

$$\Phi(\mathbf{x}_i, t) = -G \sum_{j=1}^N m_j g(\mathbf{x}_i - \mathbf{x}_j), \quad (4.6)$$

where $g(\mathbf{x}_i - \mathbf{x}_j) = 1/||\mathbf{x}_i - \mathbf{x}_j||$ is the Green's function of the Laplacian operator. The representation of the DF as a sum of δ -functions (equation 4.3) does not reproduce the smoothness of the real collisionless systems. Thus, in the N -body codes the Newtonian force is softened at small distances. In other words, this is equivalent to represent the particles as extended mass distributions, substituting $m_i \delta[\mathbf{x}(t)_i - \mathbf{x}]$ in equation (4.3) with a density distribution

$$W_{\text{soft}}[\mathbf{x}_i(t) - \mathbf{x}], \quad (4.7)$$

with characteristic width given by the so-called *softening length*. Correspondingly, the Green function in the potential (equation 4.6) is replaced by a function $g_{\text{soft}}(\mathbf{x})$, so that the Poisson equation

$$\nabla^2 \Phi[g_{\text{soft}}(\mathbf{x})] = 4\pi G W_{\text{soft}} \quad (4.8)$$

is satisfied. Finally, the softened force (per unit mass) exerted by a particle on another particle in \mathbf{x} is

$$\mathbf{F}_{\text{soft}}(\mathbf{x}) = -\nabla \Phi[g_{\text{soft}}(\mathbf{x})]. \quad (4.9)$$

The introduction of softening produces the following effects (see Dehnen 2001 and references therein):

- a) it removes the two-body force singularity, thus reducing the time integration numerical problems;
- b) at some extent, it helps to simulate a collisionless DF, avoiding artificial two-body encounters and binaries;
- c) at variance with what often believed, it does not increase too much the two-body relaxation time, which is mainly dependent on the effect of noise on large scale.

A longstanding computational problem encountered to integrate the resulting N -body system is that the direct force evaluation has $O(N^2)$ complexity in operations count. Three main methods have been proposed in order to approximate this evaluation.

1) The *Particle-Mesh* approach (Hockney & Eastwood 1981), where a fixed grid is introduced with a number N_g of grid points. The particle density is then interpolated on the grid, and the gravitational potential is computed by numerically evaluating the integral (4.2) on the grid in N_g operations. The force is then back interpolated on each particle. In periodic domains (such as in cosmological simulations), where the Fast Fourier Transforms (FFT) can be used, this amounts to a total of $O(N \log N_g)$ complexity in operations count. However, the Particle-Mesh approach, because of the non adaptivity of the grid, is not suitable for applications where highly inhomogeneous density distributions and very violent dynamical processes are involved (e.g., in the case of galaxy merging). In addition, the error estimate is quite difficult to be obtained, and the softening, determined (implicitly) by the grid size, is not easily controlled.

2) The *tree-code* algorithms, that are pure Lagrangian schemes with no fixed grid. The first main contribution in this direction has been provided by Barnes & Hut (1986, hereafter BH86). In their tree-code the data are organized in an oct-tree adaptive set of cubic cells containing particles. In computing the interactions

of sufficiently distant particle–cell pairs, one approximates equation (4.6) using a Taylor expansion in Cartesian coordinates centered in the center of mass of the cell, usually truncated at the quadrupole term. The expansion parameter is the ratio l/D (where l is the size of the cell and the D is the distance between the particle and the center of mass of the cell). The tree-code algorithm allows to reach effective $O(N \log N)$ computational complexity in operations count. At the same time, it is characterized by great adaptivity and good accuracy. Thus, this scheme has been implemented in many N -body codes currently used in astrophysical applications. The adopted time integrator is the standard leapfrog scheme, with uniform time step, which is symplectic⁴. In some implementations a (quasi symplectic) integrator with a variable time step (from particle to particle) is introduced (see Section 4.3.2).

3) The *Fast Multipole Methods* (FMMs; Greengard & Rokhlin 1987, 1997): in this approach, a system of particles is first organized in a oct-tree structure of nested cells, providing a hierarchical grouping of particles. For each pair of distant cells (A, B), the interactions between particles are approximated by a Taylor expansion of the two-point Green’s function around the geometrical center of each cell by using spherical harmonics. In these cell-cell interactions the two-body symmetry of the exact Green’s function is preserved by the multipole approximation. In principle, a FMM-based scheme can achieve a prescribed accuracy ϵ by increasing the order p of the Taylor polynomial, and/or by lowering the expansion parameter l/D . Even if a formal, asymptotic scaling $O(N)$ is expected, the proposed algorithms in the original formulation appear in fact less performing and difficult to be implemented. In addition, even in a more recent and improved formulation (Capuzzo-Dolcetta & Miocchi 1998), the FMM scheme results to be not competitive with the classical BH86 tree-code. Note however that, only when very high accuracy (better than $\epsilon \sim 10^{-5}$) is required, the FMMs are the most efficient currently available N -body codes.

Recently, a new Poisson solver for N -body systems has been developed by Dehnen (2000; 2002, hereafter D02). This numerical scheme is a combination of the tree-codes and the FMMs, and achieves an effective $O(N)$ computational complexity, together with an almost perfect preservation of the linear momentum. Dehnen’s scheme develops the FMM by taking advantage of the adaptivity of tree algorithms to select the pairs of cells (both bodies and cells, even belonging to different levels of refinements), and introducing some new ingredients, which succeed to improve the overall efficiency in a substantial way. The Taylor expansion is performed in Cartesian components, and the expansion centers are the *centers of mass* of the cells, as in the BH86 tree-code. In addition, the truncation order is fixed: $p = 3$ is chosen as optimal. Thus, only the value of l/D controls the accuracy of the Taylor approximation.

4.2 N -body codes used for our simulations

From the discussion above it is apparent that the numerical scheme proposed by D02 can be considered the state of the art of N -body simulations for collisionless stellar dynamics, in intermediate accuracy range ($\epsilon \sim 10^{-3}$). For this reason,

⁴It preserves the Hamiltonian structure.

even if a scalar C++ code based on this scheme was already available (falcON; D02), we implemented the algorithms proposed by D02 in a Fortran-90 code, and parallelized it by a domain decomposition using the MPI (Message Passing Interface) routines. This parallel code, named FVFPS (Fortran Version of a Fast Poisson Solver; Londrillo, Nipoti & Ciotti 2003), was used to run a substantial fraction of the simulation presented in this work. Besides the new FVFPS code, we also used for our simulations other two N -body codes based on tree algorithms: the Barnes & Hut (1986, hereafter BH86) tree-code (in a Fortran 77 version made publicly available by Hernquist 1987), and GADGET (GALaxies with Dark matter and Gas intEract, Springel, Yoshida & White 2001, hereafter SYW01), both in its scalar and parallel versions. By using more than one code we can also check that the results of the simulations are independent of the details of the numerical scheme. In addition, the present work is a good opportunity to test our new FVFPS code by comparing its performances with those of two well tested codes as the BH86 tree-code and GADGET. Since the BH86 tree-code is the prototype of the tree algorithms, we will first describe its main characteristics (Section 4.2.1). Then we will point out what are the most important modifications introduced in GADGET (Section 4.2.2) and we will present in detail our FVFPS code (Section 4.2.3).

4.2.1 The Barnes & Hut tree-code

The calculation of the forces in the BH86 tree-code is based on a hierarchical subdivision of space in cubic cells. The *tree* is obtained by starting from a root cell (a cube containing all the N particles), and subdividing it in 8 cubic sub-cells with half the size of the parent cell. Empty cells are excluded from the tree; cells with more than one particle are recursively divided in 8 sub-cells; cells with only one particle are bodies, i.e., the leaves of the tree. The gravitational field at a given point is computed considering the exact contribution of near bodies, by direct summation, and the approximated contribution of sufficiently distant cells, by using multipole expansion. As pointed out above, as a consequence of the introduction of this tree technique the cost of the computation of the forces for the N bodies scales as $O(N \log N)$, resulting remarkably less time consuming than the $O(N^2)$ algorithms based on the direct summation.

In the considered implementation, the force between individual particles is smoothed through the introduction of the standard Plummer softening, i.e., the softened potential produced at a distance r by a particle of mass m is

$$\Phi(r) = -\frac{Gm}{\varepsilon} g_{\text{pl}}\left(\frac{r}{\varepsilon}\right) \quad (4.10)$$

where m is the particle mass, r is the mutual distance between the two particles, and the smoothing parameter ε is called *softening length*, and

$$g_{\text{pl}}(x) = \frac{1}{(1+x^2)^{1/2}} \quad (4.11)$$

is the Plummer softening kernel.

The concept of “sufficiently distant cells”, introduced to choose between approximated and exact calculation of the forces, is quantified by adopting an

opening criterion depending on a single dimensionless parameter θ , called *opening angle*. Let us consider the interaction between a cell of length l and a particle at a distance D from the center of mass of the cell. If

$$\frac{l}{D} < \theta \quad (4.12)$$

(i.e., the cell is “sufficiently distant”), the force exerted by the cell on the particle is calculated with the multipole expansion. Otherwise, the cell is opened and is split in its 8 sub-cells, which are recursively analysed with the opening criterion (4.12).

In the version implemented by Hernquist (1987), the higher allowed term of the multipole expansion is the quadrupole. The dipole term of the force (centered in the center of mass of the cell) is null by definition. Thus, the approximated potential for a particle in \mathbf{x} produced by a group of k particles of mass m_k at \mathbf{y}_k in a cell B of total mass M_B with center of mass \mathbf{z}_B is (Hernquist 1987)

$$\Phi(\mathbf{x}) = \sum_{n=0}^2 -\frac{(-1)^n}{n!} \nabla^{(n)} g(\mathbf{r}_0) \odot \mathbf{M}_B^n, \quad (4.13)$$

where $\mathbf{r}_0 = \mathbf{x} - \mathbf{z}_B$, $g = g_{\text{pl}}$ is the Plummer softening kernel, and the tensor \mathbf{M}_B^n is such that $\mathbf{M}_B^0 = M_B$, \mathbf{M}_B^1 is the (null) dipole moment, and

$$\mathbf{M}_B^2 = \sum_{k \in B} m_k (\mathbf{y}_k - \mathbf{z}_B)^{(2)} \quad (4.14)$$

is the quadrupole moment. Note that, following D02, we indicate the n -fold outer product of a vector \mathbf{V} with $\mathbf{V}^{(n)}$, and the tensor inner product with \odot . The approximated force per unit mass is then recovered from equation (4.13), computing $\mathbf{F}(\mathbf{x}) = -\nabla \Phi$.

In the considered implementation of the BH86 tree-code a second-order leapfrog integrator is used to advance positions and velocities. In particular, a *kick-drift-kick* scheme is adopted in the form (see, e.g., Quinn et al. 1997)

$$\mathbf{v}_{n+1/2} = \mathbf{v}_n + \frac{1}{2} \Delta t \mathbf{a}_n, \quad (4.15)$$

$$\mathbf{x}_{n+1} = \mathbf{x}_n + \Delta t \mathbf{v}_{n+1/2}, \quad (4.16)$$

$$\mathbf{v}_{n+1} = \mathbf{v}_{n+1/2} + \frac{1}{2} \Delta t \mathbf{a}_{n+1}, \quad (4.17)$$

where, for a given particle, \mathbf{x}_i and \mathbf{v}_i are the position and the velocity at the i -th step, and $\mathbf{a}_i = \mathbf{a}(\mathbf{x}_i)$ is the acceleration evaluated at \mathbf{x}_i . The time-step Δt is the same for all particles and is constant during the simulation, so that the integrator is symplectic and, thus, time-reversible (see discussion in Section 4.3.2).

4.2.2 GADGET

GADGET is a simulation code that evolves both self-gravitating collisionless fluids and collisional gas (SYW01). In the present work we use it only for simulations of collisionless isolated or interacting systems, and so we recall here only its main properties with respect to this application.

GADGET is a tree-code, with the same tree structure as the BH86 tree-code. The Newtonian gravity is corrected with a cubic spline softening: the smoothed potential generated by a particle of mass m at a distance r is

$$\Phi(r) = -\frac{Gm}{h_3} g_{\text{spl3}}\left(\frac{r}{h_3}\right), \quad (4.18)$$

where h_3 is the softening length, and the smoothing kernel $g_{\text{spl3}}(x)$ is given by

$$g_{\text{spl3}}(x) = \begin{cases} -\frac{16}{3}x^2 + \frac{48}{5}x^4 - \frac{32}{5}x^5 + \frac{14}{5}, & (0 \leq x < \frac{1}{2}), \\ -\frac{1}{15x} - \frac{32}{3}x^2 + 16x^3 - \frac{48}{5}x^4 + \frac{32}{15}x^5 + \frac{16}{5}, & (\frac{1}{2} \leq x < 1), \\ \frac{1}{x}, & (x \geq 1). \end{cases} \quad (4.19)$$

Note that the spline softened potentials are, by definition, exactly Newtonian for $r \geq h_3$. In addition, we recall here that, owing to their different definitions, the spline softening length h_3 and the Plummer softening length ε are not directly comparable. A Plummer softening length “equivalent” to a given spline softening h_3 can be defined, for example, by imposing that the minimum of the potential is the same in the two cases (see, e.g., SYW01). For the considered cubic spline this happens for $\varepsilon = h_3/2.8$ (see Section 4.2.1).

The multipole expansion of the potential in GADGET is analogous to that in equation (4.13), but clearly the exact form depends on the adopted softened potential (equations 4.18 and 4.19; see SYW01 for details). As well as in the BH86 tree-code, an opening criterion is used, but in a different form. In particular, the equation (4.12) is substituted by

$$Mt^4 < \alpha |\mathbf{a}| D^6, \quad (4.20)$$

where M is the mass of the cell, $|\mathbf{a}|$ is the modulus of the acceleration of the particle in the previous step, and α is a new cell-opening parameter. The opening criterion (4.20) follows from the requirement that the hexadecupole order of the multipole expansion (i.e., the first non-vanishing neglected term) does not exceed a fraction α of the total force exerted on the particle (SYW01). It is then clear that the cell-opening parameter α and the BH86 opening angle θ have different meaning and their values are not directly comparable (see Section 4.3.3).

However, the only really new ingredient in GADGET, with respect to the BH86 tree-code is that SYW01 adopt, as time integrator, a variant of the leapfrog, in which the time-step is allowed to vary from step to step and also from particle to particle. In other words, at each time-step only a fraction of the particles is advanced. With this choice, at the same computational cost, a better accuracy can be obtained, since very short time-steps are used only for particles that need them, while the majority of the particles have longer time-steps (at least in usual density distributions). In this case, for a single particle, the *drift-kick-drift* scheme is adopted:

$$\mathbf{x}_{n+1/2} = \mathbf{x}_n + \frac{1}{2}\Delta t \mathbf{v}_n, \quad (4.21)$$

$$\mathbf{v}_{n+1} = \mathbf{v}_n + \Delta t \mathbf{a}(\mathbf{x}_{n+1/2}), \quad (4.22)$$

$$\mathbf{x}_{n+1} = \mathbf{x}_{n+1/2} + \frac{1}{2}\Delta t \mathbf{v}_{n+1}. \quad (4.23)$$

The variable time-step implies the introduction of a time-step criterion for the choice of Δt for each particle at each time. Among the different time-step criteria available in GADGET, we chose for our simulations

$$\Delta t = \alpha_{\text{tol}} \frac{\sigma}{|\mathbf{a}|}, \quad (4.24)$$

where σ is a typical velocity dispersion of the particles and α_{tol} is the time-step tolerance parameter (see Section 4.3.2 and SYW01). In order to avoid too long or too short time-steps for groups of particles in particular configurations, the range of the acceptable time-steps can be limited by the optional choice of the minimum and the maximum time-step Δt_{min} and Δt_{max} .

4.2.3 FVFPS: a parallel implementation of Dehnen's $O(N)$ force algorithm

The scheme recently introduced by D02 can be seen as an original combination of the tree-based BH86 algorithm and of the FMMs with multipole expansion truncated at a fixed low order level. This scheme, implemented by Dehnen in a C++ code [named *falcON*, Force ALgorithm with Complexity $O(N)$], results in a significant improvement over the existing tree-codes, in terms of uniform accuracy, linear momentum conservation, and CPU time performances. Moreover, the numerical tests presented in the D02 paper show that for an accuracy level $\epsilon \sim 10^{-3}$, for the first time an *effective* $O(N)$ scaling in operations count, as predicted by the FMM theory, is obtained. For these reasons, we implemented this scheme in a new Fortran-90 code (FVFPS, a Fortran Version of a Fast Poisson Solver), and then parallelized it by using the MPI procedures. Here, we start up by outlining the main characteristics of Dehnen's algorithm. Then we will present our FVFPS implementation and its parallelization.

Scheme of Dehnen's Poisson solver

Dehnen's scheme is based on a hierarchical tree of cubic cells as well as the BH86 tree-code, while the method for the force evaluation is taken from the FMMs. In this case, the cells are both “sources” and “sinks” of the gravity interaction. This symmetry assures that the Newton's third law is satisfied (and consequently the linear momentum conserved) by construction. The force is approximated with a Taylor expansion with fixed truncation order (usually $p = 3$), while the accuracy is regulated only through the expansion parameter l/D .

Clearly, also the Taylor expansion of the potential reflects the symmetry of this approach, resulting quite different when compared with equation (4.13). Following D02, we consider two cells A and B , with centers of mass \mathbf{z}_A and \mathbf{z}_B , and two particles in \mathbf{x} and \mathbf{y} , in A and B , respectively. The (truncated) Taylor expansion of the Green's function (or of the adopted softening kernel) about $\mathbf{r}_0 = \mathbf{z}_A - \mathbf{z}_B$ is

$$g(\mathbf{x} - \mathbf{y}) = \sum_{n=0}^p \frac{1}{n!} (\mathbf{x} - \mathbf{y} - \mathbf{r}_0)^{(n)} \odot \nabla^{(n)} g(\mathbf{r}_0). \quad (4.25)$$

The potential at \mathbf{x} (in A) due to all the particles in B can be computed approximately as

$$\Phi_{B \rightarrow A} = - \sum_{l=0}^p \frac{1}{l!} (\mathbf{x} - \mathbf{z}_A)^{(l)} \odot \mathbf{C}_{B \rightarrow A}^{l,p}, \quad (4.26)$$

where the tensor field

$$\mathbf{C}_{B \rightarrow A}^{l,p} = \sum_{n=0}^{p-l} \frac{(-1)^n}{n!} \nabla^{(n+l)} g(\mathbf{r}_0) \odot \mathbf{M}_B^n \quad (4.27)$$

represents gravity, and

$$\mathbf{M}_B^n = \sum_i m_i (\mathbf{y}_i - \mathbf{z}_B)^{(n)} \quad (4.28)$$

are the multipole moments of the cell B . Note that we adopted the same notation as in equations (4.13) and (4.14). The multipole expansion is truncated at the order $p = 3$. Clearly, for the symmetry of the interaction, A acts also as a source of gravity and B as a sink. Thus, the approximated potential generated by A at ant point in B is computed again through a set of equations like (4.26 - 4.28), where A replaces B and vice versa.

Dehnen's scheme benefits also by a new opening criterion, called *multipole-acceptance criterion* (MAC; D02), which determines whether two nodes are well separated. Note that the MAC is characterized by an intrinsic symmetry, i.e., it satisfies the necessary requirement that if node A interacts with node B then node B interacts with node A . To introduce the MAC it is first necessary to define, for each node, a characteristic radius r_{\max} . If d_{\max} is the separation between the center of mass \mathbf{z} of a given node and its most distant corner, the associated r_{\max} is the minimum between d_{\max} and

$$\max\{r_{i,\max} + |\mathbf{z} - \mathbf{z}_i|\}, \quad (4.29)$$

where $r_{i,\max}$ and \mathbf{z}_i are the characteristic radius and the center of mass of the i -th sub-node, respectively, and the maximum is computed among all the sub-nodes of the considered node. Then, according to the MAC, two nodes (A and B) are well separated if

$$D > r_{A,\text{crit}} + r_{B,\text{crit}}, \quad (4.30)$$

where D is the distance between the two centers of mass, $r_{\text{crit}} = r_{\max}/\theta$, and θ is the *tolerance parameter*. Note that, since bodies (i.e., nodes with one particle) have $r_{\max} = r_{\text{crit}} = 0$, in the case of body-cell interaction equation (4.30) is analogous to the BH86 opening criterion (equation 4.12). For this reason, following D02, we indicate with the same notation the tolerance parameter and the BH86 opening angle. Note however that θ has not exactly the same meaning in equation (4.12) as in equation (4.30): in general the MAC requires smaller values of θ than the BH86 opening criterion, in order to attain the same accuracy (see Section 4.3.3). As will be shown by the tests described in Section 4.4, the MAC gives a substantial

contribute to the high level of performance of the code, by increasing the number of approximated calculations, without affecting significantly the overall accuracy.

A new, mass dependent control parameter $\theta = \theta(M)$ has also been introduced, that assures faster performances and a more uniform error distribution. The $\theta(M)$ function is given in implicit form by

$$\frac{\theta^5}{(1-\theta)^2} = \frac{\theta_{\min}^5}{(1-\theta_{\min})^2} \left(\frac{M}{M_{\text{tot}}} \right)^{-\frac{1}{3}}, \quad (4.31)$$

where θ_{\min} (the minimum value of θ , associated with the total mass M_{tot} of the N -body system) enters as a new, preassigned control parameter, and where M is the mass enclosed in a cell. $\theta(M)$, as given in equation (4.31), implies that, in the considered case of multipole expansion truncated at the third order of the force exerted by the cell, the *absolute* errors are roughly independent of the mass of the cell. On the contrary, in case of constant θ the *relative* error is the same for all the cells, so that the most massive cells are responsible for most of the total error of the interactions.

The resulting force solver is then organized as follows:

(a) As in the BH86 code, an oct-tree structure of nested cells containing particles is first constructed. A generic cell A , when acting as a gravity source is characterized by the position of its center of mass \mathbf{z}_A , by its critical size $r_{A,\text{crit}}$, mass M_A , and by the multipole tensor \mathbf{M}_A^2 . On the other hand, a set of 20 Taylor coefficients C_A are used to store the potential and acceleration values at \mathbf{z}_A , for the same cell A considered as gravity sink.

(b) To compute these coefficients, a new procedure for the tree exploration has been designed: starting from the root cell, all pairs of cells (A, B) satisfying the acceptance condition (4.30) are looked for in a sequential way. When the condition is satisfied, each cell of the selected pair accumulates the resulting interaction contributions in $C_A(B)$ or $C_B(A)$. In case of nearby cells (not satisfying the acceptance condition), the bigger cell of the pair is split, and the new set of pairs is then considered. The Author, by using a stack structure to order the visited cell-pairs, has introduced a powerful and efficient new algorithm able to perform this *interaction phase* in the force computation.

(c) Once all the cell-cell interactions have been computed and stored in the C_A array, a final step is needed to evaluate the gravitational potential and the accelerations of the particles in the (generic) cell A . This *evaluation phase* can be performed by a simple and fast $O(N)$ tree-traversal.

Clearly, for cells containing a small number of particles the approximated method can be more time-expensive than the direct summation. Thus, this latter method in the interaction phase [step (b)] is preferred in these cases. For example, for sufficiently large values of the total number of particles N (typically $N \gtrsim 10^4$), an additional criterion is adopted: cells containing less than 6 particles are not split. Moreover, the force is calculated by direct summation also in case the product of the number of particles in two interacting nodes does not exceed N_{cc} and N_{bc} , for cell-cell and body-cell interactions, respectively. As a general rule, the values $N_{\text{cc}} = 16$ and $N_{\text{bc}} = 100$ give good efficiency. A similar criterion is adopted for the cell self-interaction, which is computed by direct summation for cell containing less

than N_{cs} particles (with, e.g., $N_{\text{cs}} = 64$; see D02 for details).

Our Fortran-90 parallel implementation (FVFPS)

In our Fortran-90 implementation of the scheme above (FVFPS), we followed rather closely the algorithms as described in D02: at this stage of development and testing, we have neither attempted to optimize our implementation, nor to look for particular tricks to save computational time.

For the parallelization of the force solver, we have adopted a straightforward strategy, by first decomposing the physical domain into a set of non-overlapping subdomains, each containing a similar number of particles (a few per cent of tolerance is allowed). The set of particles in each subdomain, S_k , is then assigned to a specific processing unit, P_k . Each processor builds its own tree [step (a)], and computes the interaction phase for all the particles in its subdomain [step (b)]. Steps (a) and (b) are executed in parallel. By ordering the processors in a one-dimensional periodic chain, it is then possible to exchange (particles and tree-nodes) data between them, by a “`send_receive`” MPI routine, in such a way that each processor can compute the interaction phase with the other subdomains. This phase is performed by the following computational steps:

(i) The P_k processor sends its source-data to P_{k+s} and receives from the P_{k-s} a copy of its source-data, where $s = 1, 2, \dots, N_{\text{PE}}/2$, and N_{PE} is the total number of processors.

(ii) At any given level s , each P_k computes, again in parallel, the interaction phase with particles and cells of P_{k-s} . Mutuality of the interactions allows to evaluate, at the same time, the results of these interactions for cells and particles of processor P_{k-s} , which are stored as sink-data.

(iii) These accumulated sink-data (acceleration for particles and Taylor’s coefficients for cells) are sent back to the P_{k-s} processor, while the corresponding sink-data of the P_k processor are received from processor P_{k+s} and added to the current P_k values. In this way, it is evident that by repeating step (ii) $N_{\text{PE}}/2$ times and step (iii) $N_{\text{PE}}/2 - 1$ times, the interactions of P_k particles with all other particles in the domain are recovered.

(iv) The final evaluation phase [step (c)], being fully local, is performed in parallel.

Besides the force solver, the N -body code has been completed by a standard leapfrog time integrator, with a *drift-kick-drift* scheme (see equations 4.21 - 4.23). We adopt a (uniform) time step Δt , determined adaptively using a local stability condition dependent on the maximum of particle density (see Section 4.3.2). The potential is softened with a linear spline, i.e., it is given by equation (4.18) where now h_1 substitutes h_3 and the softening kernel is

$$g_{\text{spl1}}(x) = \begin{cases} -\frac{1}{2}(3 - x^2), & (x < 1), \\ \frac{1}{x}, & (x \geq 1). \end{cases} \quad (4.32)$$

In this case the equivalent Plummer softening is $\varepsilon = h_1/1.5$ (see Section 4.3.1). Optionally, also a quadratic spline is implemented, with smoothing parameter h_2 ,

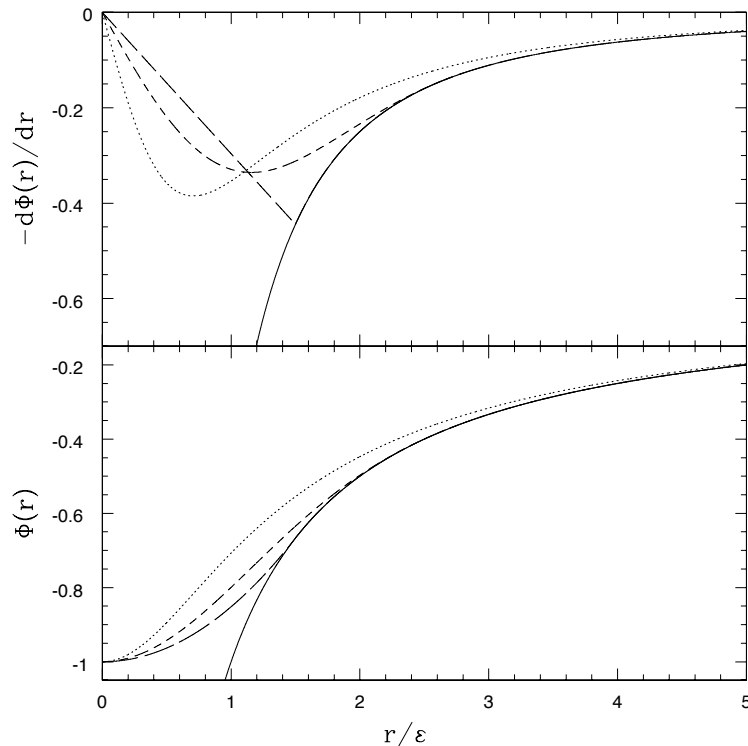


Figure 4.1: Softened force per unit mass (upper panel) and potential (lower panel) for Plummer (dotted curves), linear spline (long dashed curves) and cubic spline (short dashed curves) softening. We assumed $h_1 = 1.5\varepsilon$ and $h_3 = 2.8\varepsilon$. For comparison the Newtonian force and potential are plotted (solid curves).

smoothing kernel

$$g_{\text{spl2}}(x) = \begin{cases} -\frac{1}{8}(15 - 10x^2 + 3x^4), & (x < 1), \\ \frac{1}{x}, & (x \geq 1), \end{cases} \quad (4.33)$$

and equivalent Plummer softening $\varepsilon = 8h_2/15$.

4.3 Choosing the parameters of the codes

As already pointed out, the three codes presented above belong to the family of the tree-codes, characterized by three fundamental parameters: the softening length, the time-step, and the opening angle. We now discuss the criteria that we follow in the choice of the values of these parameters in our simulations.

4.3.1 The softening length

The problem of finding the optimal value of the softening parameter in N -body simulations has been studied in detail in the literature (see, e.g., Merritt 1996, Athanassoula et al. 2000, Dehnen 2001). The main conclusion of these studies

is that this optimal softening length can be obtained with a compromise between reducing the artificial fluctuations due to the discreteness of the system (*variance*) and limiting the deviations from the Newtonian force (*bias*). In other words, the error in the evaluation of the forces is dominated by the numerical noise, for small values of the softening parameter, while by the modification of the Newtonian potential, for large values (Dehnen 2001). From a quantitative point of view, the optimal value of the softening length is usually determined by minimizing the *mean integrated square error* (MISE), which is a measure of the deviation of the approximated force field with respect to the force field generated by the underlying smooth density distribution (see, e.g., Merritt 1996). Owing to this definition, the value of the optimal softening length depends on the particular density distribution, besides on the number of particles. Dehnen (2001) has computed for a few density distributions (as, for example, for one-component $\gamma = 1$ models) the values of the softening parameter that minimize the MISE, as a function of the softening method and of the number of particles.

As already pointed out in Section 4.2, each of the codes used in our simulations adopts a different form of the softened potential: a Plummer softening (with softening length ε) for the BH86 tree-code, a cubic spline (with softening length h_3) for GADGET, and a linear spline (with softening length h_1) for our FVFPS code. The three parameters ε , h_3 , and h_1 have then different meaning and their values can be related, for example, by imposing that the minimum of the softened potential is the same in the three cases. Thus, the “equivalent” Plummer softening length is $\varepsilon = h_3/2.8$ and $\varepsilon = h_1/1.5$, in the case of cubic and linear spline, respectively. In Fig. 4.1 are plotted, in the lower panel, the three normalized softened potential and, for comparison, the Newtonian potential; the upper panel shows the corresponding forces.

On the basis of the results of Dehnen (2001), we assume as optimal Plummer softening, for a $\gamma = 1$ model with N particles and core radius r_c , $\varepsilon_{\text{opt}}/r_c = 0.017(N/10^5)^{-0.23}$. In the case of linear and cubic spline we adopt $h_{1,\text{opt}}/r_c = 0.05(N/10^5)^{-0.2}$ and $h_{3,\text{opt}}/r_c = 0.06(N/10^5)^{-0.2}$, respectively. As outlined above, ε_{opt} , $h_{1,\text{opt}}$, and $h_{3,\text{opt}}$ depend on the particular density distribution of the simulated systems. The general trend is that more concentrated models require smaller softening length. In what follows, when we consider $\gamma = 0$, $\gamma = 2$ and (1,1) models, we will indicate case by case the values of ε , h_1 and h_3 adopted in the simulations, on the basis of the previous discussion and of several numerical tests.

4.3.2 The time-step

The time integration in the used N -body codes is done with a leapfrog scheme (see, e.g., Quinn et al. 1997). As already outlined, the time-step parameter Δt is assumed constant in the considered implementation of the BH86 tree-code, while it varies during the simulation, and from particle to particle, in GADGET; in our FVFPS code Δt is the same for all particles, but is allowed to vary adaptively during the evolution of the system. We recall that the leapfrog integrator is symplectic (i.e., it is an exact solution of a Hamiltonian system) if Δt does not change from particle to particle, while this is not true in general for particle-dependent time-steps. Symplecticity implies the conservation of the phase-space volume between

subsequent steps and time-reversibility, which are of course desirable properties in N -body codes. For this reason, in schemes with different time-steps for single particles, the simple leapfrog integrator need to be implemented with some care, in order to be at least quasi-reversible (see, for a discussion, Quinn et al. 1997, SYW01).

A problem common to all the integrators, both with fixed and with variable time-step, is the choice of the value of Δt . Of course, in any case, the smaller is the time-step the more accurate is the simulation. However it is obvious that too small time-steps imply high computational costs, since the number of steps scales as $\propto 1/\Delta t$. Then we need a criterion to find the maximum Δt compatible with the desired accuracy. We report here a simple derivation of a widely used criterion, based on the evaluation of the local density. Linearizing the equations of motion of a particle with position \mathbf{x} and velocity \mathbf{v} , in a density distribution $\rho(\mathbf{x})$ generating a potential $\Phi(\mathbf{x})$, we obtain

$$\delta\dot{\mathbf{x}} = \mathbf{v}, \quad (4.34)$$

$$\delta\dot{\mathbf{v}} = -\delta\nabla\Phi(\mathbf{x}) = -\nabla^2\Phi(\mathbf{x})\delta\mathbf{x}, \quad (4.35)$$

where $\delta\mathbf{x}$ and $\delta\mathbf{v}$ are the position and velocity increments, respectively. By combining these two equations with the Poisson equation

$$\nabla^2\Phi = 4\pi G\rho, \quad (4.36)$$

it follows

$$\delta\ddot{\mathbf{x}} + 4\pi G\rho(\mathbf{x})\delta\mathbf{x} = 0, \quad (4.37)$$

which is the equation of an harmonic oscillator with $\omega^2 = 4\pi G\rho(\mathbf{x})$. Then the local dynamical time at \mathbf{x} is

$$T_{\text{loc}}(\mathbf{x}) = \frac{1}{\omega} = \frac{1}{\sqrt{4\pi G\rho(\mathbf{x})}}. \quad (4.38)$$

A suitable time-step for a particle at \mathbf{x} is then a fraction of the local dynamical time, namely

$$\Delta t = \eta T_{\text{loc}}(\mathbf{x}), \quad (4.39)$$

where η is a parameter to be determined on the basis of the required accuracy, typically of the order of $\eta \sim 0.3$.

Other time-step criteria can be obtained by constraining the higher order terms in the change of the phase-space variables between subsequent steps (SYW01). For example, from equations (4.21-4.23) we obtain the particle displacement

$$\Delta\mathbf{x} = \mathbf{x}_{n+1} - \mathbf{x}_n = \mathbf{v}_n\Delta t + \frac{1}{2}\mathbf{a}_{n+1/2}\Delta t^2, \quad (4.40)$$

and the specific kinetic energy change

$$\Delta E_{\text{kin}} = \frac{1}{2}v_{n+1}^2 - \frac{1}{2}v_n^2 = \mathbf{v}_n \cdot \mathbf{a}_{n+1/2}\Delta t + \frac{1}{2}a_{n+1/2}^2\Delta t^2, \quad (4.41)$$

where $v = |\mathbf{v}|$ and $a = |\mathbf{a}|$. By imposing that the second order term in equation (4.40) does not exceed a certain length l (related to the softening parameter), we obtain

$$\Delta t = \sqrt{\frac{2l}{|\mathbf{a}|}}. \quad (4.42)$$

On the other hand, if in equation (4.41) the second order term is forced to be smaller than that of first order, it follows

$$\Delta t = \alpha_{\text{tol}} \frac{\sigma}{|\mathbf{a}|}, \quad (4.43)$$

where σ is a typical velocity dispersion of the system and α_{tol} is the tolerance parameter.

In the case of constant time-step (i.e., with the BH86 tree-code) we adopt for all the particles Δt given by equation (4.39), with T_{loc} substituted by the half-mass dynamical time of the system (see Section 3.3), and $\eta \lesssim 0.01$, depending case by case by the specific density distribution. Also in our FVFPS code we use the time-step criterion (4.39), where now in the definition (4.38) $\rho(\mathbf{x})$ is substituted by $\rho_{\text{MAX},i}$, the maximum density at the i -th step, and $\eta \lesssim 0.03$. As mentioned in Section 4.2.2, for GADGET simulations, characterized by time-steps variable also from particle to particle, we adopt the time-step criterion (4.43), where we assume σ of the order of the virial velocity dispersion of the system and $\alpha_{\text{tol}} \lesssim 0.1$. In addition, we use, as minimum and maximum allowed time-step, $\Delta t_{\text{min}} = 0$ and $\Delta t_{\text{max}} = 0.03T_{\text{dyn}}$, where T_{dyn} is the half-mass dynamical time of the system (see Section 3.3).

Finally, we note that the softening length and the time-step are strongly coupled parameters: in order to maintain the same accuracy in the force evaluation, Δt must be reduced if the softening length is reduced (Barnes & Hut 1989). It is then necessary to verify whether the combined choice of the two parameters is correct. This can be done a posteriori, for example by checking the conservation of the total energy over the time range spanned by the simulation.

4.3.3 The opening parameter

The opening parameter establishes whether the interactions are calculated directly or approximately. For this reason, it has a primary role in determining the accuracy in the calculation of the forces. As already pointed out in Section 4.2, each of the codes used for our simulations has a different opening criterion. As a consequence, the corresponding opening parameters (α for GADGET, θ for the BH86 tree-code and FVFPS) have different meaning. In any case, the smaller is the softening parameter the more accurate is the calculation of the force: in the extreme case $\alpha = 0$ or $\theta = 0$ the forces are always calculated via direct summation. It is clear that for smaller values of the opening parameter more computational time is needed. Thus, as it happens for the time-step, also the “optimal” value of the opening parameter is the maximum value compatible with the required accuracy.

On the basis of the results of some test simulations (see Section 4.4), we assume $\theta = 0.8$ for the simulations with the BH86 tree code, $\alpha = 0.02$ for those with

GADGET, and $\theta = 0.65$ for those with our FVFPS code (when adopting a unique value of the opening parameter for all the cells). We note in particular that the MAC requires smaller values of θ (but not larger computational time), with respect to the BH86 opening criterion, in order to attain the same accuracy. As pointed out in Section 4.2.3, in FVFPS it is possible to adopt a variable θ , whose dependence on the cell mass is given by equation (4.31): in this case the parameter determining the accuracy in force calculation is θ_{\min} . We find that $\theta_{\min} = 0.5$ corresponds, in terms of global accuracy, to constant $\theta = 0.65$.

4.4 Numerical tests

We performed several numerical tests in order to assess the reliability of our simulations and the errors associated to the measured quantities, for different codes and choices of the parameters. On the basis of these tests we determined, for each density distribution, the optimal values of the parameters that we adopt for the simulations. We report here the results of some test simulations where these values of the parameters are used. We consider in particular the dynamical evolution of an isolated isotropic one-component $\gamma = 1$ model and, as a second test simulation, the head-on merging of two isotropic one-component $\gamma = 1$ models.

4.4.1 Isolated one-component $\gamma = 1$ model

With each code we ran a simulation with initial conditions represented by an isolated (isotropic) one-component $\gamma = 1$ model with total mass M , core radius r_c and $N = 32768$ particles, over $100 T_{\text{dyn}}$, where T_{dyn} is the half-mass dynamical time (see Section 3.3). On the basis of the criteria discussed in Section 4.3, we adopt the following values of the parameters: $\varepsilon/r_c = 0.03$, $\Delta t = 0.01 T_{\text{dyn}}$, $\theta = 0.8$ for the BH86 tree-code, $h_3/r_c = 0.07$, $\alpha_{\text{tol}} = 0.05$, $\Delta t_{\min} = 0$, $\Delta t_{\max} = 0.03 T_{\text{dyn}}$, $\alpha = 0.02$, for GADGET, and $h_1/r_c = 0.05$, (initial) $\Delta t = 0.01 T_{\text{dyn}}$, $\theta_{\min} = 0.5$ for our FVFPS code.

With these parameters the total energy E of the system is preserved with deviations in any case smaller than 1%, over $100 T_{\text{dyn}}$. In the upper panel of Fig. 4.2 the quantity $|\Delta E/E| \equiv |E - E_0|/|E_0|$ is plotted as a function of time for the three simulations: dotted line for the BH86 code, dashed line for GADGET and solid line for FVFPS. In all the three simulations there is a slow secular drift in the total energy. The lower panel of Fig. 4.2 shows the evolution of the virial ratio $V = |2T/W|$, where T and W are the total kinetic and potential energy of the system. Deviation from the equilibrium value $V = 1$ are in the three cases smaller than 0.01 in modulus and do not show any significant trend over the whole simulation.

In Fig. 4.3 the density profiles at the end of the three simulations are plotted and compared with the theoretical density distribution of the one-component $\gamma = 1$ model (circles: BH86 code; squares: GADGET; triangles: FVFPS). It is apparent that the data follow the theoretical profile over a large radial range; as expected, deviations are observed at radii comparable with the softening length ($r/r_c \lesssim 0.1$).

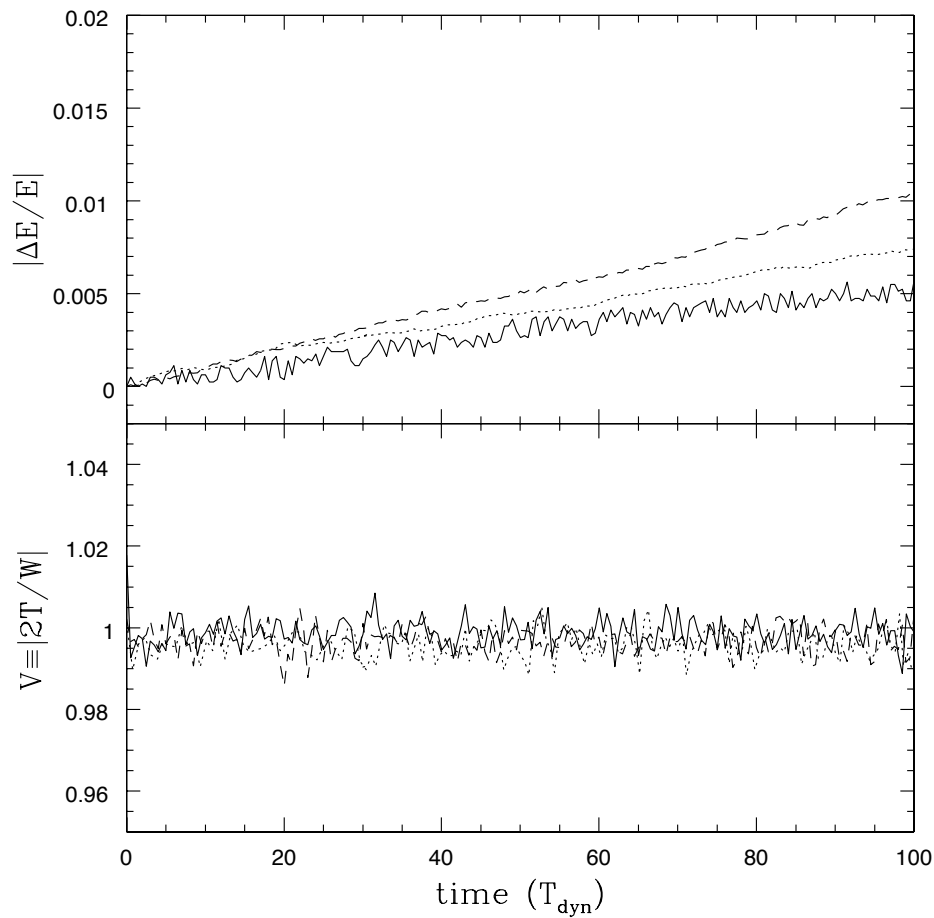


Figure 4.2: *Upper panel:* relative change in total energy as a function of time for the simulation of an isolated (isotropic) $\gamma = 1$ model with BH86 code (dotted line), GADGET (dashed line) and the FVFPS code (solid line). *Lower panel:* evolution of the virial ratio during the same three simulations.

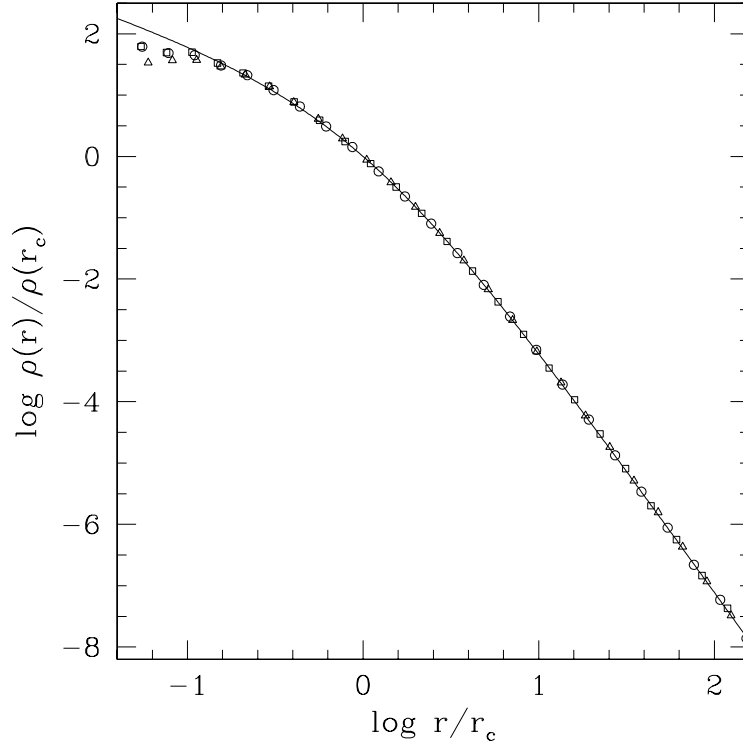


Figure 4.3: Density profile at the end of the simulation of an isolated (isotropic) $\gamma = 1$ model with BH86 code (circles), GADGET (squares) and the FVFPS code (triangles). The theoretical density profile of the $\gamma = 1$ model is plotted for comparison.

4.4.2 Merging of two $\gamma = 1$ models

The initial conditions of this test simulation are represented by two (isotropic) $\gamma = 1$ models with the same mass $M_1 = M_2 = M$ and scale length r_c . Each model is realized with $N = 32768$ particles. At the time $t = 0$ the relative separation between the centers of mass of the two models is $d_{\text{rel}} = 50r_c \simeq 3r_{90}$ (r_{90} is the radius enclosing the 90% of the total mass of each galaxy) and the modulus of their relative velocity is $v_{\text{rel}} = \sqrt{2G(M_1 + M_2)/d_{\text{rel}}} = 2\sqrt{GM/d_{\text{rel}}}$. The system has vanishing angular momentum and interaction energy. We performed this test with the three codes adopting the same parameters as in the case of the evolution of an isolated $\gamma = 1$ model (see Section 4.4.1).

In Fig. 4.4 we plot the change in total energy $|\Delta E/E|$ (upper panel) and the virial ratio V (lower panel), as a function of time, for the simulations with the three codes. As in the case of isolated galaxy model, described in Section 4.4.1, for the three codes $|\Delta E/E| \lesssim 0.01$, over $100 T_{\text{dyn}}$. We note that the small deviation from $V = 1$ at the end of the simulation is due to the contribution of escapers; the end-products, constituted by bound particles only, are perfectly virialized. The merger remnants relative to the simulations with the different codes are practically indistinguishable, in three-dimensional shape, angle-averaged half-mass radius, density and velocity dispersion profiles. The angle-averaged density profiles of the end-products in the three cases are shown in Fig. 4.5.

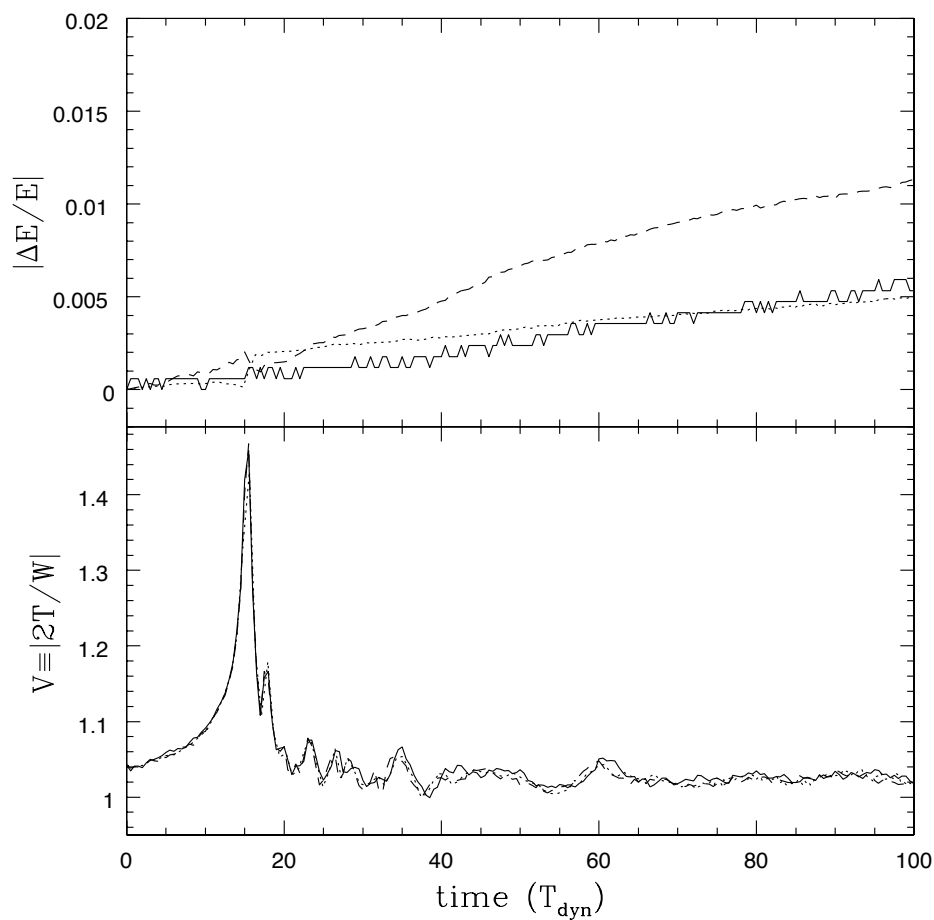


Figure 4.4: *Upper panel:* relative change in total energy as a function of time for the simulation of the head-on merging of two (isotropic) $\gamma = 1$ models with BH86 code (dotted line), GADGET (dashed line) and FVFPS (solid line). *Lower panel:* evolution of the virial ratio during the same three simulations. Note the different plotted range in V , with respect to Fig. 4.2, lower panel.

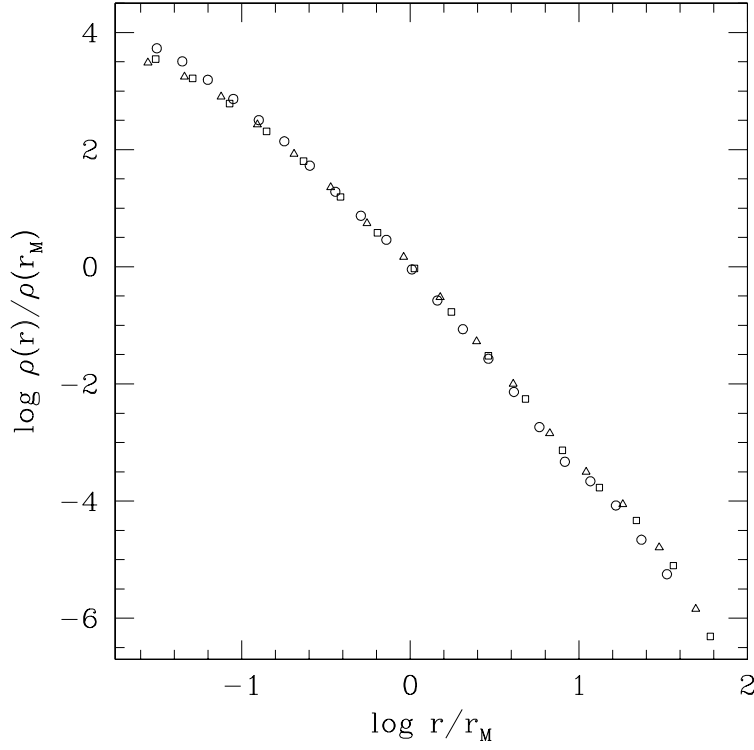


Figure 4.5: Angle-averaged density profile of the remnant of the merging of two (isotropic) $\gamma = 1$ models with BH86 code (circles), GADGET (squares) and FVFPS (triangles). r_M is the angle-averaged half-mass radius.

4.4.3 Performance of the FVFPS code

Scalar version

We ran some test simulations in order to estimate the performance of our Fortran-90 code (FVFPS) and compare it with the original C++ version (falcON; D02) and with the BH86 tree-code. We focus first on the analysis of the time efficiency in force calculation, considering scalar simulations of a galaxy group, where each galaxy is represented by a one-component $\gamma = 1$ galaxy model, for various values of the total number of particles N . In particular, we note that in the simulations with our FVFPS code and with falcON the opening parameter is $\theta = \theta(M)$, with $\theta_{\min} = 0.5$, while for the BH86 code (constant) $\theta = 0.8$ is used. We ran our simulations on a Pentium III/1.133 GHz PC. For falcON and for the BH86 code we refer to the data published by D02, who used a Pentium III/933 MHz PC.

In Fig. 4.6 we plot the time efficiency of the codes as a function of the number of particles; it is apparent from the diagram that our FVFPS code (solid line), as well as falcON (dashed line), reaches an effective $O(N)$ scaling, for $N \gtrsim 10^4$. In addition, we note that the Fortran-90 version is slower than the C++ version of a factor ~ 1.5 , for large N . We think that this discrepancy is due to differences in the details of the implementation, but also reflects a better intrinsic efficiency of the C++ with respect to the Fortran-90 for this kind of algorithms. In Fig. 4.6 are also plotted the

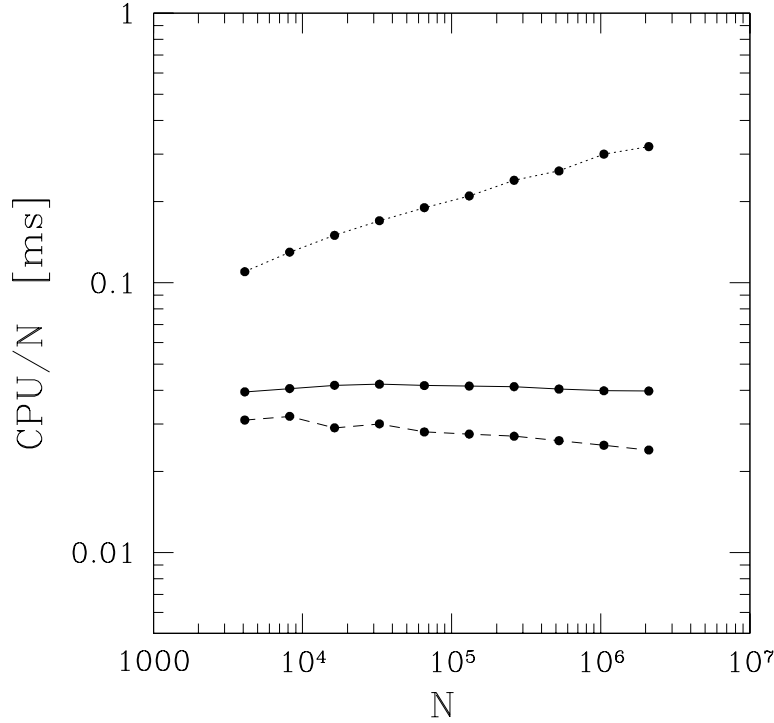


Figure 4.6: CPU time per particle as a function of total number of particles for the BH86 tree-code (dotted line), the falcON code (dashed line; data from D02), and the FVFPS code (solid line). The opening parameter is $\theta = 0.8$ for the BH86 code, and $\theta = \theta(M)$ with $\theta_{\min} = 0.5$ in the last two cases.

data relative to the BH86 tree-code (dotted line), whose $O(N \log N)$ scaling implies an increase of the CPU time per particle for increasing N . It is apparent from the figure that, for fixed N , the BH86 tree-code is significantly slower than the new scheme: for example for $N \simeq 10^5$ the FVFPS code is faster of a factor ~ 8 . Therefore, even if the present Fortran-90 implementation does not yet appear to be optimal, it gives further support to the efficiency of the D02 scheme, independently of the adopted programming language and of the implementation details.

The accuracy of the codes, for given parameters, can be evaluated through the mean relative error on the acceleration

$$\left\langle \frac{\Delta a}{a} \right\rangle \equiv \frac{1}{N} \sum_{i=1}^N \frac{|a_{\text{approx}}^i - a_{\text{direct}}^i|}{a_{\text{direct}}^i}, \quad (4.44)$$

and the corresponding 99th percentile $(\Delta a/a)_{99\%}$. In Fig. 4.7 we plot, as a function of N , $\langle \Delta a/a \rangle$ (solid circles) and $(\Delta a/a)_{99\%}$ (empty squares), for the FVFPS code (solid lines) and, for comparison, for falcON (dashed lines). As usual, the reference acceleration values a_{direct}^i are evaluated by direct summation of the exact two-body Green's function. In these tests, we have considered simulations having as initial condition an isolated one-component $\gamma = 1$ galaxy model, again with $\theta = \theta(M)$, and $\theta_{\min} = 0.5$. In any case $\langle \Delta a/a \rangle$ and $(\Delta a/a)_{99\%}$ do not exceed a few 10^{-3} and

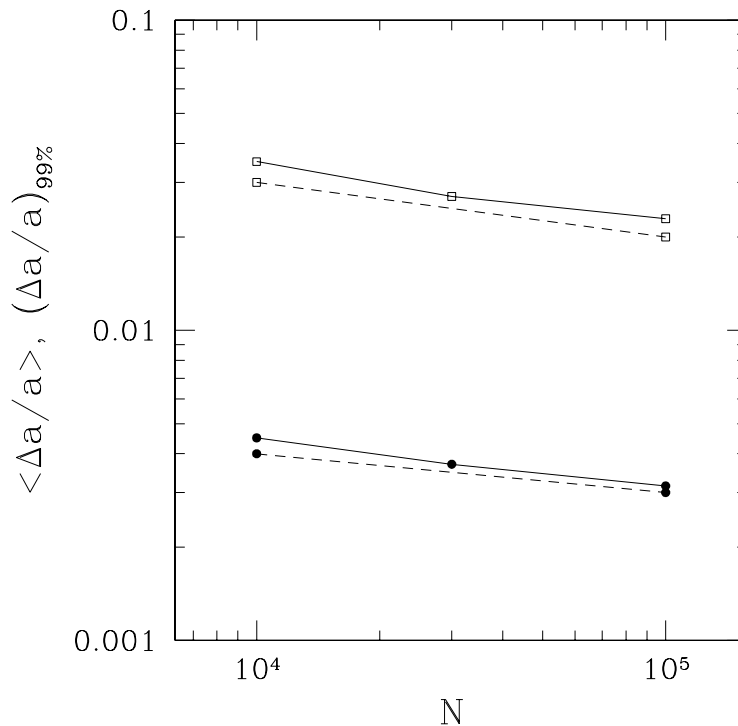


Figure 4.7: Mean error on the force calculation (solid circles) and corresponding 99th percentile (empty squares) as a function of the number of particles for falcON (dashed line; data from D02), and FVFPS (solid line).

a few per cent, respectively: this accuracy is considered sufficient for astrophysical applications (see, e.g., Capuzzo-Dolcetta & Mocchi 1998). We recall here that the BH86 tree-code with (constant) $\theta = 0.8$ has mean relative errors of the order of $\sim 5 \times 10^{-3}$ for $N \sim 10^4$ (see, e.g., Hernquist 1987), i.e., it is roughly as accurate as the new scheme with $\theta = \theta(M)$, and $\theta_{\min} = 0.5$.

Parallel version

As outlined in Section 4.2.3, we parallelized our code by using a domain decomposition with a load balancing essentially based only on particles number on each subdomain. We find that this load balancing criterion works quite well, taking advantage of the intrinsic $O(N)$ scaling in operations count of the basic scheme. In order to check the performance of the parallel version of the FVFPS code, we ran some simulations on a IBM Linux cluster (of Pentium III/1.133 GHz PCs), with a numbers of processors $N_{\text{PE}} \leq 16$. In this case the initial conditions are represented by a group of 8 one-component $\gamma = 1$ galaxy models with a total number of particles $N = 10^6$. As can be observed in Fig. 4.8, the considered parallelization is characterized by a good linear scaling of the CPU time per particle with the number of processors.

A more detailed analysis of the performance of our parallel FVFPS code can be obtained by considering the diagram in Fig. 4.9, where the different contributions

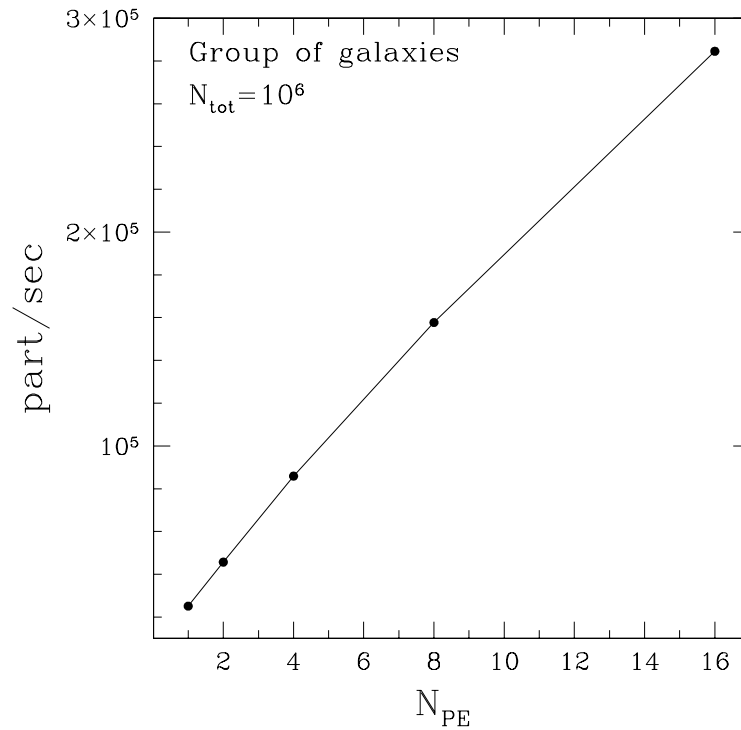


Figure 4.8: Number of particle processed per second as a function of the number of processor for the parallel FVFPS code. The data refer to simulations of a group of galaxies with total number of particles $N = 10^6$.

to the total CPU consumption are plotted. As expected, up to $N_{\text{PE}} = 16$ the main contribution comes from the force computation in each sub-domain (“self”), corresponding to the step (ii) of the parallel scheme outlined in Section 4.2.3. Among the other computations, the tree building [“tree”; step (i)] is important when few processors are used, while the contributions coming from the force evaluation among particles belonging to different subdomains (“cross”) and the cumulative time for all communication steps among processors (“trans”) increase with N_{PE} , but keep much smaller than force computation in each sub-domain in the chosen range of parameters (N, N_{PE}). Therefore, the $O(N)$ scaling of the base scheme, allows to estimate, for given N , the optimal configuration of the N_{PE} that can be used.

All the parallel simulations considered in this work were run on Cray T3E, on IBM SP3, and on IBM Linux cluster, with a number of processors in the range 4–32, depending on the code and on the number of particles. We ran the simulations with the scalar codes on Sun and Alpha workstations.

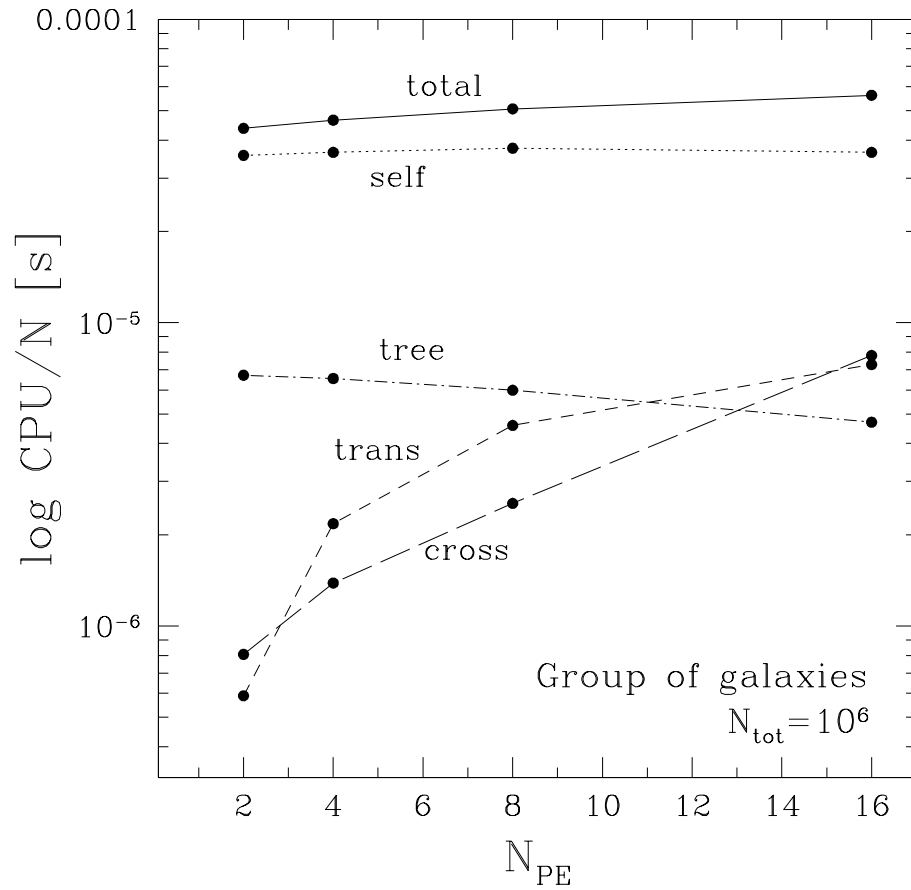


Figure 4.9: CPU time per particle as a function of the number of processors for the parallel code for the same simulations as in Fig. 4.8. The different contributions are plotted: tree building (“tree”), force computation in each sub-domain (“self”) and between different subdomains (“cross”), data transfer among the processors (“trans”), and total computational time (“total”).

5. Radial orbital anisotropy and the Fundamental Plane of elliptical galaxies

In the present Chapter we explore the interplay between radial orbital anisotropy and the Fundamental Plane of elliptical galaxies. As briefly discussed in Chapter 1, we will consider both the thickness and the tilt of the FP, taking into account explicitly the role of radial orbit instability.

5.1 Introduction

The FP relation (equation 2.5) implies that the effective radius and the central velocity dispersion of elliptical galaxies of given luminosity L_B must be strongly coupled: at any fixed luminosity the coordinates k_3 and k_1 are related through definitions (2.2) and (2.4) by

$$k_3 = \sqrt{\frac{2}{3}}k_1 + \sqrt{\frac{1}{3}}\log \frac{2\pi}{L_B}, \quad (5.1)$$

and the slope of this relation ($\simeq 0.82$) is different from that of the FP ($\simeq 0.15$). As a consequence, in the (k_1, k_3) plane all galaxies with the same luminosity are located on straight lines significantly inclined with respect to the FP. Thus, the presence of substantial scatter in galactic properties from galaxy to galaxy (of similar luminosity) would destroy the thinness of the FP by producing a large scatter in k_1 and so in k_3 .

The relation between galaxy properties and the FP can be expressed in a quantitative way under the reasonable assumption that present day ellipticals are virialized systems. We write the virial theorem as

$$\frac{GL_B\Upsilon_*}{\langle R \rangle_e} = K_V\sigma_0^2 \quad (5.2)$$

where $\Upsilon_* = M_*/L_B$ is the galaxy *stellar* mass-to-light ratio (for example in Blue solar units), and K_V is a dimensionless factor depending on the stellar density profile, internal dynamics, dark matter amount and distribution, and, for non-spherical galaxies, on their relative orientation with respect to the observer's line-of-sight

(see, e.g., Ciotti 1997); in addition, K_V depends also on the observing aperture adopted to derive σ_0 .

Equations (2.5) and (5.2) imply that, for galaxies belonging to the FP, the quantity Υ_*/K_V is a very well defined function of two⁵ of the three observables L_B , σ_0 , and $\langle R \rangle_e$. In the particular case of adopting the numerical coefficients of equation (2.5), measuring L_B in $10^{10} L_{B\odot}$, and taking into account that $k_1 = \log(G\Upsilon_* L_B / K_V) / \sqrt{2}$ and $k_3 = \log(2\pi G\Upsilon_* / K_V) / \sqrt{3}$,

$$\frac{\Upsilon_*}{K_V} \simeq 1.12 \times L_B^{0.23}, \quad (5.3)$$

where the quantity Υ_*/K_V is characterized by a scatter of $\simeq 20\%$ due to its relation with k_3 (however, additional considerations reduce this figure to $\simeq 12\%$, see Renzini & Ciotti 1993). As a consequence, any departure from the relation dictated by equation (5.3) will move a galaxy away from the FP. We recall here that the dependence of k_3 on k_1 , as given by equation (2.5) and responsible for the luminosity dependence of the ratio Υ_*/K_V , is commonly known as the FP “tilt”.

The simple analysis presented above shows that the two properties of thinness and tilt of the FP are deeply connected with the present-day structure and dynamics of Es, and, as a consequence, with their formation and evolution history: as we outlined in Chapter 1, the very existence of the FP [as well as of the other tight scaling relations revealing the remarkable homogeneity of Es, such as the M_{BH} - σ_0 (see Section 2.4), the Mg_2 - σ_0 (Bender, Burstein & Faber, 1993 and references therein) and the color-magnitude (Bower, Lucey & Ellis, 1992) relations] imposes strong constraints on the different formation and evolutionary scenarios proposed for Es (i.e., dissipationless merging, monolithic collapse, or a combination of the two; see, e.g., Ciotti & van Albada 2001).

Among the various galaxy properties in principle able to destroy the FP thinness (as a consequence of a substantial variation at fixed galaxy luminosity), one of the most “effective” is certainly orbital anisotropy (de Zeeuw & Franx 1991). Galaxy models are commonly believed to be able to sustain a large spread of orbital anisotropies and it is also well known that radial orbital anisotropy can produce very high *central* velocity dispersion values, and correspondingly low values of K_V , thus substantially violating equation (5.3). A natural question to be addressed is then what physical principle or evolutionary process limits the range of orbital anisotropies shown by real galaxies. Ciotti & Lanzoni (1997, hereafter CL97), using one-component, radially anisotropic Sersic (1968) models, and a semi-analytical investigation based on the Fridman & Polyachenko (1984, hereafter FP84) stability indicator, suggested the possibility that radial orbit instability could be the limiting factor of the FP thickness. In practice, CL97 found indications that galaxy models sufficiently anisotropic to be outside the FP observed thickness (when their parent isotropic model was assumed to lie on the FP) were unstable. Clearly, this preliminary indication requires a confirmation with the aid of numerical simulations and more realistic galaxy models (for example, allowing for the presence of live

⁵In principle one could find virialized galaxies *everywhere* in the three-dimensional observational $(L_B, \sigma_0, \langle R \rangle_e)$ space. From this point of view the existence of the FP is related to the virial theorem as the HR diagram is related to hydrostatic equilibrium: the useful information that one derives is *not* about the equilibrium equations, but the physics of the objects involved.

dark matter halos). Also, a question naturally associated with that above is the determination of the position of the end-products of unstable initial conditions in the space of the observables. One of the aims of this work is indeed to answer these two questions by numerical simulations of one and two-component radially anisotropic galaxy models.

Orbital anisotropy is not only related to the problem of the FP thinness but it is also one of the candidates that have been proposed to explain the origin of the FP tilt (Ciotti et al. 1996; CL97). If this were the case, the amount of radial anisotropy in the velocity dispersion tensor should increase with galaxy luminosity, as can be seen from equation (5.3) under the assumption of a constant Υ_* and of structural homology⁶ over the whole FP plane. In other words, in this scenario the FP tilt would be produced by a *dynamical* non-homology due to anisotropy (note that dynamical non-homology may well coexist with structural homology, but the converse is in general not true). Many interesting questions are raised by the scenario depicted above: for example, under the assumption that an isotropic galaxy of given luminosity lies on the FP, how far can the derived structurally homologous but radially anisotropic models climb over the FP before the onset of radial orbit instability? In addition, what happens to the end-products of the unstable models? Will they remain near the FP? In this work we try to address also these questions with the aid of N -body numerical simulations.

Strictly related to the clarification of the interplay between orbital anisotropy and the FP tilt, is the possibility to obtain some clues on the formation processes of Es. As we will show in details in Section 6.1, as consequence of the virial theorem and the conservation of the total energy, the *virial* velocity dispersion cannot increase in a merging between two galaxies, at least when the energy of the pair and the mass loss are negligible. On the other hand, the FP and the less tight Faber–Jackson relation (see Section 2.2) indicate that the *projected central* velocity dispersion increases with galaxy luminosity. Then, in the dissipationless merging scenario the FP tilt can be produced only by structural and/or dynamical non-homology, since the relation between central and virial velocity dispersion depends on the structure and dynamics of the system: in particular, in this Chapter we will discuss the second possibility, with regard to an increase in radial orbital anisotropy with galaxy luminosity. Note that an increase in the radial orbit amount has been claimed in the past as a natural by-product of galaxy merging, and also some observations have been interpreted in this way (Bender 1988; see also Naab, Burkert & Hernquist 1999, and references therein). With the aid of the explored numerical models we will try to obtain some qualitative insight in this problem: it is however clear that the results should be considered at the best qualitative indications, and that a firm answer about the role of merging in producing the FP tilt can be obtained only with N -body numerical simulations of merging galaxies like those described in Chapter 6.

Summarizing, the aims of this Chapter are the following. For what concerns the FP thickness problem, we investigate the role of radial orbit instability as a factor regulating the amount of radial anisotropy for galaxies of given luminosity, and the position, relative to the FP, of the end-products of radially unstable anisotropic

⁶With “structural homology” we mean that all the structural galaxy properties (e.g., the stellar and dark halo density profiles, the ratio of their scale-lengths and masses, and so on) *do not depend on* L_B .

models. In addition, we explore whether it is possible to reproduce the whole FP tilt with a systematic variation of radial anisotropy with luminosity (using both stable and unstable initial conditions), and what is the fate of unstable models initially forced to lie on the FP.

5.2 Numerical simulations

As initial conditions for the N -body simulations presented in this Chapter, we used spherically symmetric one-component γ -models (with $\gamma = 0, 1, 2$) and two-component (1,1) models with radial orbital anisotropy introduced with the Osipkov-Merritt (OM) parameterization (see Sections 3.1 and 3.2). We recall here that, for simplicity, the orbital distribution of the DM halos is assumed in any case isotropic. The initial particle distributions were realized as described in Appendix A.1. To run these simulations we used the BH86 treecode and the parallel version of GADGET (see Sections 4.2.1 and 4.2.2). In particular, the one-component simulations were run by using the BH86 tree-code with total number of particles $N = 32768$; for some of them we used also $N = 65536$. For the two-component models we used instead GADGET with $N = 131072$; in addition, some one-component models were also tested with $N = 131072$ using the same code. We found very good agreement between the test simulations performed with both the codes, with the basic properties of the simulated systems nearly independent of the adopted number of particles.

On the basis of the tests presented in Section 4.4, we adopted the following values of the parameters in the BH86 simulations: $\theta = 0.8$, $\Delta t = T_{\text{dyn}}/100$, and $\varepsilon/r_c = (0.072, 0.030, 0.016)$ for $\gamma = (0, 1, 2)$ models, respectively. In the two-component GADGET simulations we used $\alpha = 0.02$, $\Delta t_{\text{min}} = 0$, $\Delta t_{\text{max}} = T_{\text{dyn}}/100$, $\alpha_{\text{tol}} = 0.05$. The value of the softening length h_3 was determined according to the discussion in Section 4.3.1, considering case by case the core radius length of the more concentrated component.

In order to determine the “observational” properties of the end-products of the numerical simulations, and place them in the (k_1, k_2, k_3) space, we measured their effective radius $\langle R \rangle_e$, central velocity dispersion σ_0 and mean effective surface brightness $\langle I \rangle_e$ for several projection angles. The technical details of the adopted procedures are given in the Appendix A.2. A point of interest is the choice of the adopted “aperture radius” for the measure of σ_0 , fixed in this case to $\langle R \rangle_e/8$ in order to match the observational procedure at low redshifts (see, e.g., JFK96). Indeed, it is well known that isotropic γ -models may present a projected velocity dispersion profile decreasing towards the center (in contrast to what happens in the vast majority of elliptical galaxies): for example, the projected velocity dispersion of (isotropic) $\gamma = 1$ models peaks approximately at $R_e/5$, while the profile for (isotropic) $\gamma = 2$ models is monotonically decreasing (see Fig. 3.2). As a consequence, the position of the initial conditions and of the end-products in the k space could depend on the adopted aperture radius used to measure σ_0 . In order to assess the effect of this choice on our conclusions, we analyzed the results of the simulations also by using an aperture radius of $\langle R \rangle_e/4$, and we found very good agreement with the results obtained with the aperture $\langle R \rangle_e/8$: therefore, we present

Table 5.1: The dimensionless coefficient $K_V(\gamma, s_a)$ for one-component models, as obtained from equation (5.2). See Section 5.3 for the definitions of s_{ac} and s_{as} .

γ	$K_V(\gamma, \infty)$	$K_V(\gamma, s_{as})$	$K_V(\gamma, s_{ac})$
0	6.7	5.9	2.8
1	5.9	5.3	2.7
2	4.8	4.4	2.3

here only these last results. Note however that, by virtue of the projected virial theorem (see, e.g., Ciotti 1994), a totally different scenario from that explored in this Chapter would arise in the limiting case of σ_0 measured over the whole galaxy: anisotropy would play no role at all in determining the position of initial conditions in the k space, and any difference between initial and final σ_0 would be only due to projection effects associated with loss of spherical symmetry. These aperture effects could be important when studying observationally the FP at intermediate redshift (see, e.g., van Dokkum & Franx 1996, Bender et al. 1998, Treu et al. 1999), or locally by using large apertures (see, e.g., Graham & Colless 1997).

5.3 Orbital anisotropy and the FP thinness

As already pointed out in Section 2.1, the 1-sigma dispersion of the observational data around the best-fit relation (2.5) is surprisingly small and nearly constant over all the observed range in k_1 , with $\sigma(k_3) \simeq 0.05$. We investigate here the constraints imposed by this tightness on the amount of radial orbital anisotropy for a set of one and two-component galaxy models belonging to the family described in Section 3. We start up by fixing the values for the dimensionless parameters γ (for one-component models) and μ and β (for two-component models); we also assume global isotropy, i.e., $s_a \rightarrow \infty$, and in this way the quantity K_V is uniquely determined. These globally isotropic models (that we call *parent models*) are then placed on the FP by assigning of the pair (Υ_*, L_B) so that equation (5.3) is verified. From each of these parent models lying on the FP we then generate a *family* of OM radially anisotropic models by decreasing s_a , while maintaining fixed all the other model parameters. Correspondingly K_V decreases (as can be seen from Table 5.1, in the case of one-component models and for representative values of the parameter s_a), k_1 increases, and so does k_3 , according to equation (5.1): for sufficiently small values of s_a the members of each family are found outside the observed thickness of the FP. Note that by an appropriate choice of the pair (Υ_*, L_B) each parent isotropic model can be placed at arbitrary positions over the best-fit line (equation 2.5), and so the results of the numerical simulations (after a rescaling to Υ_* and L_B) are the same everywhere on the FP. In addition, since $\sigma(k_3)$ is constant over the whole observational range spanned by k_1 , the conclusions obtained from each family of models are also independent of the position of the parent galaxy on the FP.

Obviously all the isotropic models discussed in this work are stable (see, e.g., Binney & Tremaine 1987; Ciotti 1996), while for each family of models a critical value s_{as} for *stability* exists such that the initial conditions characterized by $s_a < s_{as}$ describe radially unstable configurations. From the point of view of the present

discussion, the critical value s_{as} corresponds, through $K_V(s_{\text{as}})$, to the maximum distance that a *stable* model can have from the FP, where its parent isotropic model lies at (say) $(k_1^{\text{iso}}, k_3^{\text{iso}})$. Clearly, initial conditions describing unstable models can be placed at larger distances from the FP: these initial conditions will evolve with time, and their representative points in the space of observables will also evolve with time, up to virialization. In particular, the coordinates $k_1(t)$ and $k_3(t)$ will evolve with time moving on the line described by equation (5.1). Note that the maximum distance from the FP at which unstable models can be placed is in general finite: the anisotropy radius of all physically acceptable (stable and unstable) galaxy models must satisfy the inequality $s_a \geq s_{\text{ac}}$, where $s_{\text{ac}} \leq s_{\text{as}}$ is the (dimensionless) critical anisotropy radius for *consistency* (i.e., the anisotropy limit for initial states with a nowhere negative DF); for a study of s_{ac} in γ -models and in (γ_1, γ_2) models see Carollo, de Zeeuw & van der Marel (1995a) and Ciotti (1996, 1999).

FP84 argued that a quantitative indication on the maximum amount of radial orbits sustainable by a specific density profile is given by the stability parameter $\xi = 2T_r/T_t$, where T_r and $T_t \equiv T_\theta + T_\varphi$ are the radial and tangential component of the kinetic energy tensor, respectively. From its definition $\xi \rightarrow 1$ for $s_a \rightarrow \infty$ (globally isotropic models), while $\xi \rightarrow \infty$ for $s_a \rightarrow 0$ (fully radially anisotropic models). The fiducial value indicated by FP84 as a boundary between stable and radially unstable systems is $\xi_s \simeq 1.7$. Unfortunately, the reliability of such indicator is not well understood, and indications exist of a significant dependence on the particular density profile under scrutiny (see, e.g., Merritt & Aguilar 1985; Bertin & Stiavelli 1989; Saha 1991, 1992; Bertin et al. 1994; Meza & Zamorano 1997). In any case, CL97 used this value to determine s_{as} for one-component Sersic (1968) models by solving the associated Jeans equations, and from this value they determined the maximum distance of stable models from the FP: all models characterized by $\xi < \xi_s$ were found inside the observed thickness of the FP. This finding can be considered at the best a qualitative indication, considering the uncertainties associated to the exact value of ξ_s and to its dependence on the specific density profile adopted, and the need of numerical simulations is clear.

With the aid of N -body simulations in the following two Sections we investigate how distant from the FP stable models of various families can be placed, by increasing their radial orbital anisotropy. The logically related question of what happens to the end-products of the unstable (but physically consistent) initial conditions is also addressed.

Due to its central role in the following discussion, it is important to quantify the concept of “distance” of a galaxy model from the FP. In general, we define distance of a point (k_1, k_3) from the FP the quantity $\delta k_3 \equiv |k_3 - 0.15k_1 - 0.36|$, i.e., the distance at fixed k_1 from the point and the FP itself: this quantity naturally compares with $\sigma(k_3)$. Unfortunately, as already discussed in Section 5.1, galaxy models of fixed luminosity move along inclined lines in the (k_1, k_3) space and so in the present exploration $|k_3 - k_3^{\text{iso}}|$ is *not* the distance from the FP. The relation between δk_3 and $|k_3 - k_3^{\text{iso}}|$ is however of immediate determination: from equation (5.1) $k_3 = k_3^{\text{iso}} + \sqrt{2/3}(k_1 - k_1^{\text{iso}})$, and from the assumption that the parent isotropic models are placed on the FP one obtains $\delta k_3 = (1 - 0.15\sqrt{3/2})|k_3 - k_3^{\text{iso}}| \simeq 0.816|k_3 - k_3^{\text{iso}}|$.

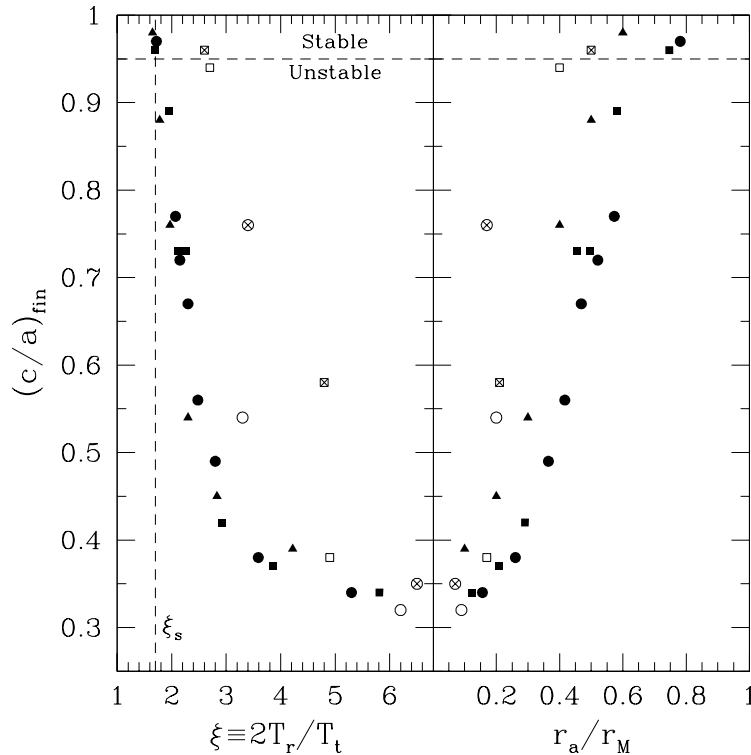


Figure 5.1: *Left*: final axis ratio $(c/a)_{\text{fin}}$ vs. the stability parameter $\xi \equiv 2T_r/T_t$ of initial conditions, for all the computed models. One-component models are represented by full symbols ($\gamma = 0$, circles; $\gamma = 1$, squares; $\gamma = 2$, triangles). Two-component (1,1) models are represented by empty symbols: squares correspond to concentrated halos ($\beta = 0.5$), circles to diffuse halos ($\beta = 2$). Crosses indicate models with massive halos ($\mu = 3$). *Right*: final axis ratio $(c/a)_{\text{fin}}$ vs. r_a/r_M for the same models shown in left panel. The vertical dashed line is located at $\xi_s = 1.7$ (FP84). Models above the horizontal dashed line are stable (see the text for a discussion).

5.3.1 One-component models

In order to answer to the questions outlined above, we performed a set of 21 simulations of one-component γ -models with $\gamma = (0, 1, 2)$, evaluating numerically for each of the three families the critical value for stability s_{as} . We recall here that in our simulations the onset of instability is just due to numerical noise produced by discreteness effects in the initial conditions, and that, at most, the simulations are interrupted after $100 T_{\text{dyn}}$. As a rule, in order to determine if a given model is unstable, we found useful to check its departures from spherical symmetry by monitoring the evolution of its intrinsic axis ratios c/a and b/a (where a , b and c are the longest, intermediate and shortest axis of its inertia ellipsoid associated to “bona fide” bound particles; see Appendix A.2): we found that numerical uncertainties (due to the finite number of particles) of these ratios never exceed 5%. According to this choice we define *unstable* the models for which the minimum c/a over $100 T_{\text{dyn}}$ is smaller than a fiducial threshold value, 0.95 (the horizontal dashed line in Fig. 5.1).

Also this value has been obtained by analyzing the fluctuations – due to the finite number of particles – of c/a shown by the numerical realizations of the isotropic (stable) parent γ -models. As expected, we found that an exact determination of s_{as} for a given density profile is not straightforward: while for strongly anisotropic initial conditions the onset of instability is apparent and the numerical models settle down into a final equilibrium configuration in a few dynamical times, for nearly stable initial conditions the instability can be characterized by very slow growth rates and its effects become evident even after $30 T_{\text{dyn}}$ (see also Bertin et al. 1994).

The results of the simulations are summarized in Fig. 5.1, where we plot for all models the final value of the axis ratio, $(c/a)_{\text{fin}}$, as a function of ξ (left panel) and r_a/r_M (right panel) of initial conditions (we recall here that r_M is the angle-averaged half-mass radius). A first result is that for one-component γ -models (full symbols) the ξ critical value is in the range $1.6 \lesssim \xi_s \lesssim 1.8$: for $\xi \lesssim 1.6$ all models were found stable up to $100 T_{\text{dyn}}$, while for $\xi \gtrsim 1.8$ all models present clear evolution on time-scales shorter than $30 T_{\text{dyn}}$. This range for ξ_s is compatible with the value 1.7, reported by FP84 and used in CL97, and with the results of Bertin et al. (1994), who estimated $\xi_s \simeq 1.58$ for the family of “ f_∞ models”; Meza & Zamorano (1997) found instead a higher threshold value for stability ($\xi_s \simeq 2.3$). When expressed in terms of r_a/r_M the critical value for stability is found in the range $0.6 \lesssim (r_a/r_M)_s \lesssim 0.8$. Finally, the stability limits expressed in terms of the (dimensionless) critical anisotropy radius (the quantity of direct interest in this work) are given by $s_{\text{as}} = (3.0, 1.8, 0.6)$ for $\gamma = (0, 1, 2)$ models, respectively; for comparison the critical anisotropy radius for consistency is $s_{\text{ac}} = (0.5, 0.2, 0.0)$; Ciotti 1999).

For what concerns the internal structure of the end-products of unstable initial conditions, we found (in accordance with previous results, see, e.g., Merritt & Aguilar 1985, Stiavelli & Sparke 1991) that they are in general prolate systems, with axis ratios in the range $0.3 \lesssim (c/a)_{\text{fin}} \lesssim 1$, consistent with the ellipticities of the observed galaxies. Only the most anisotropic models, near the consistency limit ($s_a \simeq s_{\text{ac}}$), form a triaxial bar. From Fig. 5.1 it is apparent that $(c/a)_{\text{fin}}$ is strongly anti-correlated with ξ (and so correlated with r_a/r_M), and this in a way essentially independent of the value of γ ; a similar decrease of $(c/a)_{\text{fin}}$ with s_a was also found in the numerical simulations of Meza & Zamorano (1997).

In order to better compare the end-products of unstable models with real galaxies, we also fitted their projected mass density profiles with the widely used Sersic (1968) $R^{1/m}$ law:

$$I(R) = I_0 \exp \left[-b(m) \left(\frac{R}{R_e} \right)^{1/m} \right] \quad (5.4)$$

where $b(m) \sim 2m - 1/3 + 4/405m$ (Ciotti & Bertin 1999; see also Appendix A.3). In Fig. 5.2 we plot the Sersic best fit parameter m as a function of ξ for a small, but representative, set of models. As for real galaxies, we found a significant dependence of m on the adopted radial range over which the fit is performed, while the value of m is not very sensitive to the specific fitting method adopted (see, e.g., Bertin, Ciotti & Del Principe 2002 and Appendix A.3). For example, in the radial range $0.1 \lesssim R/\langle R \rangle_e \lesssim 4$ we found $1 \lesssim m \lesssim 5$, with average residuals between the data and

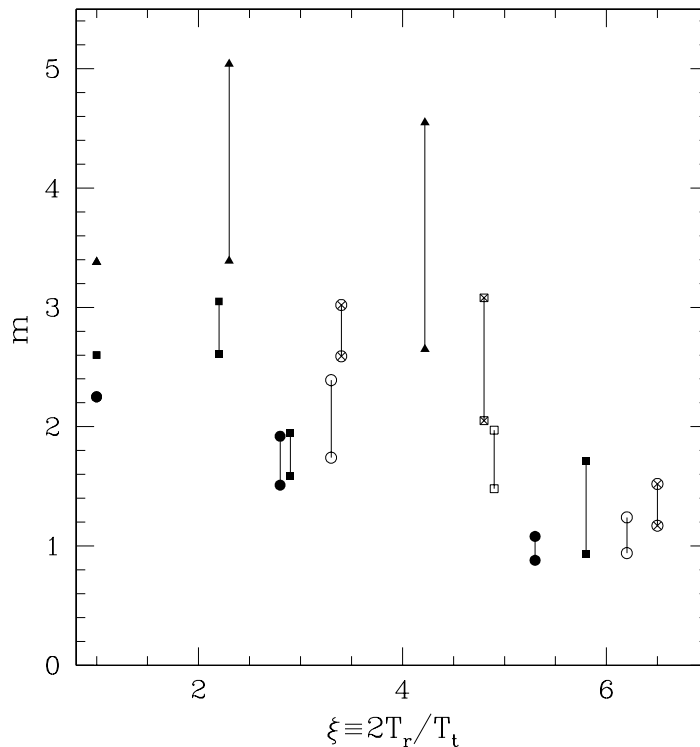


Figure 5.2: Sersic best fit parameter m vs. stability parameter ξ for a subset of the computed models. Symbols are the same as in Fig. 5.1. The three points at $\xi = 1$ give the value of m for the isotropic (stable and spherically symmetric) parent galaxies, while vertical bars show the maximum and minimum m for each model due to the relative orientation of the end-product and the line-of-sight.

the fits $\langle \Delta\mu \rangle \simeq 0.02 - 0.14 \text{ mag arcsec}^{-2}$. Clearly, the fitted quantities m and $\langle R \rangle_e$ depend on the relative orientation of the line-of-sight and of the end-products of the simulations: with the vertical bars in Fig. 5.2 we indicate the range of values spanned by m when projecting the final states along the short and long axis of their inertia ellipsoids. As an example of fit for a specific model, in Fig. 5.3 we show the data relative to the initial conditions of an unstable $\gamma = 1$ model, and to the two projections of its end-product.

Having determined for each family of galaxy models the critical anisotropy radius, we can now proceed to check how distant from the FP stable models can be placed, and where the end-products of unstable initial conditions are found. Of course, in this second case the coordinates in k -space depend on the line-of-sight orientation with respect to the density distribution of the end-products, and the dependence is expected to be stronger for smaller values of $(c/a)_{\text{fin}}$: to any unstable initial condition corresponds, in the k -space, a *set* of points. Due to the fact pointed out above that the properties of the models here investigated do not depend on the specific position of the parent galaxy on the FP, in Fig. 5.4 we plot the obtained results in a coordinate system that reflects this property, and allows for an immediate visualization of the most important consequences derived from the simulations; in

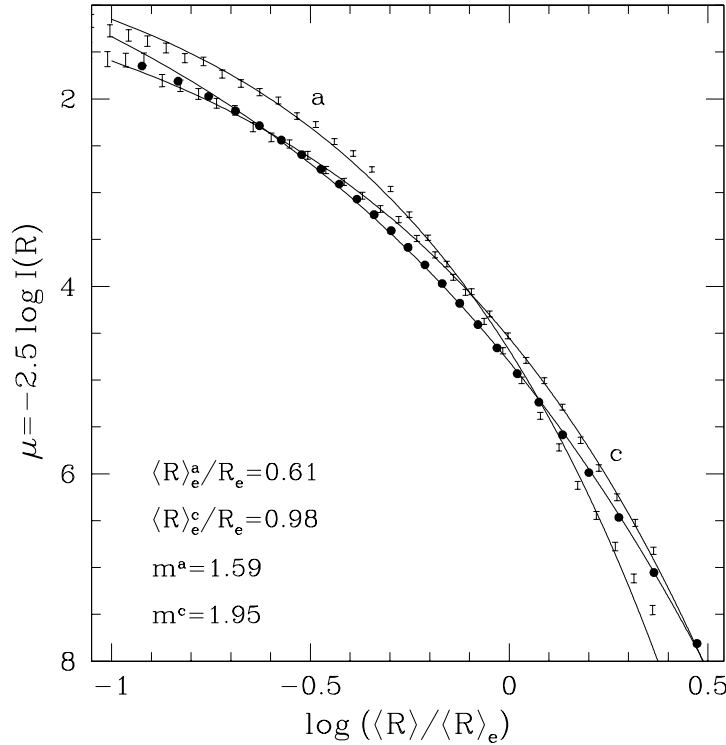


Figure 5.3: Circularized surface brightness profiles (vertical bars) of the end-product of the unstable one-component $\gamma = 1$ model with $s_a = 0.7$. R_e is the effective radius of the (spherically symmetric) initial condition (solid dots), while $\langle R \rangle_e \equiv \sqrt{a_e b_e}$ is the circularized effective radius. Solid lines represent the best fit Sersic models of the end-product projections along its inertia ellipsoid minor (*c*) and major (*a*) axis.

Fig. 5.5 the behavior of a representative set of models is shown in the standard (k_1, k_2, k_3) space. In the horizontal axis of Fig. 5.4 we plot the displacement of the anisotropic initial conditions, measured by their k_3^i , with respect to the isotropic parent galaxy, placed at k_3^{iso} : as a consequence, initial conditions with larger $|k_3^i - k_3^{\text{iso}}|$ are characterized by larger amounts of radial orbital anisotropy. As already discussed in the Section 5.1, these initial conditions are placed in the (k_1, k_3) space along the lines given by equation (5.1). For example, in the upper panel of Fig. 5.5 the initial conditions A_1 , B_1 , and C_1 correspond to the isotropic parent galaxies placed at points A , B , and C (by assuming $\Upsilon_* = 5$ and determining L_B from equation 5.3), while in the lower panel the same parent galaxies and initial conditions are shown in the (k_1, k_2) space, connected by dotted lines.

On the vertical axis of Fig. 5.4 we plot the quantity $k_3 - k_3^{\text{iso}}$ corresponding to the end-product of each explored initial condition: if $k_3 = k_3^{\text{iso}}$ then the model has “fallen back” on the FP. We also recall here that $\delta k_3 \simeq 0.816 |k_3 - k_3^{\text{iso}}|$: in Fig. 5.4 the two horizontal dashed lines correspond to the FP thickness $\sigma(k_3)/0.816 \simeq 0.0613$, and so points inside this strip represent models consistent with the observed thickness of the FP. Finally, as an obvious consequence of the choice of the coordinate axes in Fig. 5.4, note that all the *initial conditions* (as for example models A_1 , B_1 , and C_1)

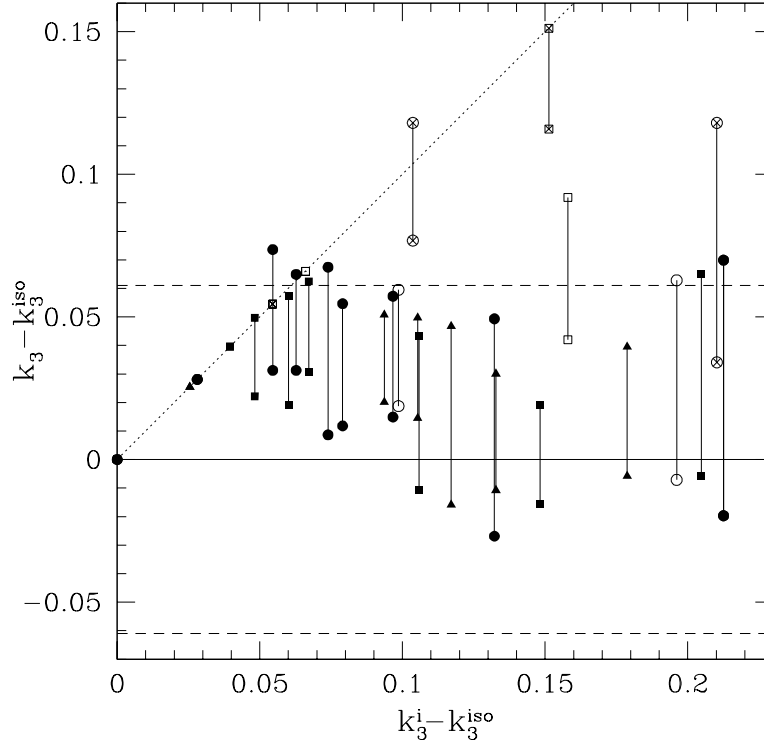


Figure 5.4: Final vs. initial k_3 for all galaxy models, measured with respect to k_3^{iso} , the k_3 coordinate of their isotropic parent galaxy. The horizontal dashed lines correspond to $\delta(k_3) = \sigma(k_3)$, while the dotted line $k_3 = k_3^i$ is the locus of the initial conditions and of the stable models. Symbols are the same as in Fig. 5.1. See the text for the explanation.

are located at $t = 0$ on the dotted line (with slope equal to 1). This means that this line is also the locus of *stable* models, while all the parent galaxies (as for example models *A*, *B*, and *C* of Fig. 5.5) lie at the point $(0, 0)$. A few stable anisotropic models may indeed be seen, as single solid points, on this line at low anisotropy values.

By increasing the amount of radial anisotropy the initial conditions move along the dotted line, and when they reach the critical value of the anisotropy radius they become unstable and rearrange their density profile and internal dynamics in a new, stable configuration. As we have seen, these end-products are strongly asymmetric, and so their representative points span a range of values as a function on the line-of-sight orientation. In Fig. 5.4 the vertical lines show the importance of this projection effect: note that, in general, the length of these segments is considerably smaller than the FP thickness.

The first result that can be obtained by inspection of Fig. 5.4 is the fact that, for one-component γ -models (solid symbols), radial orbit instability becomes effective for initial conditions *inside* the FP thickness, thus providing strong support to what found by CL97 for $R^{1/m}$ models. On the contrary, by considering as anisotropy limitation the very basic requirement of model consistency only, it is apparent from Fig. 5.4 that physically acceptable initial conditions could be placed at a distance

from the FP substantially larger than $\sigma(k_3)$, up to $\delta k_3 \simeq 2 - 3\sigma(k_3)$, the well known problem motivating this work. Models A_1 , B_1 , and C_1 in Fig. 5.5 are just three examples of such models. The second result is that all one-component, radially unstable models fall back on the FP: in other words, *not only the FP thickness is nicely related to stability, but the FP itself acts as an “attractor” for the end-products of radially unstable systems when their parent galaxies lie on it.*

The same results can be illustrated in a more direct way by using Fig. 5.5, where we plot the positions of the end-products of unstable models in the k space. As described above, to each final configuration derived from unstable initial conditions corresponds a set of points, depending on their relative orientation with respect to the observer’s line-of-sight. Due to the fact that the total luminosity of each model is obviously conserved by projection, these sets in the (k_1, k_3) space are actually *segments* of the straight line given by equation (5.1), as shown by Fig. 5.5 where the end-products of the initial conditions A_1 , B_1 , and C_1 can be immediately recognized. On the contrary, in the (k_1, k_2) plane the end-products are distributed, as a consequence of projection along different angles, on two-dimensional regions. This is due to the fact that no 1-1 relation similar to equation (5.1) exists between k_1 and k_2 , because also the value of $\langle R \rangle_e$ enters explicitly [$k_2 = \log(\Upsilon_* L_B^3 / K_V \langle R \rangle_e^6) / \sqrt{6} + \text{const}$]. For this reason for each end-product we plot several positions obtained with random viewing angles. Note however that the displacement in the (k_1, k_2) space occurs mainly along the k_2 coordinate, and this is due to the steepening of the profile (Fig. 5.2), i.e., to the increase of $\langle I \rangle_e$. *In any case, the models remain well inside the populated zone of the (k_1, k_2) plane.*

5.3.2 Two-component models

We now present the results of 8 numerical simulations of two-component (1,1) galaxy models. Although indications exist that the *onset* of radial orbital anisotropy is not strongly affected by the presence of a massive DM halo (see, e.g., Stiavelli & Sparke 1991, Ciotti 1996), in principle its *presence* could significantly modify the structural and dynamical properties of the end-products of unstable initial conditions, and so alter the findings obtained for one-component models described in Section 5.3.1.

Unfortunately, due to the dimension of the parameter space, we are not in the position to determine, as for one-component models, even a fiducial threshold for stability, and so we limit our study to the behavior of some representative models. In particular, we consider the following cases: $\mu = 1$ (“light” halo), $\mu = 3$ (“massive” halo), $\beta = 0.5$ (“concentrated” halo) and $\beta = 2$ (“diffuse” halo), where for each of the four possible combinations we fix the anisotropy radius to $s_a = 0.3$ and $s_a = 0.7$, two values corresponding to strongly unstable one-component $\gamma = 1$ models. In the simulations we use *live* DM halos, and in order to have equal mass particles for “stars” and “dark matter” we adopt $N_h = 98304$ and $N_* = 32768$ for $\mu = 3$, and $N_h = N_* = 65536$ for $\mu = 1$.

In analogy with the one-component case, the quantities T_r and T_t , entering the definition of $\xi = 2T_r/T_t$, are now the radial and the tangential component of the *total* (stellar and halo) kinetic energy tensor, respectively. This choice seems the natural one in the case of a live DM halo, when from a dynamical point of view the galaxy should be considered as a whole; but certainly other choices (for example, by

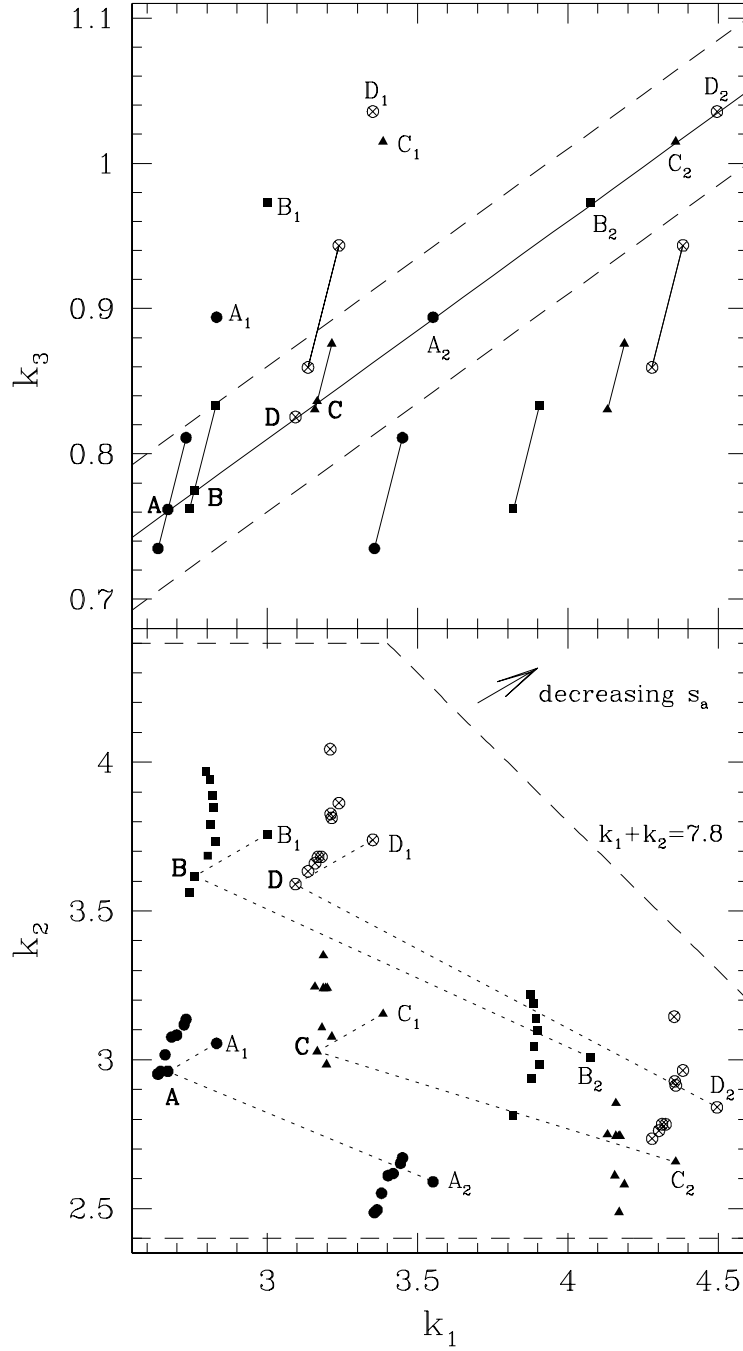


Figure 5.5: *Top*: k_3 vs. k_1 for a representative set of the one and two-component models shown in Fig. 5.4 and Fig. 5.6: symbols are the same. The solid line represents the FP relation (equation 2.5) with its observed dispersion (dashed lines). The stellar mass-to-light ratio is fixed to $\Upsilon_* = 5$ and $\Upsilon_* = 2.7$, for one and two-component models, respectively. *Bottom*: k_2 vs. k_1 for the same models plotted in the upper panel. The dashed lines define the region, as given by BBF92, where real galaxies are found. The arrow shows the direction followed by initial conditions with increasing radial anisotropy.

using in the ξ definition the kinetic energies of the stellar component only) could be equally well motivated. Clearly, the determination of the observational properties of the end-products is based on the analysis of their stellar component only.

As can be seen from Fig. 5.1, where the ellipticity of the stellar component of (1,1) models is represented by empty symbols, the basic trend of $(c/a)_{\text{fin}}$ with ξ is similar to that of one-component models: the end-products are mostly prolate systems, with axis ratio $(c/a)_{\text{fin}}$ in the same range of that of the one-component models. In general, however, when considering one and two-component initial conditions with the same ξ , the final *stellar* distribution remains more spherical in the cases with DM than in the one-component cases. Moreover, models with massive DM halos (empty symbols with crosses in Figs. 5.1, 5.2, 5.4 and 5.5) remain more spherical than the corresponding models with light halos and (approximately) the same ξ . This means that for the explored two-component models, at variance with the one-component cases, the parameter ξ *is not* well correlated with the final axis ratio. As can be seen from Fig. 5.2, the best fit parameter m of the projected stellar distribution of the end-products of (1,1) unstable models remains limited to values $m \lesssim 3$, the same range covered by one-component $\gamma = 1$ models. We also found that the final shape of the DM halos remains nearly spherical, with $0.88 \lesssim (c/a)_{\text{fin}} \lesssim 1$.

The observational properties of the end-products of the two-component models are illustrated in Figs. 5.4 and 5.5 where a comparison with the one-component models can be easily made. In particular, as in the one-component case, we found that the FP thickness still nicely separates stable from unstable models, independently of the amount and distribution of DM. However, the final position in the k space of the end-products depends on the amount of DM: as expected two-component models with a light halo (quite independently of its concentration) are very similar to one-component models, while models with massive DM halos are quite different. In particular from Fig. 5.4 it is apparent that massive halos prevent the models from falling back on the FP and this effect is stronger for more concentrated halos. This is shown in Fig. 5.5 (upper panel) by the final state of model D_1 , an initial condition obtained from the parent galaxy D , and characterized by a diffuse, massive DM halo. The positions of this end-product in the (k_1, k_2) plane are instead remarkably similar to those of the one-component models, and the same comments apply. Again, the scatter associated with projection effects is smaller than the total thickness of the FP.

5.4 Orbital anisotropy and the FP tilt

As discussed in Section 5.1, a question frequently addressed in the literature is whether the so-called FP tilt can be due to some kind of structural and/or dynamical “non-homology”, i.e., to a systematic variation from low to high luminosities of the structural and/or dynamical properties of the galaxies. From an observational point of view, this problem is still in general unsettled (see, e.g., Caon, Capaccioli & D’Onofrio 1993, Graham & Colless 1997, Gerhard et al. 2001, Bertin et al. 2002 and references therein) and so here we try to gain some hint on its solution by using the results of the numerical simulations described in Section 5.3. In particular we investigate whether relation (5.3) can be satisfied, in the whole observed luminosity

range ($0.2 \lesssim L_B \lesssim 40$ in the BBF92 sample), by a systematic variation of K_V induced by an appropriate underlying correlation $s_a = s_a(L_B)$, while maintaining fixed the models structure and Υ_* . In practice, the isotropic parent model of each family is placed on the FP by selecting its L_B and Υ_* ; then, by increasing its anisotropy and luminosity, the family of initial conditions is generated. Note that, at variance with the exploration described in Section 5.3, in this case all initial conditions are placed by construction on the FP, as can be seen from Fig. 5.5 (upper panel) where initial conditions A_2 , B_2 , C_2 and D_2 are generated by the parent galaxies A , B , C and D .

As in the case of Section 5.3, we found useful to represent the result of the simulations in a coordinate system slightly different from the usual k space. In the abscissae axis of Fig. 5.6 we plot the quantity $k_3^i - k_3^{\text{iso}}$ that measures how much a given initial condition is displaced on the FP from its parent isotropic model, while in the ordinate axis we plot the quantity $k_3 - k_3^i$ of the corresponding end-product. As a consequence all parent isotropic models are placed at the origin, and the FP is represented by the solid line $k_3 = k_3^i$: this line is also the line of stable initial conditions, while the two horizontal dashed lines represent the FP thickness. By using an argument similar to that used in the case of Fig. 5.4, we now obtain $\delta k_3 \simeq 0.816|k_3 - k_3^i|$ and the end-products of unstable initial conditions are vertical segments due to projection effects.

5.4.1 One-component models

For each family of γ -models we fixed a constant value of Υ_* such that the isotropic model, with a suitable assigned L_B , lies at the faint end of the FP ($k_1 \simeq 2.6$, $k_3 \simeq 0.75$). Then we placed the anisotropic initial conditions on the FP by choosing L_B , according to equation (5.3), as a function of $K_V = K_V(\gamma, s_a)$, in order to reproduce the tilt of the FP.

The inspection of Fig. 5.6 reveals that it is not possible to reproduce the FP tilt over the whole observed range ($\Delta k_1 \simeq 2$ and $\Delta k_3 \simeq 0.3$ in the BBF92 sample) by using stable model only. In fact, independently of the value of γ , the variations of K_V for $s_a \gtrsim s_{\text{as}}$ correspond to $\Delta k_3 \lesssim 0.04$, much smaller than the observed interval. If we consider also unstable (but consistent) systems, we can use a wider range of $K_V(\gamma, s_a)$ (see Table 5.1). In this case it is possible to reproduce the FP tilt over a much larger interval, $\Delta k_3 \simeq 0.2$, which is however still significantly smaller than the observed one: even if consistency limitations only are taken into account, *the FP tilt cannot be explained as an effect of a systematic increase of radial anisotropy in one-component models, under the assumption of structural homology* (see also Ciotti et al. 1996 and CL97).

What happens to the end-products of unstable initial conditions is shown in Fig. 5.6: in general they fall well outside the FP thickness, and the departure is larger for larger distance from the parent galaxy: they always fall out of $\sigma(k_3)$ for $k_3^i - k_3^{\text{iso}} \simeq 0.1$: this implies that, limiting to end-products of unstable initial conditions which remain *inside* the FP thickness, the maximum amount of the FP tilt that can be explained by pure anisotropy is $k_3^i - k_3^{\text{iso}} \lesssim 0.1$. Of course, a *larger* part of the FP tilt could be covered by considering parent galaxies with *tangentially anisotropic* velocity dispersion tensor (as observed in real, low luminosity ellipticals).

The results presented can also be seen, for a few representative cases, in the

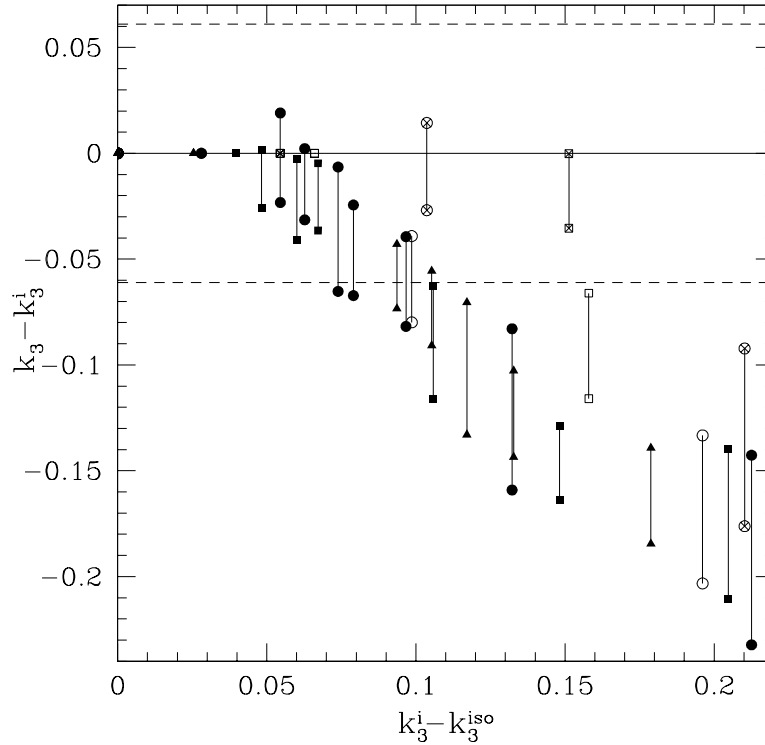


Figure 5.6: End-products of initial conditions placed on the FP at $k_3^i - k_3^{iso}$, where k_3^{iso} is the coordinate of their isotropic parent galaxy. The dashed lines correspond to $\delta k_3 = \sigma(k_3)$. Note that the abscissae range is significantly smaller than the actual range spanned by BBF92 galaxies, $\Delta k_3 \simeq 0.3$. Symbols are the same as in Fig. 5.4.

upper panel of Fig. 5.5, where the position of the end-products of models A_2 , B_2 , C_2 , D_2 is represented by the straight line segments. As in the case discussed in Section 5.3, the end-products remain well inside the region populated by real galaxies in the (k_1, k_2) plane.

Finally we qualitatively explore an interesting related problem (which however is not the argument of our paper), i.e., whether the FP tilt can be reproduced over the whole observed range in luminosity, for fixed Υ_* , in case the requirement of perfect structural homology is relaxed. In practice we determined Υ_* so that the parent isotropic $\gamma = 0$ model (to which corresponds the maximum value of K_V) is placed at the faint end of the FP ($L_B = 0.2$, $\Upsilon_* = 5$). With the same value of Υ_* the $\gamma = 1$ and $\gamma = 2$ parent galaxies are then placed on the FP, and their positions are characterized by larger L_B (and so k_1), due to the corresponding decrease of K_V (see first column in Table 5.1). In this approach, the FP tilt can be reproduced over almost all the observed range by using models compatible with *consistency*. However, even in this *mixed* structural and dynamical non-homology approach, if one limits to *stable* models only, the maximum available range is reduced to $\Delta k_3 \simeq 0.16$, approximately half of the required k_3 variation.

5.4.2 Two-component models

In analogy with the one-component case, for each family of (1,1) models, given μ , β (the same as for the models presented in Section 5.3.2) and Υ_* , we placed the parent isotropic model at the faint end of the FP and we derived L_B of the initial conditions according to equation (5.2), as a function of $K_V = K_V(\mu, \beta, s_a)$. As already discussed in Section 3.2, for each family of (1,1) models we study only two values of the anisotropy radius, $s_a = 0.3$ and $s_a = 0.7$. We found that for each family these initial conditions, under the only requirement of consistency ($s_a \geq s_{ac}$), span a range $\Delta k_3 \lesssim 0.2$, smaller than the observed one (see Fig. 5.6). The main difference with respect to the one-component case is that in the (k_1, k_3) space the end-products of the unstable (1,1) models move less than the one-component models with similar initial δk_3 and only the most anisotropic systems fall outside the FP thickness. An example of these systems is model D_2 , whose behavior in (k_1, k_3) and (k_1, k_2) planes, clearly represented in upper and lower panel of Fig. 5.5 respectively, is similar to that of one-component models (A_2 , B_2 , C_2). Again we found that the DM halo concentration is an important quantity, strictly related to the displacement of the end-product with respect to the initial conditions.

These findings suggest that *even in the two-component case under the assumption of perfect structural homology and constant mass-to-light ratio the FP tilt cannot be explained as a consequence of a systematic increase of radial orbital anisotropy.*

5.5 Discussion and conclusions

With the aid of numerical simulations of one and two-component galaxy models we explored the constraints imposed by the observed thickness and tilt of the FP on the amount and distribution of radial orbital anisotropy in elliptical galaxies. The main results are summarized below.

- Remarkably, all the explored models (both one and two-component, and quite independently of the density profile) are found to be unstable when their radial orbital anisotropy is high enough to place them outside the observed FP thickness (under the assumption that their isotropic parent models lie on the FP). On the contrary all stable models lie inside the FP thickness.
- The end-products of one-component unstable models initially placed outside the FP fall back inside the FP: in other words, the larger is the initial displacement from the FP, the stronger is the reassessment of the model structure and dynamics. The behavior of two-component models is more varied, due to the fact that the properties of their end-products are significantly affected by the amount of mass and the distribution of the DM halo. In particular, the end-products of models with massive (either concentrated or diffuse) DM halos remain outside the FP thickness, while models with light halos behave essentially like one-component models.
- Since the end-products of the unstable initial conditions are not spherically symmetric, their positions on the (k_1, k_3) plane depend on their relative

orientation with respect to the line-of-sight direction. However, the scatter due to projection effects is in general smaller than the observed thickness of the FP, for both one and two-component models.

- We found that it is impossible to reproduce the whole FP tilt with radially anisotropic but stable (one and two-component) models under the assumption of constant Υ_* and structural homology. In other words, under these assumptions, luminous galaxies would be radially unstable well before the bright end of the FP.
- At variance with what happens to the end-products of unstable models initially placed outside the FP thickness (but exactly for the same reasons), the end-products of unstable models with initial conditions on the FP, fall well outside the FP itself.

Our results lead to some speculation on the formation mechanism and evolutionary scenarios of elliptical galaxies. First, if the (unknown) formation mechanism produces galaxies with various degrees of internal radial orbital anisotropy, of which the isotropic ones constitute the “backbone” of the observed FP, then the most anisotropic systems would be radially unstable and would evolve into final states lying on the FP. Then no “ad hoc” fine tuning would be required on the amount of radial anisotropy of ellipticals at the moment of their formation. In addition, our results concerning the FP tilt could give some indications about the importance of dissipationless merging in the history of the assembly of elliptical galaxies. In fact, if Es form by hierarchical *dissipationless* merging, then the very existence of the FP necessarily implies structural or dynamical non-homology of the merging end-products. The possibility that we explored in this Chapter is that of a substantial dynamical non-homology as a function of galaxy luminosity. Our simulations show that this is not a viable possibility to reproduce the FP tilt: in this scenario the FP would be destroyed by merging. However, it should be clear that we cannot rule out the possibility that merging produces a combination of structural and dynamical effects that conspire to maintain galaxies on the FP. For this reason we have explored directly this problem, with the aid of one and two-component galaxy merging simulations, which are described in Chapter 6.

All our results on the FP thickness and tilt seem to point towards a significant dynamical homology in real galaxies, and dynamical homology in luminous Es has been recently determined by some authors (Gerhard et al. 2001); we note also that an independent observational support for dynamical homology is given by the very evidence of the $M_{\text{BH}}\text{--}\sigma_0$ relation (see Section 2.4), which relates a dynamical independent quantity (M_{BH}) with a quantity strongly dependent on anisotropy (σ_0). The fact that the scatter of the $M_{\text{BH}}\text{--}\sigma_0$ is very small means that elliptical galaxies are basically dynamically homologous systems.

6. Galaxy merging, the Fundamental Plane of elliptical galaxies, and the $M_{\text{BH}}\text{-}\sigma_0$ relation

In the present Chapter we consider the effects of galaxy merging on some of the most important scaling laws of Es. In particular, we present the results of N -body numerical simulations of dissipationless merging hierarchies.

6.1 Introduction

As already outlined in Chapter 1, a natural question to ask, in the context of galaxy formation studies, is how well *dissipationless* merging is able to produce and maintain the scaling relations of Es. We focus on dissipationless merging since it is simpler to be modeled with respect to gas rich merging, and because in this way we can check whether the contribution of gas dissipation is required in the merging scenario of Es formation. In addition, the analysis of dissipationless merging should indicate whether the merging between gas poor systems observed at $z < 1$ (van Dokkum et al. 1999) is a common phenomenon in Es lifetime, or a rare event. Existence of serious problems encountered by the picture of Es formation mainly driven by dissipationless merging to reproduce their scaling relations was pointed out, among others, by Ciotti & van Albada (2001; hereafter CvA01). In their *phenomenological approach*, just by combining the observed (edge-on) FP and the $M_{\text{BH}}\text{-}\sigma_0$ relations, they demonstrated that in a dissipationless merging scenario, and under reasonable assumptions for the addition of BH masses during the merging, *elliptical galaxies forced to lie on the FP and to satisfy the $M_{\text{BH}}\text{-}\sigma_0$ relation* would have effective radii exceedingly larger than those observed in real Es.

Here we follow a complementary approach, and the main goal is verifying, by using high resolution N -body numerical simulations of one and two-component galaxy models, whether the end-products of merging of galaxies, initially lying on the FP, lie on the FP (as well as on the other scaling relations) or they fail in some other respect (see also Pentericci, Ciotti & Renzini 1995; Capelato, de Carvalho & Carlberg 1995; Bekki 1998; Evstigneeva, Reshetnikov & Sotnikova 2002; Nipoti, Londrillo & Ciotti 2003b, hereafter NLC03b).

Numerical simulations are needed since, owing to possible structural and/or dynamical non-homology and to projection effects, one cannot predict with simple theoretical arguments how σ_0 and $\langle R \rangle_e$ evolve as consequence of merging: however, rough indications on their behavior can be derived from the study of the evolution of the *virial velocity dispersion* σ_V and the *virial radius* r_V ⁷. As a consequence of the virial theorem and the conservation of the total energy, in the merging of two galaxies with masses M_1 and M_2 and virial velocity dispersions $\sigma_{V,1}$ and $\sigma_{V,2}$, the virial velocity dispersion of the resulting galaxy (in case of no mass loss and negligible kinetic and interaction energies of the galaxy pair when compared to their internal energies) is given by

$$\sigma_{V,1+2}^2 = \frac{M_1 \sigma_{V,1}^2 + M_2 \sigma_{V,2}^2}{M_1 + M_2}. \quad (6.1)$$

It follows that $\sigma_{V,1+2} \leq \max(\sigma_{V,1}, \sigma_{V,2})$, i.e., *the virial velocity dispersion cannot increase in a merging process of the kind described above*. Under the same hypotheses, the virial radius $r_{V,1+2}$ of the resulting galaxy is given by

$$\frac{(M_1 + M_2)^2}{r_{V,1+2}} = \frac{M_1^2}{r_{V,1}} + \frac{M_2^2}{r_{V,2}}, \quad (6.2)$$

where $r_{V,1}$ and $r_{V,2}$ are the virial radii of the progenitors. Identity (6.2) implies that $r_{V,1+2} \geq \min(r_{V,1}, r_{V,2})$, i.e., *the virial radius cannot decrease in a merging process of the kind described above*.

From equations (6.1) and (6.2) it follows that, in the highly idealized scenario of a merging hierarchy based on identical, one-component seed galaxies characterized by $\sigma_{V,0}$, $r_{V,0}$ and M_0 , we expect $\sigma_V = \sigma_{V,0}$ and $r_V = (M/M_0)r_{V,0}$, independently of the merging sequence. Thus, by qualitatively assuming that $\sigma_0 \sim \sigma_V$ and $\langle R \rangle_e \sim r_V$, one should conclude that the FJ and Kormendy relations are not consistent with the scenario depicted above. Now, it is well known that for a large variety of mass models there is a good correlation between r_M (the half-mass radius of the galaxy, strictly related to $\langle R \rangle_e$) and r_V , with the proportionality constant showing little dependence on the particular density profile⁸ (see, e.g., Spitzer 1969, Ciotti 1991), and so, even in presence of structural non-homology in the merging end-products, the “prediction” of a linear growth of $\langle R \rangle_e$ with M should be quite robust. A more problematic situation (that can be properly addressed only with numerical simulations) arises when considering the relation between σ_V and σ_0 : at variance with r_M/r_V , structural non-homology can *strongly* affect the ratio σ_0/σ_V (see, e.g., Ciotti, Lanzoni & Renzini 1996; Bertin, Ciotti & Del Principe 2002). In addition, a systematic variation of orbital anisotropy with mass (the so-called dynamical non-homology) can produce an increasing σ_0 even at constant σ_V (although in Chapter 5 we showed that the whole tilt of the FP cannot be ascribed to orbital anisotropy effects only; see also Nipoti, Londrillo & Ciotti 2002, hereafter NLC02).

⁷By definition in a one-component galaxy $\sigma_V^2 \equiv 2T/M$ and $r_V \equiv -GM^2/U$, where T and U are the total kinetic and the gravitational energy of the galaxy, respectively.

⁸For example in truncated power-law spherical models $r_V/r_M = 2^{\frac{1}{3-\gamma}}(5-2\gamma)/(3-\gamma)$ and so $2 \leq r_V/r_M \lesssim 2.1$ for $0 \leq \gamma \leq 2$.

Here, with the aid of high-resolution N -body simulations of one and two-component galaxy models, we investigate the effect of subsequent generations of merging on the galaxy scaling relations. As outlined in Section 1.4, our study explores two extreme situations, namely the case of *major merging*, in which equal mass galaxies are involved at each step of the hierarchy, and the case of *accretion*, in which a massive galaxy increases its mass by incorporating smaller galaxies: the evolution of more realistic, “mixed” merging histories should be bracketed by our simulations.

6.2 Numerical simulations

As initial conditions for the first generation of merging we use spherically symmetric one and two-component Hernquist density distributions, corresponding to $\gamma = 1$ and $(1, 1)$ models, respectively (see Sections 3.1 and 3.2). At variance with the models used in Chapter 5, here we restrict to globally isotropic models: the distribution function (DF) is then given by equation (3.7) for both the stellar and the halo components. For the simulations described in this Chapter we used FVFPS, the new, fast and accurate, parallel N -body code described in Section 4.2.3.

For the stellar distribution of each seed galaxy of the one-component merging hierarchies we use $N_* = 16378$ particles, and in the two-component case the DM distribution made of $N_{\text{DM}} = 49152$ particles is added: with this choice, halo and stellar particles have the same mass (see Section 6.2.1). As a consequence of the merging hierarchy, the number of particles in the simulations increases with the galaxy mass: in the last merging of (one and two-component) equal mass systems and of the accretion scenario, the total number of particles involved is of the order of 5.2×10^5 and 3.2×10^5 , respectively.

We followed the dynamical evolution of each merging event up to the virialization of the resulting system, which is usually reached on a time scale shorter than $50T_{\text{dyn}}$ after the first encounter between the two galaxies: for example, the virialization time for the first step in the one-component equal mass merging hierarchy is of the order of 2 Gyr, assuming $M_* = 10^{10}M_{\odot}$ and $r_c = 1$ kpc. In the following we call “end-product” of a simulation the system made of bound particles after the virialization. In the determination of the intrinsic and the “observational” properties of the end-products, we followed the procedure described in Appendix A.2. In particular, we measured the end-product intrinsic axis ratios c/a and b/a (where a , b and c are the major, intermediate and minor axis of the associated inertia ellipsoid), their virial velocity dispersion σ_v and half-mass radius r_M , and, for several projection angles, the end-product circularized effective radius $\langle R \rangle_e$, central velocity dispersion σ_0 , and mean effective surface brightness $\langle I \rangle_e$ (obtained from the stellar mass profile by assuming a constant stellar mass-to-light ratio Υ_*). The central velocity dispersion σ_0 is obtained by averaging the projected velocity dispersion over the circularized surface brightness profile within a radius $\langle R \rangle_e/8$.

6.2.1 Initial conditions

Equal mass merging

The first generation of the *equal mass merging* hierarchy is obtained by merging a pair of identical, spherically symmetric and isotropic $\gamma = 1$ models (the “zeroth order” seed galaxies), while the successive generations are obtained by merging pairs of identical systems obtained by duplicating the end-product of the previous step. We followed the evolution of the hierarchy of 5 steps of *head-on* mergers (that would correspond, in absence of mass escape, to a mass increase of a factor 32); we also explored 3 steps of the *head-on* merging hierarchy whose seed galaxies are two-component (1, 1) models (in which we assume a DM halo more massive, $\mu = 3$, and less concentrated, $\beta = 2$, than the stellar component), and, finally, 3 steps of the hierarchy of encounters of one-component models with *non zero (orbital) angular momentum*.

In the assignment of the initial conditions for the head-on encounters the two galaxies are initially placed on an orbit characterized by vanishing relative energy and angular momentum, i.e., they would have a null relative velocity while at infinite relative distance. In practice, at the time $t = 0$, we place the two galaxies at a distance $d_{\text{rel}} \simeq 3\langle r \rangle_{90}$ (where $\langle r \rangle_{90}$ is the angle-averaged radius enclosing the 90% of the total mass M of each galaxy), and, neglecting the effects due to tidal forces, we assign to their centers of mass a relative velocity with modulus $v_{\text{rel}} = 2\sqrt{GM/d_{\text{rel}}}$. The end-products of each merging are non-spherical, and so, when exploring a successive merging, their mutual orientation at the beginning of the new simulation is randomly assigned. In the simulations with orbital angular momentum, we still consider vanishing relative energy and d_{rel} defined as above, and we assume as impact parameter the sum of the angle-averaged half-mass radii of the merging galaxies.

Accretion

In the case of the merging hierarchy in which the test galaxy grows by accretion of smaller systems (*accretion*), the seed galaxy is a one-component $\gamma = 1$ model, and the first merging event is identical to that in the equal mass merging case. In the second step, however, the first end-product (of mass $\sim 2M_*$) merges again with a seed galaxy, and so on. As a consequence, the mass ratio between the infalling stellar system and the test galaxy decreases approximately as $1/n$, where n is the step in the accretion hierarchy. Due to the higher computational cost required by accretion simulations with respect to equal mass merging in order to reach the same mass increase, in the former case we limit to 15 steps (of head-on merging) and to 9 steps (of merging with angular momentum), for a putative mass increase of a factor 16 and 10, respectively. As in the case of equal mass merging simulations, the relative initial positions and velocities of the infalling satellite and of the test galaxy are chosen so that at $t = 0$ they are on parabolic orbit, and the mutual orientation of the two galaxies is assigned randomly. In practice, as initial relative distance we adopt $d_{\text{rel}} \simeq \langle r \rangle_{90,1} + 2\langle r \rangle_{90,2}$, where the subscript 2 refers to the smaller galaxy. Again, in case of non zero angular momentum, the impact parameter is given by the sum of the angle-averaged half-mass radii.

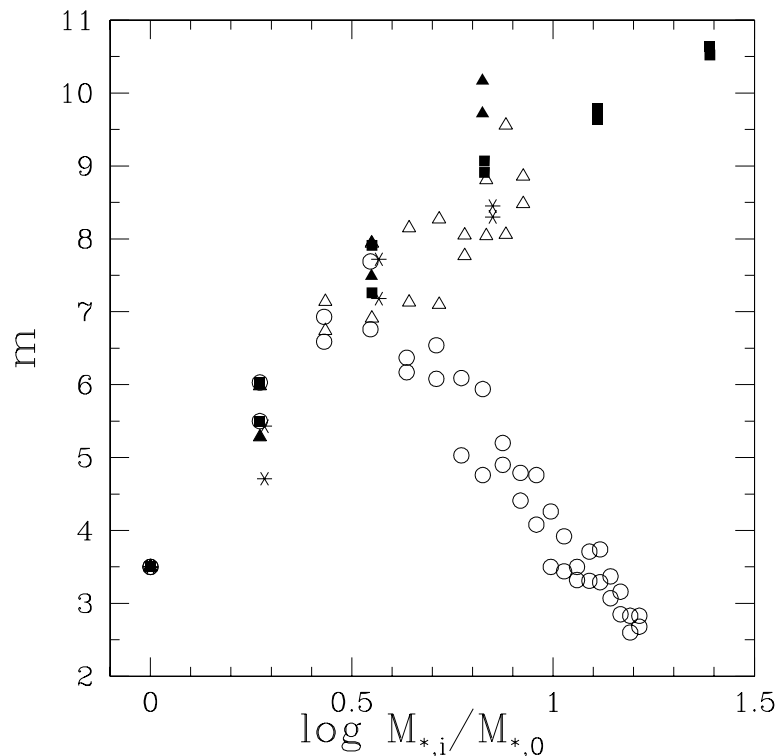


Figure 6.1: Sersic best-fit parameter m vs. total stellar mass of the end-products at stage i of the merging hierarchy. Equal mass mergers are shown as solid triangles and squares (one-component galaxies), and stars (two-component galaxies); empty triangles and circles represent the accretion hierarchies. Triangles correspond to simulations with non zero orbital angular momentum.

6.3 The results: equal mass merging

Before presenting the effects of equal mass merging on the FP and on the other scaling relations, we briefly describe the induced modifications of the internal structure and dynamics of one and two-component galaxy models. In general, the end-products are triaxial systems with axis ratios in the range $0.5 \lesssim c/a \lesssim 0.7$ and $0.7 \lesssim b/a \lesssim 0.8$ (where a , b and c are the major, intermediate and minor axis, respectively), in accordance with observed ellipticities of Es. For comparison with real galaxies, we also fitted (over the radial range $0.1 \lesssim R/\langle R \rangle_e \lesssim 10$) the projected stellar mass density profile of the end-products with the Sersic (1968) $R^{1/m}$ law as (equation 5.4; see also Appendix A.3), and in Fig. 6.1 we plot the best-fit parameter m as a function of the total mass of the systems, for one-component (solid squares and triangles) and two-component (stars) models. Clearly, the fitted quantities m and $\langle R \rangle_e$ depend on the relative orientation of the line-of-sight and of the end-products of the simulations: the two points for each value of the mass in Fig. 6.1 show the range of values spanned by m when projecting the final states along the shortest and longest axis of their inertia ellipsoids. We note that higher values of the best-fit parameter m correspond to more massive systems, a trend similar to that

observed in Es⁹ (see, e.g., Caon, Capaccioli & D’Onofrio 1993, Prugniel & Simien 1997, Bertin et al. 2002). Note also that the values of m are in the same range obtained from observations: we find $2 \lesssim m \lesssim 11$. However, from Fig. 6.1 one could argue that $m \approx 4$ galaxies should have experienced at most one major merger event in their life.

Following the discussion in Section 6.1, in Fig. 6.2 (top panel) we show the relation between the virial velocity dispersion and the total stellar mass of the mergers at each step of the merging hierarchy. In one-component models (solid squares and triangles) a modest increase of σ_V with M_* is apparent: for the last model in the hierarchy the mass is increased by a factor ~ 24.5 (instead of the maximum possible value of 32), while the σ_V is increased by a factor ~ 1.16 only. This small increase of σ_V with respect to the expectation of equation (6.1) (i.e., $\sigma_V = \text{const}$) can be explained with a simple generalization of the highly idealized situation formalized there. If during a merging between two galaxies with mass M_1 , M_2 and virial velocity dispersion $\sigma_{V,1}$, $\sigma_{V,2}$ a mass ΔM is lost with mean velocity v_{ej} , then the virial velocity dispersion of the end-product $\sigma_{V,1+2}$ is expected to be

$$\sigma_{V,1+2}^2 = \frac{M_1 \sigma_{V,1}^2 + M_2 \sigma_{V,2}^2 + \Delta M v_{\text{ej}}^2}{M_1 + M_2 - \Delta M} : \quad (6.3)$$

in particular σ_V increases as a consequence of the mass (and associated kinetic energy) loss. We found that in the simulations the mass lost during each merging never exceeds $\Delta M / (M_1 + M_2) \simeq 0.06$ and, consistently, the corresponding increase of σ_V is 2 – 5% (Fig. 6.2, top panel).

In Fig. 6.2 (bottom panel) we plot the half-mass radius as a function of the stellar mass of the mergers. As for σ_V , also for this quantity the simple virial expectation of a linear growth of r_V (and of r_M) with M (dotted line) is apparent. The “jump” from the initial condition position to the first merger is due to the significant change in the galaxy density structure (as revealed by the change of values of m in Fig. 6.1); the successive generations of merging are characterized by more similar density profiles, and, correspondingly, the points in Fig. 6.2 move parallel to the dotted line.

How does the presence of massive DM halos affect these results? As anticipated, in this case we investigated 3 steps of the (head-on) equal mass merging hierarchy by using two-component galaxy models. Due to its observational relevance, we focus here on the description of the properties of the stellar component only. As in the one-component case, the end-products are triaxial, and with the axis ratios in the same range. The best-fit Sersic parameter m still increases with mass (stars in Fig. 6.1). In the two-component simulations, owing to the presence of the DM halo, there are not arguments as simple as those used in equations (6.1), (6.2) and (6.3) in order to predict the effects of merging on σ_V (defined as $2T_*/M_*$) and r_M of the *stellar* component. However, it is apparent from Figs. 6.1 and 6.2 that the presence of a DM halo or angular momentum in the initial conditions does not modify the general trend of m , σ_V and r_M at increasing mass.

⁹Curiously, in Chapter 5 we found that in the case of end-products of unstable galaxy models m decreases for increasing radial orbital anisotropy in the initial conditions. Note also that in obtaining the best-fitting values plotted in Fig. 5.2 we used a radial range $0.1 \lesssim R/\langle R \rangle_e \lesssim 4$, the same range considered by NLC02 and Londrillo, Nipoti & Ciotti 2003.

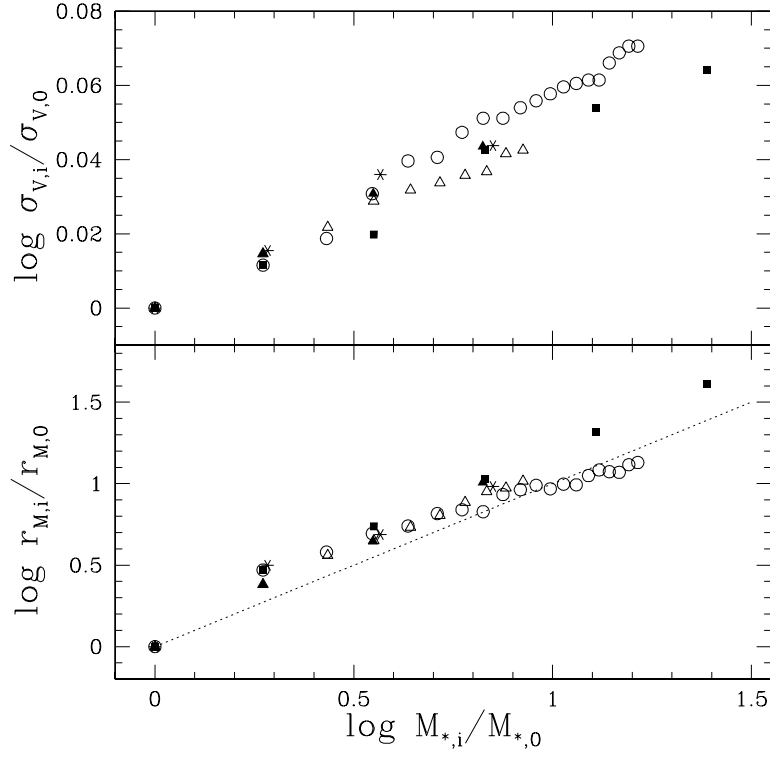


Figure 6.2: *Top panel:* virial velocity dispersion of the stellar component at stage i of the merging hierarchy vs. the total stellar mass of the merger. *Bottom panel:* angle-averaged half-mass radius r_{M} vs. total stellar mass. Symbols are the same as in Fig. 6.1. The dotted line indicates the relation $r_{\text{M}} \propto M$; $M_{*,0}$, $r_{\text{M},0}$ and $\sigma_{\text{V},0}$ are the stellar mass, the virial velocity dispersion and the half-mass radius of the seed galaxy. In the two-component cases, σ_{V} and r_{M} refer to the stellar component only. Note the different range spanned in the ordinate axes in the two panels.

6.3.1 Fundamental Plane

In Fig. 6.3 we plot the results of equal mass merging simulations in the principal planes (k_1, k_3) and (k_1, k_2) , where one-component galaxy models resulting from head-on mergers and from merging with angular momentum are identified by solid squares and triangles, respectively; two-component models are represented by stars. The progenitor of the merging hierarchy (the point without bar) is placed on the edge-on FP by choosing its luminosity $L_{\text{B}} = 3 \times 10^9 L_{\text{B}\odot}$ and *stellar* mass-to-light ratio $\Upsilon_* = 5$, so that equation (2.5), represented by the solid line, is satisfied. Consistently with the adopted dissipationless scenario, the value of Υ_* is kept constant during the whole merging hierarchy. Due to the loss of spherical symmetry of the end-products of the merging simulations, their coordinates depend on the line-of-sight direction; however, being the luminosity (mass) of each end-product fixed, variations of k_1 , k_2 , k_3 due to projection effects are not independent. The k_1 and k_3 coordinate of a galaxy of given luminosity are linearly dependent, as given by equation (5.1); this dependence is reflected by the straight lines in Fig. 6.3

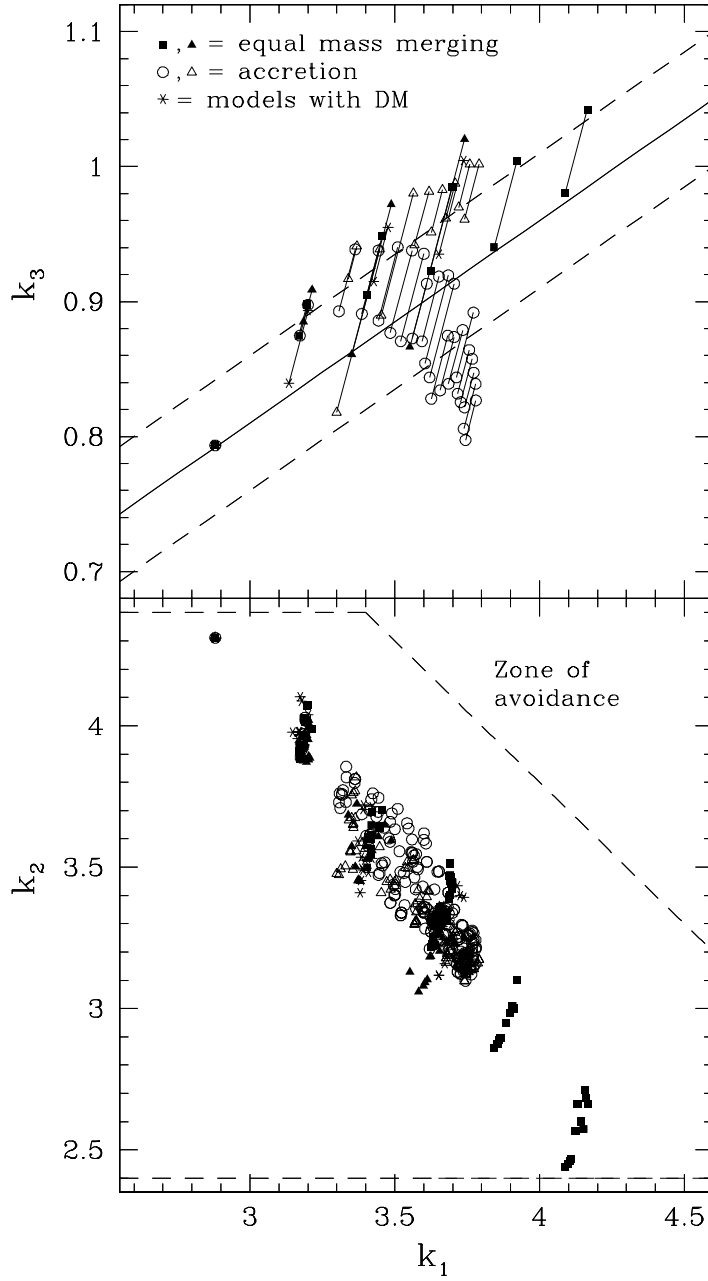


Figure 6.3: *Top panel:* the merging end-products in the (k_1, k_3) plane, where the solid line represents the FP relation as given by equation (2.5) with its observed $1-\sigma$ dispersion (dashed lines). Bars show the amount of projection effects. *Bottom panel:* the merging end-products in the (k_1, k_2) plane, where the dashed lines define the region populated by real galaxies as given by BBF92. Each model is represented by a set of points corresponding to several random projections. Symbols are the same as in Fig. 6.1.

(top panel), each of them representing the range spanned in the (k_1, k_3) space by a given end-product when observed over the solid angle. As done in Chapter 5, in order to quantify the deviation of a model from the FP, we use the vertical distance $\delta k_3 \equiv |k_3 - 0.15k_1 - 0.36|$ from the point to the FP itself. It is interesting to note that for all the end-products the projection effects translate into a δk_3 of the same order of magnitude of the observed FP dispersion. In addition it is also apparent from Fig. 6.3 how k_3 and k_1 increase with the galaxy mass consistently with the observed FP tilt and thickness. Being Υ_* fixed in our simulations, from Fig. 6.1 we conclude that one-component equal mass dissipationless merging is able to reproduce (basically by structural non-homology) the edge-on FP of elliptical galaxies (see also Capelato et al. 1995).

We also explored the behavior of the models in the (k_1, k_2) plane (Fig. 6.3, bottom panel), which represents the face-on view of the FP; the region populated by real galaxies in this plane is identified by dashed lines. By fixing the scale length, we place the first progenitor (with $\langle R \rangle_e \simeq 0.7$ kpc) in a zone of the (k_1, k_2) plane populated by low-luminosity ellipticals ($k_1 \simeq 3$, $k_2 \simeq 4.5$), and for each end-product we plot the (k_1, k_3) positions for a few random projection angles. Note that, at variance with the coordinates (k_1, k_3) , k_1 and k_2 are related (for a given end-product) by an expression containing $\langle R \rangle_e$ besides L_B , and for this reason in the (k_1, k_2) plane the effect of projection is to distribute the end-products on two-dimensional regions. One-component equal mass mergers (solid squares and triangles) are moved by merging towards the bottom right of the (k_1, k_2) plane, roughly parallel to the line defining the *zone of avoidance*, in accordance with the prediction of BBF92. The produced displacements are very large: it is remarkable that the end-products of the last step of the hierarchy are found in a position only marginally consistent with the populated region in the (k_1, k_2) space. It is also interesting to note that the presence of substantial angular momentum in the initial conditions does not change significantly the properties of equal mass mergers, both in the (k_1, k_3) and in the (k_1, k_2) plane.

The results of equal mass merging of two-component galaxies are represented in Fig. 6.3 with stars. Due to the presence of DM, in order to place the first progenitor ($L_B = 3 \times 10^9 L_{B\odot}$) on the FP, we assumed a stellar mass-to-light ratio $\Upsilon_* = 2.3$. It is apparent that both in the (k_1, k_3) and (k_1, k_2) planes, the behavior of two-component models does not significantly differ from the corresponding one-component models. In other words, *dissipationless, equal mass merging of one and two-component models seems to be consistent with the existence of the FP of Es.*

6.3.2 Faber–Jackson and Kormendy relations

As we have shown in the Section above, dissipationless merging of one and two-component galaxy models is surprisingly consistent with the existence of the FP, especially considering its small thickness when seen edge-on. However, Es do follow additional scaling relations, such as the FJ and Kormendy relations, and so here we compare the results of our simulations with these scaling laws.

The solid line in the upper panel of Fig. 6.4 represents the FJ relation in the form $L_B \propto \sigma_0^4$ together with its scatter ($\delta \log \sigma_0 \simeq 0.1$, Davies et al. 1983, dashed lines); the dotted line represents the steeper fit ($L_B \propto \sigma_0^{3.5}$) derived by Dressler et

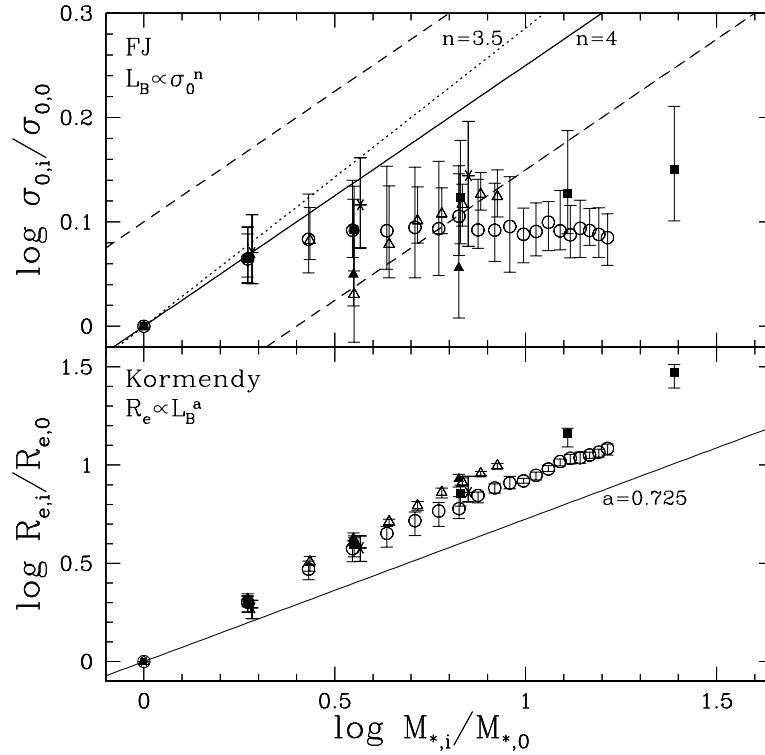


Figure 6.4: *Top panel:* stellar central velocity dispersion (normalized to that of the first progenitor) vs. total stellar mass. Points correspond to angle-averaged values, bars indicate the range spanned by projection effects. The solid and the two dashed lines represent the Faber-Jackson relation $L_B \propto \sigma_0^4$ and its scatter, while the dotted line represents $L_B \propto \sigma_0^{3.5}$. *Bottom panel:* stellar effective radius (normalized to that of the first progenitor) vs. total stellar mass. Points and bars have the same meaning as in top panel. The solid line represents our “fiducial” Kormendy relation, obtained combining the FP and the FJ with $n = 4$ (see text); symbols are the same as in Fig. 6.1. Note the different range spanned in the ordinate axes in the two panels.

al. (1987). The end-products of (head-on) equal mass merging of one-component galaxies (solid squares) have a σ_0 lower than that predicted by the FJ relation for the given mass increase, and the discrepancy is stronger in case of merging with angular momentum (solid triangles). It is interesting to compare this plot with the upper panel of Fig. 6.2: it is then clear how the failure of FJ can be directly traced to the constancy of σ_V and to the significant dynamical homology of the mergers. This latter point again suggest that *structural* non-homology, more than dynamical non-homology is at the origin of the FP in the explored merging scenario (see also Section 5.4 and NLC02). Models with DM (stars in Fig. 6.4) seem to follow more closely the FJ relation, even though the representative points show the same clear trend as the one-component merging hierarchy: it seems clear to us that additional simulations would bring also two-component models completely outside the FJ relation.

Considering now the agreement with the FP on one side, and the failure to reproduce the FJ relation on the other side, we would expect that also the Kormendy

relation is not reproduced by the equal mass merging hierarchy. In fact, if we assume that the Es obey to the FJ relation, $L_{\text{B}} \propto \sigma^n$, then from equation (2.5) we obtain a fiducial Kormendy relation $\langle R \rangle_{\text{e}} \propto L_{\text{B}}^{1.225-2/n}$. For example, with $n = 4$ (for which the “corresponding” Kormendy exponent is remarkably near to that reported by Bernardi et al. 2003) the effective radius of the end-product of the last equal mass merger is a factor ~ 3 larger than that predicted by the “Kormendy” relation. In other words, the results of our simulations are characterized by too large effective radii (see Fig. 6.4, bottom panel). Thus, in the explored equal mass merging hierarchies both σ_0 and $\langle R \rangle_{\text{e}}$ deviate systematically from the values expected from FJ and Kormendy relations. Yet, their deviations from the two scaling laws curiously compensate reproducing the edge-on FP; this shows clearly that the FJ and Kormendy relations are not simple projections of the FP, which is actually preserved by merging, but, despite their larger scatter, contain additional information on galaxy structure and dynamics.

6.4 The results: accretion

In Section 6.3 we showed that, in the case of equal mass merging of one and two-component galaxies, the virial expectations were qualitatively followed also by the observational properties $\langle R \rangle_{\text{e}}$ and σ_0 , in addition to σ_{V} and r_{V} . We recall that these expectations are independent of the specific merging history, as far as the zeroth order seed galaxies are identical systems, and so we could consider “accretion” simulations superfluous. However, the amount of escaping particles or the non-homology of the final end-products could depend on the mass ratio of the merging systems, thus resulting in substantial changes in σ_{V} and/or σ_0 . Following this argument we now present the results of accretion simulations, whose technical setting is described in Section 6.2.1. From the structural point of view, the end-products of accretion are less flattened than the corresponding (i.e. with the same mass) equal mass mergers, being, in general, triaxial systems with axis ratios in the range $0.6 \lesssim c/a \lesssim 0.9$, and $0.7 \lesssim b/a \lesssim 0.9$, and becoming more and more spherical with increasing mass as a consequence of the higher number of merging events and the random direction of accretion. The evolution of the surface brightness profile in the accretion hierarchy is shown in Fig. 6.1, where the best-fit Sersic parameter m is represented with empty circles and triangles (for head-on merging and merging with angular momentum, respectively). *A first relevant difference with the equal mass merging results is the decrease of m with mass at mass ratios larger than 4 for the head-on accretions*, and the consequent smaller range of m ($2 \lesssim m \lesssim 8$) spanned by their end-products. Therefore, the explored head-on accretion scenario fails to reproduce the relation between the surface brightness profile shapes and luminosity of real galaxies, which are characterized by m increasing with galaxy luminosity and also spanning a larger range (see Section 6.3). A different situation is obtained when considering accretion simulations with non negligible orbital angular momentum: the structural properties of the end-products are curiously similar to the equal mass cases.

In the upper panel of Fig. 6.2 we plot σ_{V} as a function of mass of also of the head-on accretion end-products (empty circles). We found that the fraction of

mass lost in each merging, $\Delta M/(M_1 + M_2)$, decreases from ~ 0.06 in the first step to ~ 0.01 in the last one, summing up to a total amount of mass lost over 15 steps of $\sim 18\%$, about the same value found in the corresponding equal mass merging cases. The slightly larger increase of σ_v in the head-on accretion hierarchy with respect to the equal mass merging cases is fully accounted for larger values of v_{ej} , in accordance with the estimate given in equation (6.3). In the lower panel of Fig. 6.2 we also show the evolution of r_M in the head-on accretion hierarchy (empty circles). The behavior of this quantity is qualitatively similar to that of equal mass mergers: the slightly flatter slope of the sequence with respect to the simple expectation $r_M \propto M$ is due to the stronger evolution of structural non-homology, as revealed by Fig. 6.1. On the other hand, the end-products of accretion simulations with angular momentum (empty triangles in Fig. 6.2) are more similar to equal mass merging case.

6.4.1 Fundamental Plane

The most striking difference of the end-products of head-on accretion simulations (empty circles) with respect to the equal mass merging hierarchy and also with respect to accretion simulations with angular momentum (empty triangles) is apparent in the upper panel of Fig. 6.3, where the results are plotted in the (k_1, k_3) space. After few accretions, the end-products are characterized by a k_3 *decreasing* for increasing k_1 , at variance with the FP slope and the trend shown by the end-products of equal mass mergers. As a consequence, the last explored models (corresponding to an effective mass increase of a factor ~ 12) are found at a distance δk_3 larger than the FP scatter. This result, when interpreted by using the information in Fig. 6.1, is not surprising. In fact, being the coordinate k_3 a measure of non-homology for galaxies with constant Υ_* (as those explored in this paper), the decrease of the Sersic parameter m at increasing mass (at variance with real galaxies) reflects directly in the unrealistic trend in the (k_1, k_3) plane. On the contrary, in the face-on (k_1, k_2) plane (Fig. 6.3, lower panel), the end-products of accretion (both head-on and with angular momentum) evolve along the same direction followed by equal mass mergers, albeit with a smaller excursion in k_1 and k_2 .

6.4.2 Faber–Jackson and Kormendy relations

In Fig. 6.4 we also plot the results of accretion simulations in the planes representing the FJ and the Kormendy relations. At variance with the case of the edge-on FP, and *independently on the presence of angular momentum*, the behavior of the end-products is considerably similar to that of the equal mass merging, i.e., both the FJ and the Kormendy relations are *not* reproduced. The end-products have σ_0 smaller and $\langle R \rangle_e$ larger than the values predicted by the two scaling relations for the given luminosity (mass) increase. However, a closer inspection of Fig. 6.4 reveals that both σ_0 and $\langle R \rangle_e$ are systematically larger in the case equal mass mergers than in the case of head-on accretion: in other words, the end-products in the latter case deviate *more* from the FJ and *less* from the Kormendy than those in the former. The result relative to the effective radius simply reflects the different evolution of the half-mass radius in the two scenarios (see Fig. 6.2, lower panel), while the behavior of σ_0 depends both on structural and dynamical non-homology effects: the combined

effect of the lower values of σ_0 and the larger values of $\langle R \rangle_e$ is responsible of the decreasing of k_3 with k_1 observed in the analysis of the edge-on FP. In other words, at variance with equal mass mergers and accretions with angular momentum, in case of head-on accretion there is not enough compensation between the trends in σ_0 and $\langle R \rangle_e$ able to reproduce the FP tilt.

6.5 Dissipationless merging and the $M_{\text{BH}}\text{-}\sigma_0$ relation

On the basis of the results of the previous Section, it is particularly interesting to investigate whether dissipationless merging is able to reproduce the $M_{\text{BH}}\text{-}\sigma_0$ relation, and we attempt to answer this question by using the simulations presented in Section 6.2. Here we recall that in our simulations we do not take into account the presence of BHs in the merging galaxies, yet we argue that we can reach robust conclusions, and this for two reasons. As well known, at the equilibrium (i.e. after the virialization of the end-product) the presence of the BH has not significant influence on σ_0 . This can easily be seen by considering that the sphere of influence of a BH with mass M_{BH} at the center of a galaxy with central velocity dispersion σ_0 has a fiducial radius $r_{\text{BH}} \equiv GM_{\text{BH}}/\sigma_0^2$, and combining this equation with the $M_{\text{BH}}\text{-}\sigma_0$ relation (equation 2.11) we obtain

$$r_{\text{BH}} \simeq 0.01 \times \left(\frac{\sigma_0}{200 \text{ km s}^{-1}} \right)^{\alpha-2} \text{ kpc}, \quad (6.4)$$

where we assumed $M_{\text{BH}} = 10^8 M_\odot$ when $\sigma_0 = 200 \text{ km s}^{-1}$ (see, e.g., Tremaine et al. 2002). The central velocity dispersion used in the definition of the FP and of the $M_{\text{BH}}\text{-}\sigma_0$ relations is the luminosity weighted projected velocity dispersion inside the radius $\langle R \rangle_e/8$ which, for ellipticals with $\sigma_0 \simeq 200 \text{ km s}^{-1}$, is in the range $0.2 \lesssim \langle R \rangle_e/8 \lesssim 0.6 \text{ kpc}$, one order of magnitude larger than r_{BH} . Thus, once the numerical end-products reached the equilibrium, their σ_0 is a good estimate of the real quantity even in presence of a BH of realistic mass. The second reason requires a more careful discussion. In fact, during the dynamical evolution of the merging system, a BH binary is formed and, in principle, its evolution could affect the kinematic properties of the end-product even beyond r_{BH} . However Milosavljevic & Merritt (2001), with the aid of numerical simulations, showed that the formation of a BH binary does not modify significantly the central velocity dispersion measured within the standard aperture $\langle R \rangle_e/8$, although the inner density profile *is* modified (for interesting observational evidences of this case see Lauer et al. 2002). In any case, we remark here that, if any, the expected effect of binary BHs is to *decrease* the central velocity dispersion, as a consequence of dynamical friction heating against background stars.

On the basis of these considerations we simply assume that each seed galaxy contains a BH of mass $M_{\text{BH},0}$, and that each merging end-product contains a BH obtained by the merging of the BHs of the progenitors (at the end of this Section, however, we will discuss two important problem faced by this last assumption). Unfortunately, BH merging is still a poorly understood physical process, in particular with respect to the amount of emitted gravitational waves (see, e.g., CvA01, and references therein), and for this reason we consider two extreme situations: the case

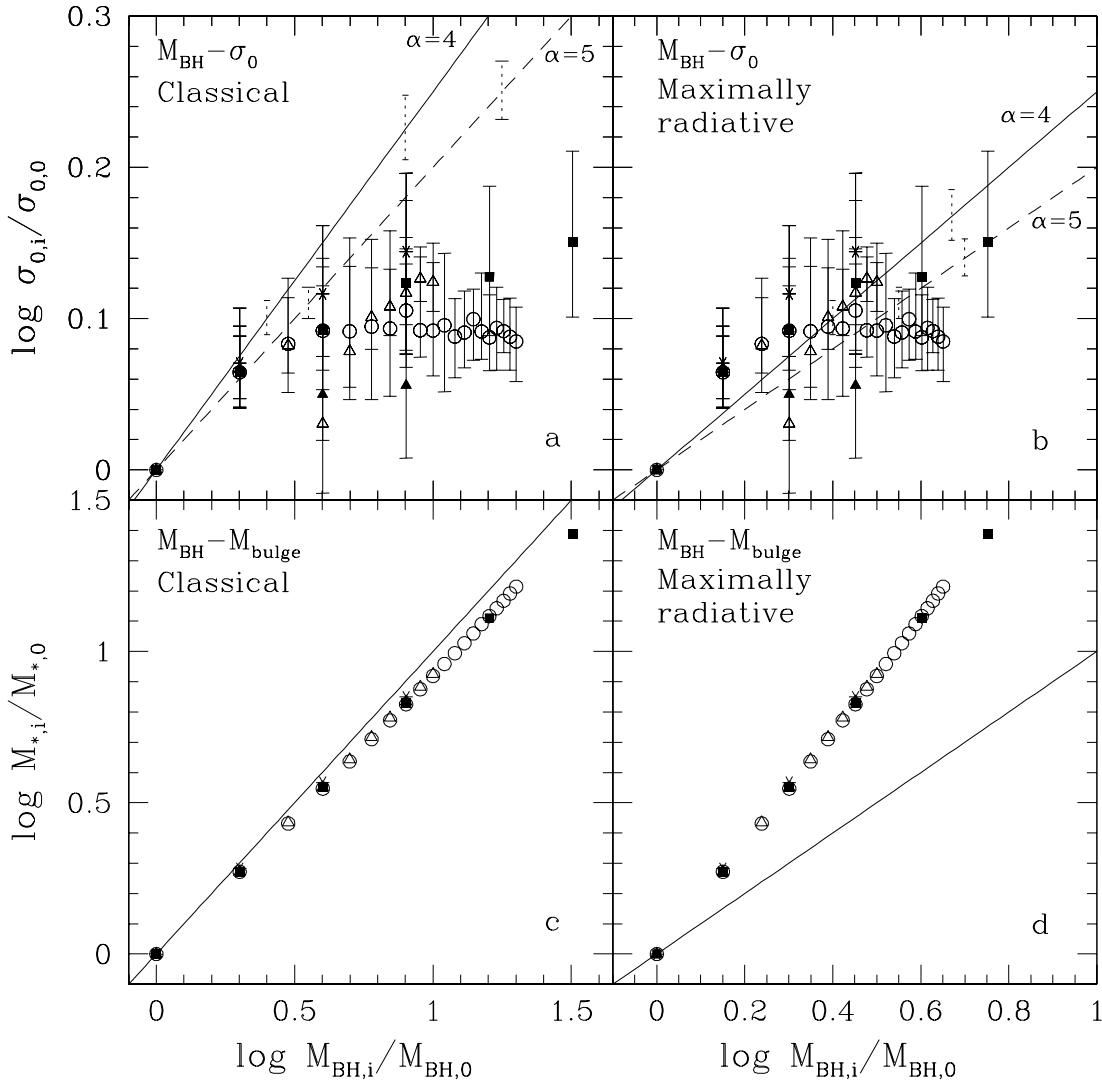


Figure 6.5: *Panel a*: galactic central velocity dispersion vs. BH mass for classical BH merging; $\sigma_{0,0}$ and $M_{\text{BH},0}$ are the central velocity dispersion and BH mass of the first progenitor, respectively. The points correspond to the mean value over the solid angle, while the bars indicate the range spanned by projection effects. Solid and dashed lines represent the $M_{\text{BH}}-\sigma_0$ relation for $\alpha = 4$ and $\alpha = 5$, respectively, while vertical dotted lines show the observed scatter around these best fits. *Panel b*: same data as in panel a, but for maximally radiative BH merging. *Panel c*: stellar mass vs. BH mass for classical BH merging; $M_{*,0}$ is the stellar mass of the first progenitor and the solid line represents the Magorrian ($M_{\text{BH}} \propto M_{\text{bulge}}$) relation. *Panel d*: same data as panel c, but for maximally radiative BH merging. Symbols are the same as in Fig. 6.1.

of *classical* combination of masses ($M_{\text{BH},1+2} = M_{\text{BH},1} + M_{\text{BH},2}$, with no emission as gravitational waves), and the case of *maximally efficient radiative merging* ($M_{\text{BH},1+2}^2 = M_{\text{BH},1}^2 + M_{\text{BH},2}^2$, corresponding to entropy conservation in a merging of two non rotating BHs). Following this choice, in Fig. 6.5 we plot the central velocity dispersion of the mergers versus the mass of their central BH in the case of classical (panel a) and maximally radiative (panel b) BH merging. As expected from the similarity between the FJ and the $M_{\text{BH}}\text{-}\sigma_0$ relations, in the classical case, both (one-component) equal mass mergers (solid squares and triangles) and accretion mergers (empty circles and triangles) are unable to reproduce the observed relation, even when its slope is assumed as high as 5, with representative points well outside the observed scatter (vertical dotted bars). As it happens for the FJ relation, the situation is somewhat better when considering equal mass mergers of two-component galaxy models: in presence of DM the stellar central velocity dispersion is higher for given BH mass and the end-products are found closer to the observed relation (stars in Fig. 6.5). Thus, as for the FJ, the reason of the failure of dissipationless merging to reproduce the $M_{\text{BH}}\text{-}\sigma_0$ relation is that the end-products are characterized by a too low σ_0 for the given M_{BH} , i.e., M_{BH} is too high for the resulting σ_0 . A promising solution to this problem could be the emission of some fraction of M_{BH} as gravitational waves. In fact, by assuming maximally efficient radiative BH merging, the points are found remarkably closer to the observed relation, even if it is apparent that the slope of the $M_{\text{BH}}\text{-}\sigma_0$ relation is not well reproduced by the end-products of head-on accretion (empty circles). Note however that, while in the classical scenario the Magorrian relation is (obviously) nicely reproduced (Fig. 6.5, panel c), in case of substantial emission of gravitational waves the relation between BH mass and bulge mass is *not* reproduced (Fig. 6.5, panel d).

All the results presented in this Section holds under the strong assumption that the BHs of the merging galaxies are retained by the end-products, but there at least two basic mechanisms that could be effective in expelling the central BHs. The first is related to the general instability of three body systems: if a third galaxy is accreted by the end-product of a previous merging before the binary BH at its center merged in a single BH, then the escape of the smallest BH is highly possible. It is clear that if this process happens more than a few times, then the Magorrian relation will be not preserved at the end. A plausible solution to this problem is then to assume that the characteristic time of BH merging (first by dynamical friction on the background stars and then by emission of gravitational waves) is shorter than the characteristic time between two galaxy merging (for a detailed discussion of this problem see, e.g., Milosavljevic & Merritt 2001, Yu 2002, Haehnelt & Kauffmann 2002, Volonteri, Haardt & Madau 2003). However, a second physical mechanism could be more effective in expelling the resulting BH from the center of a galaxy merger, i.e., anisotropic emission of gravitational waves. This process, commonly known as the “kick velocity”, is directly related to the fraction of BH mass emitted anisotropically during the BH coalescence (see, e.g., Flanagan & Hughes 1998, CvA01). Indeed, gravitational waves travel at the velocity of light, and so even the anisotropic emission of *a few thousandths* of the mass of the BH binary will produce a recoil (due to linear momentum conservation) of the resulting

BH with a characteristic velocity higher than the escape velocity typical of massive galaxies. In conclusion, it seems to us not trivial to assume that in each galaxy merging the resulting BH will reside at the center (see, e.g., Haehnelt & Kauffmann 2000).

6.6 Discussion and conclusions

As outlined in Section 6.1, the study presented in this Chapter is similar, in some aspects, to previous studies concerning the effects of merging on the FP. The results of our simulations are consistent with those of Capelato et al. (1995), based on N -body simulations of King (1966) galaxy models, and of Dantas et al. (2003), based on $\gamma = 1$ models, who found that the edge-on FP is reproduced by dissipationless merging, owing to non-homology of the end-products. However, they considered only the first two or three steps of the merging hierarchy. In the same line of investigation, Gonzalez-Garcia & van Albada (2003) found that also the first generation of end-products of dissipationless merging based on $\gamma = 2$ models preserves the FP when seen edge-on. At variance with these works, we used galaxy models with a substantially larger number of particles, we explored the cumulative effects of several generations of merging, and we also compared with other scaling laws, such as the Faber-Jackson, the Kormendy, the $M_{\text{BH}}\text{-}\sigma_0$ and the Magorrian relations.

The main results of our simulations can be summarized as follows:

- The edge-on FP is well reproduced by dissipationless hierarchical equal mass merging of one and two-component galaxy models, and by accretion simulations with substantial angular momentum, with their seed galaxies (i.e. the merging zeroth order generation) placed on the FP itself. On the contrary, in the case of head-on accretion, the k_3 coordinate *decreases* at increasing k_1 , at variance with real galaxies. The physical reason of these different behavior is due to a different evolution of structural non-homology of the end-products in the two scenarios: the Sersic best-fit parameter m grows monotonically with mass in equal mass mergers (and accretion with angular momentum), while *decreases* with mass in head-on accretion end-products.
- In both scenarios the scatter in the (k_1, k_3) coordinates associated to projection effects is of the order of the observed $1\text{-}\sigma$ dispersion of the edge-on FP.
- At variance with the results of the edge-on FP, all the results of our simulations are in qualitative agreement when plotted in the (k_1, k_2) plane, where the FP is seen nearly face-on. In this plane the mergers move parallel to the line defining the zone of avoidance, and remain near the region of the FP populated by real galaxies.
- As a direct consequence of the numerical findings that the “observables” σ_0 and $\langle R \rangle_e$ follow closely the evolution of σ_V and r_V as predicted by the virial theorem, the end-products of our simulations fail to reproduce both the FJ and Kormendy relations. However, in the case of equal mass merging and accretion merging with angular momentum, the large values of $\langle R \rangle_e$ and the

nearly constant values of σ_0 curiously compensate, and the end-products follow nicely the edge-on FP (see the first point above).

- Under the reasonable hypothesis that the derived values of σ_0 are not strongly affected by the dynamical evolution of binary BHs, our results show that dissipationless merging, while in accordance with the Magorrian relation, fails to reproduce the $M_{\text{BH}}\text{-}\sigma_0$ relation. We have then shown that, allowing for substantial emission of gravitational waves during the BHs coalescence, the $M_{\text{BH}}\text{-}\sigma_0$ relation is surprisingly reproduced, but the Magorrian relation is not. Merging by head-on accretion suffers of an additional problem when considered together with the Magorrian relation: our simulations in fact showed that the best Sersic m parameter decreases at increasing mass of the end-product, a behavior opposite to what is empirically found (Graham et al. 2001).

In conclusion the results of the presented simulations suggest that *substantial* dissipationless merging (especially when involving stellar systems of very different mass) cannot be the basic mechanism of formation of Es. We note, however, that our exploration of the parameter space is by no means complete, because in the simulations were limited to the case of parabolic orbits and we did not consider initial conditions corresponding to *multiple* merging. In any case, indications exist that our results should be obtained also under these more general circumstances (see, e.g., Gonzalez-Garcia & van Albada 2003, Nipoti et al. 2003c, and the results presented in the following Chapter). Finally, we note that from the numerical results one cannot exclude, on the basis of FP, FJ, and Kormendy relations, that Es could experience *few* occasional mergers with other Es, even in recent times as observed by van Dokkum et al. (1999). In any case, it is well known that many other astrophysical evidences, based on stellar population properties, such as the $\text{Mg}_2\text{-}\sigma_0$ (see, e.g., Burstein et al. 1988, Bender, Burstein & Faber 1993) and the color-magnitude (Bower, Lucey & Ellis 1992) relations, and the waveband dependence of the relation between mass-to-light ratio and galaxy luminosity (see, e.g., Pahre, Djorgovski & de Carvalho 1998, Pahre, de Carvalho & Djorgovski 1998), strongly argue for a substantial dissipative phase in the formation of spheroids.

If we exclude dissipationless merging as the formation mechanism for Es, then we are left with two possible solutions, namely the monolithic scenario or a merging scenario where dissipation plays an important role. In this last case the presented simulations can also say something. In fact gas dissipation should be effective in shrinking the density distribution of the merging end-products, and, at the same time, increasing their central velocity dispersion, changes that are in the direction required by the FJ and Kormendy relations. In addition, in order to preserve the Magorrian relation, a fraction of the star forming dissipating gas must flow on the central BH, producing QSO activity; in this case the cosmological evolution of QSOs would be a tracer of the merging history, in accordance with the old ages of stars in Es. As a consequence, numerical simulations of galaxy merging in presence of gas (see, e.g., Bekki 1998), taking also into account the feedback from the central BH in a self-consistent way (see, e.g., Tabor & Binney 1993, Binney & Tabor 1995, Ciotti & Ostriker 1997, 2001), and finally a better understanding of BH merging (see, e.g. Merritt & Ekers 2002; Hughes & Blandford 2002) are highly needed for a substantial progress in this field.

7. Galactic cannibalism in the galaxy cluster C0337-2522 at $z \simeq 0.59$

In the present Chapter we consider the dynamical evolution of a group of five Es observed in the core of the galaxy cluster C0337-2522. In particular, with the aid of numerical simulations we explore the hypothesis that this system represents the early stage of the process of BCG formation.

7.1 Introduction

According to the galactic cannibalism scenario BCGs, and in particular CDs, are formed by merging and accretion of galaxies at the center of galaxy clusters (Ostriker & Tremaine 1975, Hausman & Ostriker 1978). In this picture, cluster galaxies are expected to spiral (as an effect of dynamical friction), towards the bottom of the cluster potential, and eventually form there a superluminous elliptical. From an observational point of view, there are indications *a posteriori* of the reliability of this process, such as the presence of multiple nuclei in many BCGs (see, e.g., Matthews, Morgan & Schmidt 1964, Laine et al. 2003). On the other hand, examples of the stage *before* merging of this process are lacking.

As outlined in Chapter 1, we have identified a possible candidate for *a real example of the early stage of galactic cannibalism*. This system is a group of five elliptical galaxies near the center of the cluster C0337-2522 at redshift $z \simeq 0.59$. The five galaxies are located within a region of a few kpc of (projected) linear size, and our ESO-VLT images do not reveal the presence of a common luminous halo (Treu et al., in preparation). We studied the dynamical evolution of such a system in order to explore whether this represents a natural progenitor of a super-luminous elliptical: this hypothesis is investigated by using numerical simulations, in which the galaxies are represented as N-body systems.

In these simulations, presented in this Chapter, the initial conditions are constrained by the imaging and kinematic information from the ESO-VLT data cited above. The observations provide, for each galaxy, only three phase-space coordinates (the two projected positions and the line-of-sight velocity). Thus, some assumptions are needed in order to assign the initial conditions to the dynamical system under investigation. In principle, one could make use of non-parametric estimators (see Merritt & Trembley 1994). However, given the small number of

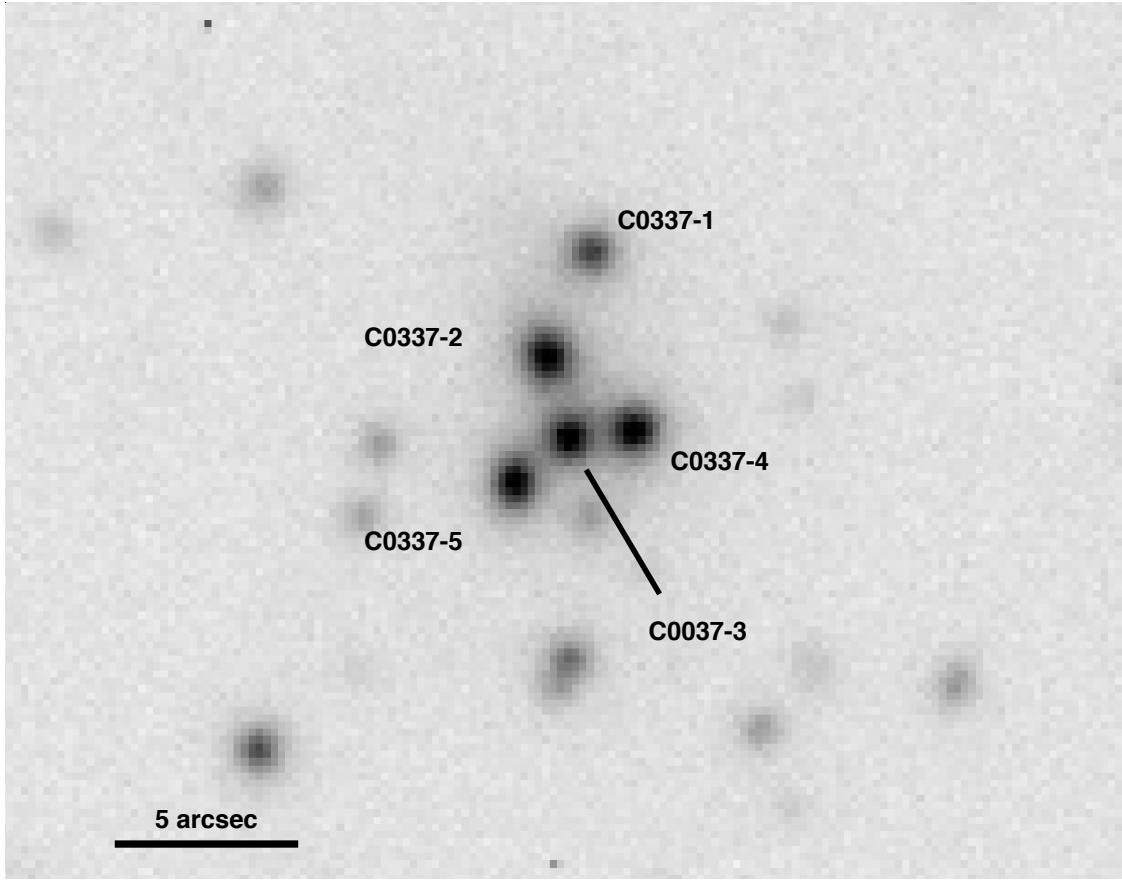


Figure 7.1: VLT-FORS1 I-band image of the galaxy cluster C0337-2522 (N up, E left). The five galaxies are named as in Table 7.1.

objects involved, such estimators are not practical for our application. To overcome this problem, we modeled the cluster where the five galaxies reside as a spherical DM density distribution with adjustable total mass, scale length and amount of radial orbital anisotropy in the velocity distribution. In order to explore the effects of the dynamical friction of the studied galaxies against the cluster DM, the cluster is also represented as a *live* N-body system.

The main goal of this Chapter is to explore, as a function of the initial conditions and of the structural and dynamical characteristics of their parent cluster, how many, if any of the five galaxies under consideration will merge before $z = 0$. Furthermore, in case of merging we investigate whether the remnant has the surface brightness (SB) profile typical of cD galaxies, i.e., it possesses a diffuse low luminosity halo. In addition, we check whether some features of elliptical galaxies, such as the FP, the FJ relation, the $M_{\text{BH}}-\sigma_0$ relation (see Chapter 2) and the metallicity gradient (Peletier 1989, Carollo, Danziger & Buson 1993), are preserved by the process.

7.2 Observations and data reduction

The five galaxies that we have considered are located in the core of the galaxy cluster C0337-2522. The I-band image, shown in Fig. 7.1, was obtained¹⁰ in September 1999, using the Focal Reducer and Spectrograph 1 (FORS1) at the ESO Very Large Telescope (VLT) with exposure time 2×300 s and seeing $0.9''$. The image was reduced with standard procedure and a catalogue of the objects was carried out with the SExtractor package (Bertin & Arnouts 1996). Spectra for the five elliptical galaxies were obtained in January 2000 with FORS1 at VLT, using the grism R600 and a $1''$ wide slit with a resolution of $\approx 90 - 100 \text{ km s}^{-1}$. Exposure times were in the range 2700s – 7200s. The reduction of the spectroscopic data and the measurement of the redshifts were performed following the procedures described in Treu et al. (2001). The redshifts of the five galaxies are reported in Table 7.1. We note that, due to poor weather conditions and reduced reflectivity during the early-stages of operations (see, e.g., Labbé et al. 2002), the signal-to-noise ratio of the spectroscopic data does not allow us to measure with sufficient accuracy the central velocity dispersions for all the five galaxies. Thus, in the present investigation we are unable to use velocity dispersion measurements in order to constrain the total mass of the galaxies and their internal dynamics. In addition, we do not report details on the photometric measurements. We just recall that the five objects span a range of ~ 0.5 in I-band magnitude. Thus, for the purpose of our investigation, we can safely assume that they have comparable mass.

7.3 Models

In the numerical simulations presented in this Chapter, the initial conditions for the cluster and the galaxies are spherically symmetric density distributions. In particular, for the DM distribution of the cluster we use a $\gamma = 1$ model (see Section 3.1). For the galaxies we use both one-component $\gamma = 1$ and two-component (1,1) models (see Section 3.2). In what follows, the cluster density profile is indicated as $\rho_{\text{cl}}(r)$, $M_{\text{cl,tot}}$ is the total cluster mass, $\Psi_{\text{cl}}(r)$ is the relative (positive) cluster potential, and r_{cl} is the cluster “core radius”. The galaxy stellar and DM components (when present) are identified by the same notation, with the subscripts “*” and “h”, respectively. In the two-component models we always assume $M_{\text{h}} \equiv 5M_*$ and $r_{\text{h}} \equiv 3r_*$.

In a subset of simulations, the cluster and/or the galaxy stellar components are radially anisotropic, while for sake of simplicity the galactic DM halo component is instead always isotropic. Radial orbital anisotropy is introduced as described in Section 3.1. Following the adopted notation, we indicate the anisotropy radius of the cluster and of the galaxies as $r_{\text{a,cl}}$ and $r_{\text{a,*}}$, respectively.

We note that a certain amount of radial anisotropy in the orbital distribution is expected, at least in a few scenarios of formation, for both elliptical galaxies (see, e.g., van Albada 1982, Barnes 1992, Hernquist 1993) and clusters (see, e.g., Crone,

¹⁰The imaging and spectroscopic observations were collected by M. Stiavelli and T. Treu at the European Southern Observatory Very Large Telescope at Paranal (proposals 63.O-0591 and 64.O-0298). The data reduction was performed by T. Treu.

Evrard & Richstone 1994, Cole & Lacey 1996, Ghigna et al. 1998). However, there exist observational and theoretical indications that radial anisotropy should be of modest amount in the both cases (see Chapter 5, and, e.g., Carollo et al. 1995b, CL97, van der Marel et al. 2000, Gerhard et al. 2001, NLC02), even at significant look-back times (Koopmans & Treu 2003).

7.4 Numerical simulations

7.4.1 Initial conditions

Our coordinate system is selected so that the x -axis runs east–west, the y -axis runs south–north and the z -axis is along the line–of–sight. Clearly, observations provide only 3 of the required 6 initial phase–space coordinates of the center of mass of each galaxy, namely two positions in the (x, y) projected plane and the line–of–sight velocity v_z . The problem of the orbital evolution of the five galaxies is thus underdetermined, and the missing initial coordinates force us towards a probabilistic approach, where several initial conditions compatible with the observational constraints are adopted and used to evolve the system from $z \simeq 0.59$ to the present. We assume, for simplicity, that the five galaxies have equal masses (consistently with the considerations at the end of Section 7.2), and that in the inertial reference system centered on the cluster center $\sum x_i = \sum y_i = \sum z_i = 0$ and $\sum v_{x,i} = \sum v_{y,i} = \sum v_{z,i} = 0$, summing over the five galaxies. In Table 7.1 we report the values of the known coordinates for the five galaxies, reduced to the reference system (we adopted $\Omega_m = 0.3$, $\Omega_\Lambda = 0.7$, and $H_0 = 65 \text{ km s}^{-1} \text{ Mpc}^{-1}$).

As a first step, in order to recover the missing coordinates of the galaxies, we fix the structural and dynamical properties of the cluster model, by choosing the values of the parameters $s_{a,cl}$, r_{cl} , and $M_{cl,tot}$ (see Sections 3.2 and 7.3). We investigated two cases for the DF of the cluster: the isotropic case (corresponding to $s_{a,cl} \equiv r_{a,cl}/r_{cl} = \infty$) and the radially anisotropic case with $s_{a,cl} = 1.8$, a value that fiducially corresponds to the maximum degree of radial anisotropy compatible with stability for the one–component $\gamma = 1$ model (see Section 5.3.1). For the core radius of the DM cluster density distribution r_{cl} , we adopt the values 100 kpc and 300 kpc (corresponding to half-mass radius $r_{M,cl} \simeq 241 \text{ kpc}$ and $r_{M,cl} \simeq 724 \text{ kpc}$, respectively). For a fixed r_{cl} there is a minimum cluster mass (M_{min}) for which all the five galaxies, with the observed coordinates (x, y, v_z) , are bound, under the implicit assumption that the cluster DM is virialized (consistently with the time independence of the cluster potential; see Section 7.3). For each galaxy, the lower limit to the cluster mass corresponds to the case of vanishing v_x , v_y and z : then the minimum mass is given by the maximum for the five galaxies of these lower limits. Considering the values in Table 7.1 and the expression of the cluster potential (equation 3.3 with $\gamma = 1$), we obtain $M_{min} \simeq 4.4 \times 10^{13} M_\odot$, when $r_{cl} = 100 \text{ kpc}$, and $M_{min} \simeq 1.28 \times 10^{14} M_\odot$, in the case $r_{cl} = 300 \text{ kpc}$. It is clear that in the limiting case $M_{cl,tot} = M_{min}$, the least bound of the galaxies has a vanishing phase–space volume available. For this reason, we consider values of the cluster mass $M_{cl,tot} > M_{min}$, exploring, for each choice of r_{cl} , two different cases: $M_{cl,tot} = \tilde{M}$, in which one of the galaxies is weakly bound, and $M_{cl,tot} = 2\tilde{M}$, in which, on

Table 7.1: Known data for the five galaxies. Positions and velocities are relative to the center of mass of the system. For reference, the center of galaxy C0337-4 is at $\alpha = 03^{\text{h}}37^{\text{m}}45.15^{\text{s}}$ and $\delta = -25^{\circ}22'36.1''$ (J2000).

Galaxy	redshift	x (arcsec)	y (arcsec)	v_z (km/s)	x (kpc)	y (kpc)
C0337-1	0.589	0.51	3.78	284.7	3.63	27.00
C0337-2	0.578	-0.36	0.94	-1892.9	-4.51	6.71
C0337-3	0.590	-0.01	-1.24	473.3	-0.09	-8.86
C0337-4	0.592	1.63	-1.04	850.2	11.63	-7.43
C0337-5	0.589	-1.49	-2.44	284.7	-10.66	-17.43

the contrary, all the galaxies are expected to be well bound ($\tilde{M} \simeq 1.1M_{\text{min}}$ when $s_{\text{a,cl}} = 1.8$, and $\tilde{M} \simeq 1.2M_{\text{min}}$ when $s_{\text{a,cl}} = \infty$).

Now that the properties of the cluster are fixed, we can use general physical principles to constrain the missing phase-space information. A first basic requirement that we impose on the unknown coordinates (z, v_x, v_y) is that they correspond to objects bound to the cluster, i.e., for each galaxy $v_x^2 + v_y^2 < 2\Psi_{\text{cl}}(x, y, z) - v_z^2$, where we neglected the galaxy-to-galaxy contribution to the binding energy. In principle, for a given cluster density profile, and without extra assumptions on the dynamical status of the five galaxies, all the sets of phase-space coordinates corresponding to bound galaxies and to a null barycentric motion should be accepted. Under the hypothesis that the five galaxies follow the same DF as the cluster DM, we can proceed with a more detailed discussion on the selection of the initial conditions.

In our approach, we first obtain the coordinate z for each galaxy, by applying the von Neumann rejection method (see, e.g., Aarseth, Henon & Wielen 1974) to the mass profile of the cluster (equation 3.2 with $\gamma = 1$). Once the position of the galactic center of mass is fixed, we recover the two unknown velocities v_x and v_y , again by application of the von Neumann rejection method to the cluster DF, where r and v_z are fixed. As a rule, when extracting the initial conditions, we check for the phase-space coordinates of the barycenter of the 5 galaxies, discarding realizations in which the discrepancy in position and velocity is larger than 10% of r_{cl} and $(GM_{\text{cl,tot}}/r_{\text{cl}})^{1/2}$, respectively. However, we also performed a few simulations in which the barycentric property of the five galaxies is perfectly realized, finding that the results of interest are not affected by the assumed tolerance on the center of mass of the system.

At the beginning of each simulation the five (one-component) galaxies are identical $\gamma = 1$ models with core radius $r_* \simeq 2.2$ kpc (which corresponds to an effective radius $R_e = 4$ kpc), and stellar mass $M_* = 4 \times 10^{11} M_{\odot}$. In the two-component case, the stellar mass is reduced to $M_* = 2 \times 10^{11} M_{\odot}$, and the galactic DM halo is more massive and more extended than the stellar component ($M_{\text{h}} = 10^{12} M_{\odot}$ and $r_{\text{h}} \simeq 6.6$ kpc). When using two-component galaxy models, we reduce the diffuse dark component of the cluster by an amount corresponding to $5M_{\text{h}}$, so that the total amount of DM in the N-body simulations is the same as in the one-component case. We also explore some cases of (one-component) radially

anisotropic galaxy models, by assuming $s_{a,*} \equiv r_{a,*}/r_* = 1.8$. With the adopted values of the parameters, the half-mass dynamical time of the galaxies (as defined in Section 3.3) is $T_{\text{dyn}} \simeq 2.0 \times 10^7$ yr and $T_{\text{dyn}} \simeq 4.8 \times 10^7$ yr in the one and two-component case, respectively.

Summarizing, our initial conditions are characterized by the properties of the cluster, which are fully determined by the three parameters $(r_{\text{cl}}, M_{\text{cl,tot}}, s_{a,\text{cl}})$, by those of the galaxies (presence or absence of galactic DM halos, $s_{a,*}$), and by the particular realization considered. Clearly, the results of the simulations depend, for a given set of cluster and galaxies parameters, also on the specific values of the initial positions and velocities of the five galaxies. Thus, it is natural to wonder about the statistical significance that should be associated to the result of a single simulation or to a set of simulations relative to given cluster and galaxies parameters.

In order to address this issue, we start out by considering the idealized case in which the whole available parameter space is explored by the simulations. In this case, any result of interest \mathcal{R} (e.g., the number of merging galaxies or the time of the last merging) is a function of the missing phase-space coordinates: $\mathcal{R} = \mathcal{R}(\mathbf{w}_1, \mathbf{w}_2, \mathbf{w}_3, \mathbf{w}_4, \mathbf{w}_5)$, where $\mathbf{w}_i = (z_i, v_{x,i}, v_{y,i})$ for $i = 1, 5$. Under the additional assumption that the dynamical evolution of each galaxy is independent of the initial positions and velocities of the other galaxies (justified in the considered scenario, in which the dominant dynamical mechanism is the dynamical friction of the galaxies against the diffuse cluster DM), the statistical weight of each simulation can be obtained by considering the product of the five reduced DFs, $f_i(\mathbf{w}_i) = f(x_{i,0}, y_{i,0}, v_{z,i,0}, \mathbf{w}_i)$. Accordingly, the statistically weighted result can be written

$$\langle \mathcal{R} \rangle = \frac{1}{\mathcal{N}} \int \mathcal{R}(\mathbf{w}_1, \mathbf{w}_2, \mathbf{w}_3, \mathbf{w}_4, \mathbf{w}_5) \prod_{i=1}^5 f_i(\mathbf{w}_i) d^3 \mathbf{w}_i, \quad (7.1)$$

where the normalization \mathcal{N} is given by

$$\mathcal{N} = \int \prod_{i=1}^5 f_i(\mathbf{w}_i) d^3 \mathbf{w}_i. \quad (7.2)$$

In case of a finite number of simulations N , equations (7.1) and (7.2) become

$$\langle \mathcal{R} \rangle = \frac{1}{\mathcal{N}} \sum_{k=1}^N \mathcal{R}(\mathbf{w}_{1,k}, \mathbf{w}_{2,k}, \mathbf{w}_{3,k}, \mathbf{w}_{4,k}, \mathbf{w}_{5,k}) \prod_{i=1}^5 f_i(\mathbf{w}_{i,k}), \quad (7.3)$$

where now

$$\mathcal{N} = \sum_{k=1}^N \prod_{i=1}^5 f_i(\mathbf{w}_{i,k}). \quad (7.4)$$

In reality, we normally considered just 2 realizations for each set of parameters, as can be seen in Table 7.2, where the main properties of the simulations are reported. In one case we explored 7 different realizations (simulations #7-13). In particular, we will use equations (7.3) and (7.4) in order to quantify the expected merging time.

7.4.2 Numerical methods

For the numerical N-body simulations described in this Chapter we used both the serial and parallel versions of the GADGET code (see Section 4.2.2). We recall here that both the galaxies and the cluster are represented with particles. Once the position and velocity of the center of mass of each galaxy were fixed by using the approach described in Section 7.4.1, the numerical realization of the initial conditions for the galaxies and for the cluster DM distribution was obtained by following the scheme described in Appendix A.1.

For the purpose of this work we are interested in the dynamical evolution of the system up to $z = 0$. Thus, the total time of each simulation is $t_{\text{tot}} = t(0) - t(z_{\text{cl}})$, where $z_{\text{cl}} \simeq 0.59$ is the redshift of the cluster. In the standard Λ CDM cosmology, as described in Section 7.4.1, $t_{\text{tot}} \simeq 6.1$ Gyr, corresponding to more than $100 T_{\text{dyn}}$ of the galaxies and from 10 up to 50 cluster dynamical times, depending on $M_{\text{cl,tot}}$ and r_{cl} . All the relevant properties of the numerical simulations are reported in Table 7.2, where different cluster parameters are separated by horizontal lines, so that the results within each group correspond to different realizations of the initial conditions.

The choice of the number of particles was determined by practical computational time limits and by the requirement that all the particles (DM and stellar components of galaxies and DM of cluster) have the same mass. For these reasons, simulations characterized by different cluster and galaxies parameters were run with different number of particles. We note that in case of high mass ratio between the cluster and the galaxies (for example, when $r_{\text{cl}} = 300$ kpc and $M_{\text{cl,tot}} = 2\tilde{M}$) even a large number of cluster particles (N_{cl}) implies a small number of stellar (N_*) and halo (N_{h}) galaxy particles.

According to the discussion in Section 4.3, we adopted the following values of the GADGET parameters: $\alpha = 0.02$, $\Delta t_{\text{min}} = 0$, $\Delta t_{\text{max}} = T_{\text{dyn}}/100$ (where T_{dyn} is the initial half mass dynamical time of each galaxy, see Section 3.3), $\alpha_{\text{tol}} = 0.05$, and $\varepsilon = R_{\text{e}}/5 \simeq 0.36 r_*$ (where R_{e} is the initial effective radius of the galaxies).

7.5 Results: merging statistics and time-scales

The first goal of this Chapter is to investigate whether any, a few, or all of the five galaxies merge into a unique system before $z = 0$, to verify whether the studied system is indeed a good candidate for a practical example of galactic cannibalism. In Column 11 of Table 7.2 we report the number N_{merg} of galaxies involved in a merging within the total time of the simulation (always 6.1 Gyr), and, in Column 12, the time T_{last} (calculated from the beginning of the simulation, with a resolution of 0.5 Gyr) at which the last merging occurs. A first inspection of Table 7.2 (leaving out the “special” simulations #1f and #7f) reveals that, in *all* the performed simulations, at least 3 galaxies merge before $z = 0$, thus suggesting that *a multiple merging event in the central group of five galaxies in the cluster C0337-2522 will take place in the next few Gyrs.*

As already pointed out in the Introduction, we based our investigation on the hypothesis that the driving mechanism leading to the galaxy merging is the dynamical friction against the cluster DM, making them spiral towards the

Table 7.2: Simulations parameters.

#	r_{cl}	$M_{\text{cl,tot}}$	$s_{\text{a,cl}}$	N_{cl}	M_*	$s_{\text{a,*}}$	N_*	M_{h}/M_*	N_{h}	N_{merg}	T_{last}
1	100	4.8	1.8	235520	4	∞	2048	0	-	4	3.0
2	100	4.8	1.8	29440	4	∞	256	0	-	4	1.0
1a	100	4.8	1.8	58880	4	1.8	512	0	-	4	3.0
1h	100	4.8	1.8	107520	2	∞	512	5	2560	4	2.0
3	100	5.3	∞	130560	4	∞	1024	0	-	4	1.5
4	100	5.3	∞	32640	4	∞	256	0	-	4	2.0
3a	100	5.3	∞	65280	4	1.8	512	0	-	4	1.5
3h	100	5.3	∞	120320	2	∞	512	5	2560	4	1.0
5	100	9.6	1.8	60160	4	∞	256	0	-	5	3.0
6	100	9.6	1.8	120320	4	∞	512	0	-	5	3.5
5a	100	9.6	1.8	120320	4	1.8	512	0	-	5	3.0
6h	100	9.6	1.8	115200	2	∞	256	5	1280	5	3.5
7	100	10.6	∞	266240	4	∞	1024	0	-	5	2.5
8	100	10.6	∞	66560	4	∞	256	0	-	5	4.5
9	100	10.6	∞	66560	4	∞	256	0	-	5	3.5
10	100	10.6	∞	66560	4	∞	256	0	-	5	4.0
11	100	10.6	∞	66560	4	∞	256	0	-	5	2.0
12	100	10.6	∞	66560	4	∞	256	0	-	5	2.5
13	100	10.6	∞	33280	4	∞	128	0	-	5	2.5
7a	100	10.6	∞	133120	4	1.8	512	0	-	5	2.5
7h	100	10.6	∞	128000	2	∞	256	5	1280	5	2.5
14	300	13.5	1.8	85120	4	∞	256	0	-	4	1.5
15	300	13.5	1.8	85120	4	∞	256	0	-	4	2.5
14a	300	13.5	1.8	170240	4	1.8	512	0	-	4	1.5
14h	300	13.5	1.8	165120	2	∞	256	5	1280	4	1.5
16	300	15.3	∞	96640	4	∞	256	0	-	4	2.5
17	300	15.3	∞	193280	4	∞	512	0	-	3	2.0
16a	300	15.3	∞	96640	4	1.8	256	0	-	4	2.5
17h	300	15.3	∞	188160	2	∞	256	5	1280	5	5.5
18	300	27.0	1.8	171520	4	∞	256	0	-	4	3.0
19	300	27.0	1.8	171520	4	∞	256	0	-	5	6.0
18a	300	27.0	1.8	171520	4	1.8	256	0	-	4	3.0
18h	300	27.0	1.8	168960	2	∞	128	5	640	5	5.5
20	300	30.6	∞	194560	4	∞	256	0	-	3	1.0
21	300	30.6	∞	194560	4	∞	256	0	-	4	1.5
20a	300	30.6	∞	194560	4	1.8	256	0	-	3	1.0
20h	300	30.6	∞	192000	2	∞	128	5	640	3	1.0
1f	100	4.8	-	-	4	∞	2048	0	-	2	1.5
7f	100	10.6	-	-	4	∞	1024	0	-	2	0.5

In the first column the name of each simulation is given. r_{cl} : cluster core radius in kpc. $M_{\text{cl,tot}}$: cluster mass in units of $10^{13} M_{\odot}$. $s_{\text{a,cl}}$: cluster anisotropy parameter. N_{cl} : number of cluster particles. M_* : galaxy stellar mass in units of $10^{11} M_{\odot}$. $s_{\text{a,*}}$: galaxy anisotropy parameter. N_* : number of stellar particles per galaxy. M_{h} : galaxy halo mass in units of $10^{11} M_{\odot}$. N_{h} : number of halo particles per galaxy. N_{merg} : number of merging galaxies. T_{last} : time elapsed from the beginning of the simulation when the last merging occurs (in Gyrs). The subscript “a” to the simulation name indicates that the galaxies are anisotropic, while “h” indicates the presence of galactic DM halos; finally, “f” means that the cluster potential is maintained fixed during the simulation.

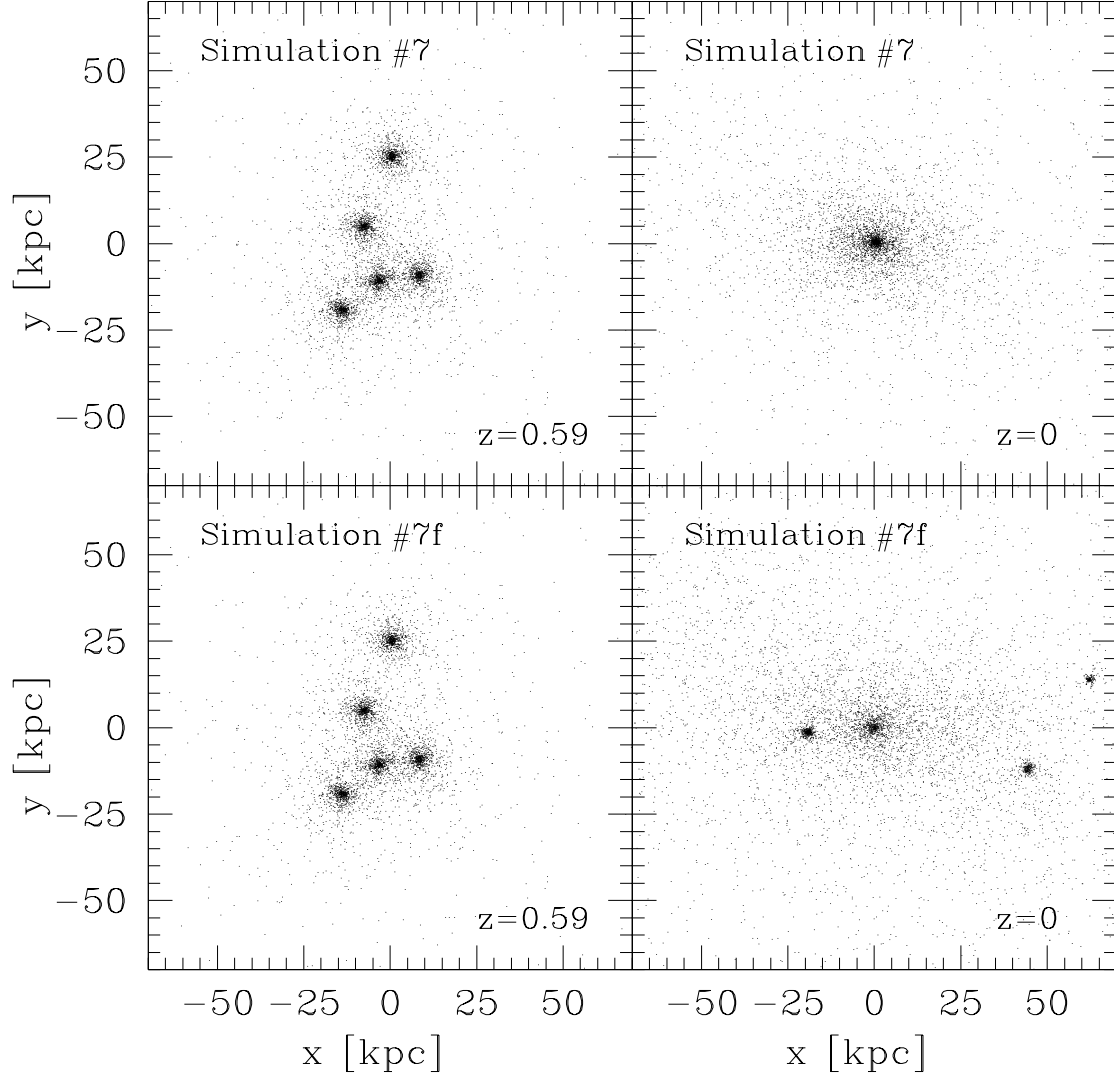


Figure 7.2: *Top panels:* snapshots of the initial ($z = 0.59$, left panel) and final ($z = 0$, right panel) distribution of the stellar particles in the projected plane (x, y) for the simulation #7. *Bottom panels:* the same as top panels, but for the simulation #7f. We recall here that the two simulations have identical initial conditions, the only difference being that in the simulation #7 the cluster DM is represented with particles, while in the simulation #7f as a fixed potential (see Table 7.2). The effect of dynamical friction is apparent when comparing the final snapshots.

cluster center. In order to verify the reliability of this hypothesis, we also ran two simulations by modeling the cluster as a *frozen* DM distribution: these two simulations (#1f and #7f) have the same initial conditions as the simulations #1 and #7, respectively. We found that, at variance with the simulations #1 and #7 (where 5 galaxies merge), in the simulations #1f and #7f only 2 galaxies merge before $z = 0$. On the basis of these results we confirm that the dynamical friction of the galaxies against the cluster DM is the primary mechanism responsible for the galactic cannibalism. The merging of two galaxies in case of frozen halo can be interpreted as a secondary effect of galaxy–galaxy interaction. In Fig. 7.2 we plot, as an example, the initial (left panels) and final (right panels) distributions in the projected plane (x, y) of the *stellar* particles for the simulation #7 and #7f: at $z = 0$ a single galaxy is formed in case of live cluster DM (upper right panel in Fig. 7.2), while four distinct stellar systems are still present in case of frozen cluster DM (lower right panel in Fig. 7.2).

As already pointed out in Section 7.4.1, for given cluster parameters, as a rule we explored 2 (but in one case 7) different realizations of the initial conditions, identified in Table 7.2 by groups separated by horizontal lines. One of the realizations in each group is also used as initial condition for simulations with anisotropic galaxy models (named with the number of the corresponding isotropic simulation with the subscript “a” in Table 7.2). Similarly, in order to explore the effects of galactic DM halos, for each group we ran also a simulation with two–component galaxy models. These simulations are named in Table 7.2 with the number of the corresponding one–component simulation with the subscript “h”. As expected, the number of merging galaxies N_{merg} and the characteristic merging time-scale do not change if anisotropic, instead of isotropic, galaxy models are used in the initial conditions. We recall here that the choice of exploring cases with anisotropic initial galaxy models was aimed at investigating possible effects on the properties of the end–products (see following Sections). As also expected, in the simulations in which two–component (and then, with the adopted parameters, more massive) galaxy models are used, dynamical friction is more effective than in absence of galactic DM. In some two–component cases more galaxies merge than in the corresponding one–component simulations; in other cases, N_{merg} is the same, but T_{last} is shorter (of $0.5 - 1$ Gyr) when galactic DM halos are present. We note that T_{last} is by definition dependent on the number of merging and it is not a direct measure of the dynamical friction time-scale (T_{fric} , that we define empirically as the time in which a galaxy reaches the center of the cluster as a consequence of the interaction with the diffuse DM). This can be seen, for example, by considering the simulations #3 and #7. In the former, 4 galaxies merge in 1.5 Gyr, while, in the latter, 5 galaxies merge in 2.5 Gyr. In this case, the dynamical friction time-scale, as defined above, is of course shorter in the case of 5 merging galaxies, even if T_{last} is larger.

A more detailed analysis is required to address the dependence of the number of merging galaxies and of the merging time-scales on the cluster parameters and the particular realization considered. We found that T_{last} (which lies in the the range $1.0 - 6.0$ Gyr) depends on both the cluster parameters and the realization. This is not surprising, since the dynamical friction time-scale is a function of both the cluster density and the initial velocity of the galaxies. The general trend is that

the number of merging galaxies is nearly independent of the specific realization for given cluster parameters, and does not depend strongly on the cluster properties either. In particular, as a general result N_{merg} is found to be insensitive to the adoption of “minimum mass” hypothesis ($M_{\text{cl,tot}} = \tilde{M}$; see Section 7.4.1). However, one could ask what is special with the set of simulations from #5 to #13, in all of which 5 galaxies merge. In order to answer this question it is necessary to try a rough quantitative evaluation the dynamical friction time-scale T_{fric} . As it is well known, $T_{\text{fric}} \propto v^3/\rho_{\text{cl}}$, where v is the modulus of the velocity vector of the galaxy and ρ_{cl} is the cluster density (see, e.g., Binney & Tremaine 1987). By substituting in this expression, as a rough estimation of the density, $\rho_{\text{cl}} = M_{\text{cl,tot}}/r_{\text{cl}}^3$, it follows $T_{\text{fric}} \propto v^3 r_{\text{cl}}^3 / M_{\text{cl,tot}}$. Thus, it is clear that *for fixed galaxy velocity* the dynamical friction time-scale increases for increasing cluster radius and for decreasing cluster mass. However, there is no reason to expect that galaxies in different simulations have similar initial velocities. A quantitative comparison can be done only if the “real” initial velocities are taken into account. We note that in the cases in which 4 galaxies merge it is always galaxy C0337-2 (characterized at $t = 0$ by the highest absolute value of line-of-sight velocity, see Table 7.1) that survives as an individual object for the time interval covered by the simulations. We find that, even when considering the “real” initial velocities of the galaxy C0337-2 in the various simulations, the expected T_{fric} is actually larger when it survives than when it merges.

As outlined above, the merging time-scale, for fixed cluster and galaxies properties, is found to be dependent on the particular realization of the initial conditions. On the basis of the discussion in Section 7.4.1., we can determine, for each set of simulations with the same cluster and galaxy properties, the statistically weighted value of the merging time-scale. As an example, we focus here on the set of 7 simulations from #7 to #13, in all of which 5 galaxies merge. By applying equation (7.3), considering as result of interest the time of last merging T_{last} , we find that in this case the statistically weighted last merging time is $\langle T_{\text{last}} \rangle \simeq 2.3 \pm 0.3$ Gyrs, where the uncertainty has been computed by considering an uncertainty of 0.5 Gyr associated to T_{last} in each simulation.

7.6 Results: properties of the end-products

We define the end-product of a simulation as the stellar system composed by the bound particles initially belonging to the galaxies involved in the merging process. In evaluating the binding energy of the particles, we consider the gravitational potential generated by both the cluster and the remnant galaxy mass distribution. As the merger lies at the bottom of the cluster potential, we always find that the fraction of unbound particles is negligible. Thus, in the following we can safely assume that the mass of the remnant is given by the sum of the masses of its progenitors.

We measured some intrinsic and projected quantities of the end-products: the intrinsic axis ratios c/a and b/a (where a, b, c are respectively the longest, intermediate and shortest axis of the associated inertia tensor), the angle-averaged half mass radius, the virial velocity dispersion and the total angular momentum, and, for a set of 50 random projections, the circularized effective radius, the projected

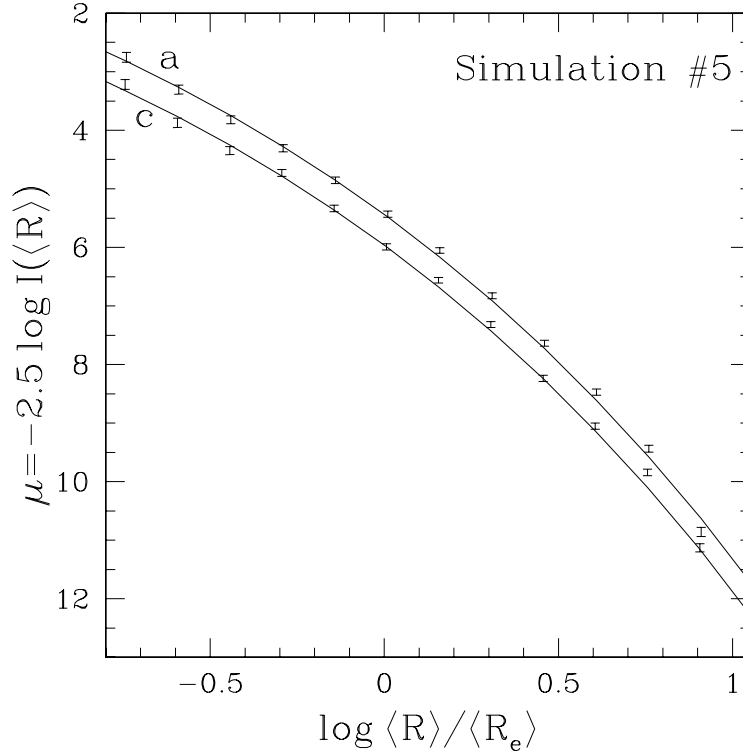


Figure 7.3: Circularized SB profiles and corresponding $R^{1/4}$ best-fit of the end-product of 5 merging galaxies projected along its major axis (a) and minor axis (c). The data are relative to the simulation #5.

central velocity dispersion, the ellipticity and the circularized SB profile. In the treatment of the outputs of the numerical simulations we followed the scheme described in Appendix A.2. In order to limit the uncertainties due to discreteness effects, we analysed the intrinsic and “observational” properties of the end-products with at least $n \times 512$ stellar particles (where n is the number of galaxies involved in merging). To satisfy this condition and to explore the properties of the end-products of all the considered initial conditions, we ran, for each choice of the cluster parameters, at least one simulation with 512 stellar particles per galaxy. The only exception is the case ($r_{\text{cl}} = 300$ kpc, $M_{\text{cl,tot}} = 2\tilde{M}$) in which we used 256 stellar particles per galaxy.

7.6.1 Structural and dynamical parameters

The merging end-product is in general well described by a triaxial ellipsoid with axis ratios in the range $0.5 \lesssim c/a \lesssim 0.9$. In a few cases we found oblate systems with $c/a \simeq c/b \simeq 0.5 - 0.7$. These oblate systems are mainly flattened by rotation. Their angular momenta (normalized to the typical scales of the system: total mass M , virial velocity dispersion σ_V , and half mass radius r_M) are, in modulus, among the highest observed in the sample of end-products. In addition, a significant degree of alignment between the angular momentum and the minor axis of the inertia tensor is found in these cases.

In the case of isotropic one-component initial models the end-products of merging of 5 galaxies (with total stellar mass $M_* = 2 \times 10^{12} M_\odot$) have circularized effective radius in the range $12 \lesssim \langle R \rangle_e \lesssim 21$ kpc, and central velocity dispersion (measured inside an aperture of equivalent radius $\langle R \rangle_e/4$) in the range $320 \lesssim \sigma_0 \lesssim 410 \text{ km s}^{-1}$. In case of merging of 3 or 4 galaxies ($M_* = 1.2 \times 10^{12} M_\odot$ and $M_* = 1.6 \times 10^{12} M_\odot$, respectively) we found $10 \lesssim \langle R \rangle_e \lesssim 12$ kpc, and $290 \lesssim \sigma_0 \lesssim 392 \text{ km s}^{-1}$. Approximately the same ranges are spanned by $\langle R \rangle_e$ and σ_0 of the end-products of merging of radially anisotropic galaxy models. In particular, there is not evidence of a systematically higher projected velocity dispersion of the end-products of radially anisotropic models, with respect to the merger of isotropic galaxies. The main characteristics of the end-products in the presence of DM associated with the single galaxies are not substantially different from those of the corresponding one-component cases, with the only exception of the central velocity dispersion, which is in general quite high ($300 \lesssim \sigma_0 \lesssim 491 \text{ km s}^{-1}$). The effective radii are in the range $7 \lesssim \langle R \rangle_e \lesssim 17$ kpc.

We note that the values of $\langle R \rangle_e$ are always comparable with those measured in real luminous Es (see, e.g., JFK96). In case of one-component progenitors, also the central velocity dispersion of the remnant lies in the same range as those measured in observations. On the other hand, in some simulations with two-component galaxies, the remnant is characterized by very large values of σ_0 , unusual even for giant Es and cD galaxies in the center of clusters, which have $\sigma_0 \lesssim 400 \text{ km s}^{-1}$ (see, e.g., Oegerle & Hoessel 1991). This could be due to the fact that in our two-component models the DM component dominates the total galactic mass distribution within the effective radius (see Section 7.3): merging of models with more diffuse galactic DM halo could be not affected by this problem. In addition, we recall here that the central velocity dispersion of the progenitors is not measured, but derives from the arbitrary choice of the galaxy length and mass scales. Thus, it is more significant comparing σ_0 of the remnant with that of its progenitors, than considering its absolute value.

7.6.2 Surface brightness profiles

One of the motivations for this investigation was the hypothesis that the system of five galaxies under investigation was an example of cD galaxy in formation. The most recognizable feature of cD galaxies is their SB profile, characterized by the $R^{1/4}$ law in the inner part and by a systematic deviation from this law in the outer part (roughly for $\langle R \rangle / \langle R \rangle_e \gtrsim 3$, where $\langle R \rangle$ is the circularized projected radius), due to the presence of a diffuse luminous halo (see, e.g., Sarazin 1986, Tonry 1987). Thus, we analysed the circularized SB profiles of three different projections (along the three principal axes) of each end-product, by fitting them with the standard de Vaucouleurs (1948) $R^{1/4}$ law. The profiles are fitted in the radial range $0.2 \lesssim R / \langle R \rangle_e \lesssim 10$ with average residuals between the data and the fits in the range $0.2 \lesssim \langle \Delta \mu \rangle \lesssim 0.5 \text{ (mag arcsec}^{-2}\text{)}$. These residuals are not small. However, we note that the fit is performed over a quite large radial range and that in any case the deviation from the $R^{1/4}$ law is not a systematic excess at large radii; this can be seen, for example, in Fig. 7.3, where we plot the circularized SB profile of the end-product of the simulation #5, projected along its minor and major axis, fitted with the $R^{1/4}$ law. We also fitted the profiles with the Sersic (1968) $R^{1/m}$

law (equation 5.4; see also Appendix A.3). Thanks to the additional parameter m , we obtained better fits for the SB profiles, with the best-fitting parameter m in the range $3.5 \lesssim m \lesssim 6.8$ and $0.05 \lesssim \langle \Delta\mu \rangle \lesssim 0.25$ (mag arcsec $^{-2}$), while for the $\gamma = 1$ profile of the initial galaxies we found $m \simeq 3.5$, always over the radial range $0.2 \lesssim R/\langle R \rangle_e \lesssim 10$. Thus, the trend is of m increasing with merging, in agreement with what found in Chapter 6 (see NLC03a and Londrillo, Nipoti & Ciotti 2003). Also the end-products obtained from mergers of anisotropic initial systems have SB profiles quite well fitted by the $R^{1/4}$ law up to $R \simeq 10\langle R \rangle_e$, with average residuals $0.1 \lesssim \langle \Delta\mu \rangle \lesssim 0.6$ (mag arcsec $^{-2}$). Adopting the Sersic law as fitting function, we find the best-fit parameter in the range $3.7 \lesssim m \lesssim 6.4$. In addition, there is no significant difference in the light distribution of one and two-component end-products: also in the presence of galactic DM halos, there is not evidence of any systematic excess at large radii in the SB profile.

On the basis of these results, *we find no indications that the merger remnant will be similar to a cD galaxy. In contrast, it seems that the product of a multiple merger like that considered is more similar to a “normal” giant elliptical.* This is in agreement with Zhang et al. (2002) who have shown, for a different set of initial conditions, that collapse with substructure is not capable of producing a cD halo. Thus, it is likely that accretion of smaller (and lower density) galaxies is needed to produce a cD halo.

7.6.3 Fundamental Plane and Faber–Jackson relations

The previous analysis showed that the merging end-products have SB profiles typical of elliptical galaxies. Of course this requirement, even though necessary in order to reproduce “real” galaxies, is by far not sufficient to validate observationally the results of the simulations. As briefly discussed in the Introduction, real Es follow a few well defined scaling relations. In particular, in order for the described process to be indeed a viable formation mechanism, we need to investigate whether the end-products satisfy the FP and the FJ relations. We consider here the FP relation in the Johnson B-band in the form given in equation (2.1) with $\alpha = 1.20$, $\beta = -0.83$, and scatter around this best-fit r.m.s.=0.071 in $\log \langle R \rangle_e$ (JFK96). For the FJ relation, we refer to the best-fit obtained by Dressler et al. (1987) for Virgo galaxies (equation 2.8).

The FP and FJ relations are known to evolve with redshift consistently with passive evolution of the stellar populations and hence of the *stellar* mass-to-light ratio. However, we can simplify our treatment by “freezing” the stars (and therefore the evolution of the mass-to-light ratio), and assuming that the relevant relations for both the progenitors and the end-products are the local FP and FJ. Therefore all values of mass-to-light ratio quoted in the following are values at $z = 0$. We associate the luminosity to our galaxy models by choosing the (position independent) stellar mass-to-light ratio $\Upsilon_* \equiv M_*/L_B$. We recall here that in the isotropic one-component case the five galaxies initially have effective radius $R_e = 4$ kpc, stellar mass $M_* = 4 \times 10^{11} M_\odot$ and central velocity dispersion $\sigma_0 \simeq 278$ kms $^{-1}$. In order to place them on the FP (and make them satisfy the FJ relation), we assume $\Upsilon_* = 6.5$ (in Blue solar units). Similarly, we assume $\Upsilon_* = 5.8$ in the anisotropic one-component case (in which $M_* = 4 \times 10^{11} M_\odot$ and $\sigma_0 \simeq 294$ kms $^{-1}$) and $\Upsilon_* = 1.9$ for

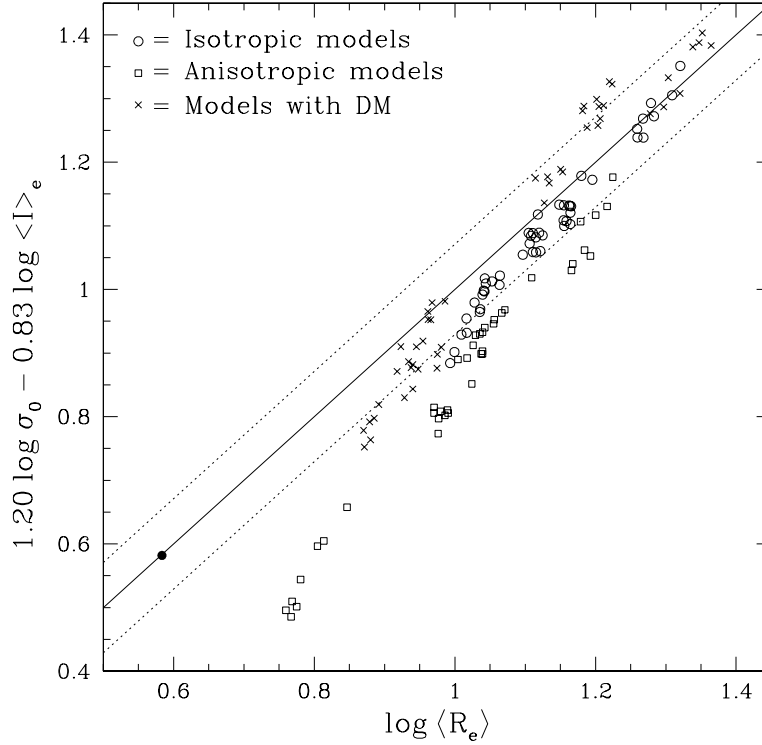


Figure 7.4: FP: best-fit relation (solid line) and its scatter (dotted lines; JFK96). Solid circle: initial conditions. Empty circles and squares: end-products of the merging of isotropic and anisotropic one-component galaxy models, respectively. Crosses: end-products in the two-component case. The plot represents 8 random projections of each end-product.

the two-component case (in which $M_* = 2 \times 10^{11} M_\odot$ and $\sigma_0 \simeq 282 \text{ km s}^{-1}$). These values of Υ_* remain constant during the evolution of the systems, consistently with the discussion above, and because we consider merging without gas and consequently without star formation.

In order to investigate the behavior of the end-products with respect to the FP relation, we measure their $\langle R \rangle_e$ and σ_0 and, knowing their luminosity (simply the sum of the luminosity of their progenitors; see the beginning of Section 7.6), we place them in the parameter space where the FP is defined. In Fig. 7.4 we plot the edge-on FP plane as given in equation (2.1), with the coefficients reported above. The solid line is the best-fitting relation of the observed FP, while the dotted lines correspond to the scatter around this relation. The solid circle represents the common initial position of the five galaxies. The position in the diagram of the (generally not spherically symmetric) end-products depends on the line-of-sight direction: each end-product, owing to projection effects, occupies a two dimensional region in Fig. 7.4 and is represented by a set of points corresponding to 8 random projections. A first interesting result is that *the projection effects* (evaluated over the whole solid angle), *though important, are not larger than the observed FP scatter*. In addition, as can be seen in Fig. 7.4, the behavior of the end-products with respect

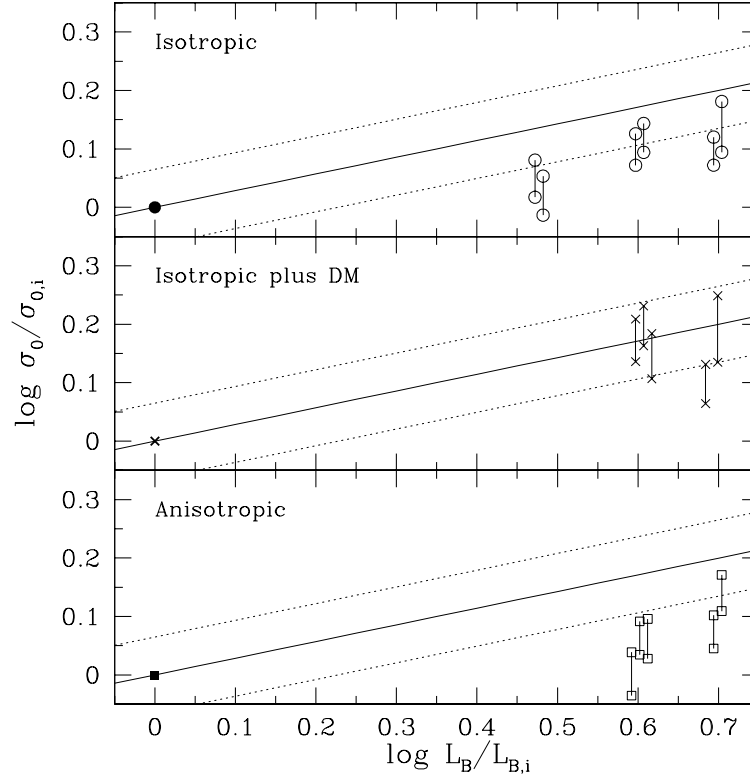


Figure 7.5: Central velocity dispersion of the final system vs. its total luminosity, in case of isotropic progenitors, progenitors with DM halo, and anisotropic progenitors. $L_{B,i}$ and $\sigma_{0,i}$ are the common luminosity and central velocity dispersion of each progenitor. The solid and dotted lines represent the FJ relation with its r.m.s. scatter, respectively. Vertical bars span the whole range of values of σ_0 due to the orientation of the line-of-sight with respect to each end-product: the horizontal split in each group of vertical bars is artificial, and it is introduced for clarity.

to the FP shows a certain dependence on the characteristics of the initial galaxies. In particular, the end-products corresponding to isotropic one-component (empty circles) and two-component (crosses) initial galaxy models are found near the FP, in positions compatible with its observational scatter, in accordance with what found in case of binary merging (see Chapter 6, NLC03a, NLC03b, Dantas et al. 2003). On the other hand, in the anisotropic one-component case (empty squares in Fig. 7.4) the end-products are placed significantly outside the FP and, in particular, they are systematically below the best-fit relation in Fig. 7.4. As will be pointed out in the following discussion about the FJ relation, this is mainly an effect of the too low central velocity dispersion of the end-products.

As outlined before, the fact that a galaxy satisfies the edge-on FP relation does not imply that it satisfies the FJ relation too, because the latter contains information about the displacement of Es on the FP itself. In Fig. 7.5 we plot the position of the end-products with respect to the FJ relation (solid line). The central velocity dispersion and the luminosity are normalized to those of the progenitors, which are placed at the origin. The vertical bars in the diagram indicate the range in

σ_0 associated to each end-product, owing to projection effects. The figure shows that, in the isotropic one-component case (empty circles), if the parent galaxies satisfy the FJ relation, *the end-products generally have central velocity dispersion only marginally consistent with the FJ relation*, when its large observed scatter is considered (dotted lines in Fig. 7.5). In particular, the σ_0 of the remnant is *lower* than that predicted by the FJ relation itself for a given luminosity, in agreement with what found in Chapter 6 (see also NLC03a and NLC03b). Interestingly, this small deviation from the FJ relation is in the same direction as observed in many real BCGs (see, e.g., Malumuth & Kirshner 1985). If the parent galaxies are anisotropic, the corresponding end-products generally deviate more substantially from the FJ relation, again in the direction of too low central velocity dispersion. This could be interpreted as due to lower degree of global radial anisotropy in the remnants, with respect to their progenitors, since the presence of radial anisotropy contributes substantially to increase σ_0 , as we showed in Chapter 5 (see also NLC02). On the other hand, considering simulations with two-component galaxies, we find that in general the presence of the galactic DM halo has the effect of producing higher velocity dispersion in the end-products. Thus, the two-component end-products are found near the FJ relation (crosses in Fig. 7.5), again in accordance with the results of Chapter 6. As already noted, in some cases two-component remnants satisfying the FJ relations have in fact large values of the central velocity dispersion ($\sigma_0 \gtrsim 400 \text{ km s}^{-1}$), which seem not consistent with the observations (see however the discussion at the end of Section 7.6.1).

7.7 Multiple merging and the $M_{\text{BH}}\text{-}\sigma_0$ relation

As outlined in Chapter 1, a question naturally raised in the considered scenario is whether the $M_{\text{BH}}\text{-}\sigma_0$ relation is preserved by multiple dissipationless merging. Here we try to get some indications about the effects of multiple mergers on the $M_{\text{BH}}\text{-}\sigma_0$ relation, by using the results of our numerical simulations, though we do not explicitly take into account the presence of BHs in the galaxy models. This approach is justified on the basis of the reasoning presented in Section 6.5, where a similar analysis was carried out, in case of binary galaxy merging.

Thus, we simply assume that each of the five galaxies contains a BH, whose mass is related to the galaxy central velocity dispersion by equation (2.11), and the merger remnant contains a BH obtained by the merging of the BHs of the progenitors. As done in Section 6.5 (following CvA01), we consider two extreme situations for the BH mass addition: the case of *classical* combination of masses ($M_{\text{BH},1+2} = M_{\text{BH},1} + M_{\text{BH},2}$, with no emission of gravitational waves), and the case of *maximally efficient radiative merging of two non-rotating BHs* ($M_{\text{BH},1+2}^2 = M_{\text{BH},1}^2 + M_{\text{BH},2}^2$). Following this choice, in Fig. 7.6 we plot the central velocity dispersion of the mergers versus the mass of their central BH, in the case of classical (left panels) and maximally radiative (right panels) BH merging. In the diagrams the dashed and dotted lines correspond to the $M_{\text{BH}}\text{-}\sigma_0$ relation as given in equation (2.11) with $\alpha = 4$ and $\alpha = 5$, respectively. We note that, owing to the small range in galaxy stellar mass (and then BH mass) explored, the difference between the values of σ_0 predicted for these two values of the exponent are always smaller than the projection

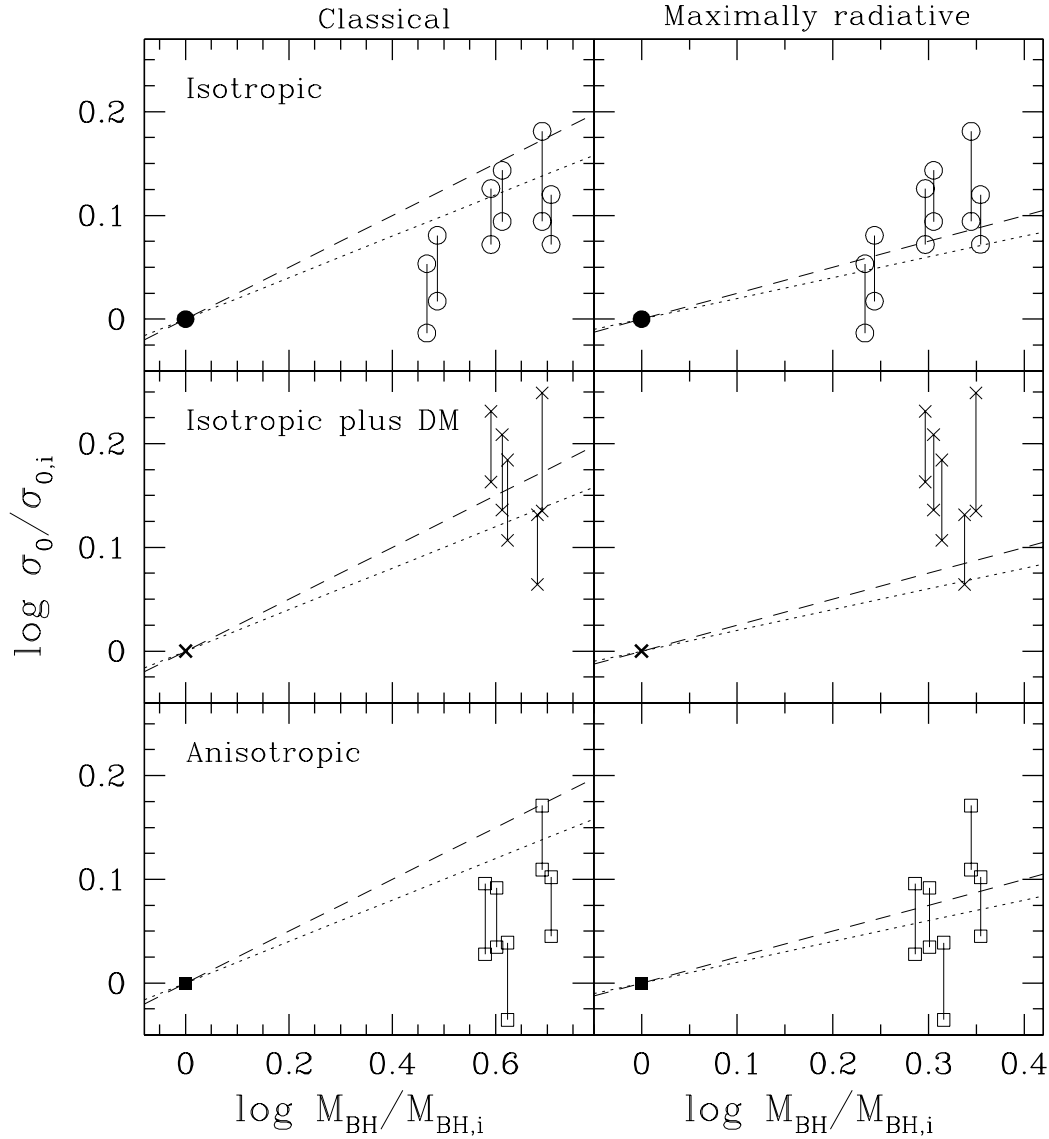


Figure 7.6: *Left panels:* galactic central velocity dispersion vs. BH mass for classical BH merging, in case of isotropic progenitors (upper panel), progenitors with DM halo (intermediate panel), and anisotropic progenitors (lower panel); $\sigma_{0,i}$ and $M_{\text{BH},i}$ are the central velocity dispersion and BH mass of the progenitors, respectively. The bars indicate the range spanned by projection effects. Dashed and dotted lines represent the $M_{\text{BH}}\text{-}\sigma_0$ relation for $\alpha = 4$ and $\alpha = 5$, respectively. *Right panels:* same data as in left panels, but for maximally radiative BH merging.

effects on σ_0 of the models (vertical bars in Fig. 7.6): for this reason, the following considerations about the comparison between the data and the $M_{\text{BH}}\text{-}\sigma_0$ relation are independent of the exact value of α . In addition, we note that also the scatter of the observed $M_{\text{BH}}\text{-}\sigma_0$ relation (actually not indicated in the diagram) is comparable in size with the separation between the dashed and dotted lines (see Section 2.4).

We start up considering the case of classical combination of BH masses (left panels in Fig. 7.6). It is apparent from the diagrams that, as well as in the case of the FJ relation (see previous Section), the properties of the progenitor galaxies are an influent factor in determining the effects of multiple merging on the $M_{\text{BH}}\text{-}\sigma_0$ relation. In particular, when the initial galaxies are without dark matter and isotropic (upper panel) the trend is that the merger remnant has σ_0 lower than that predicted by the $M_{\text{BH}}\text{-}\sigma_0$ relation; the situation is even worse if the initial galaxies are radially anisotropic (lower panel). On the contrary, in case of initial models with galactic DM halo (intermediate panel) the stellar central velocity dispersion is higher for given BH mass and the end-products are found closer to the observed relation, in accordance with what found in Section 6.5 in case of binary galaxy merging. The situation changes substantially if maximally radiative BH merging is considered (right panels in Fig. 7.6): in this case the BH mass does not increase linearly with the stellar mass and, as a consequence, the $M_{\text{BH}}\text{-}\sigma_0$ relation predicts lower σ_0 for a merger remnant of given luminosity, with respect to the classical case. Thus, in case of initial galaxies without galactic DM halo, both isotropic (upper panel) and anisotropic (lower panel), the end-products are found near the observed relation, while in case of initial models with dark halo (intermediate panel) the data deviate strongly from the $M_{\text{BH}}\text{-}\sigma_0$ relation, in the sense that the remnant has too high central velocity dispersion. Considering the presented results as a whole, we obtain a picture indicating that *the effects of multiple merging on the $M_{\text{BH}}\text{-}\sigma_0$ relation depend significantly on the properties of the progenitors and on the details of BH merging*. The observed slope of this relation is compatible with maximally radiative merging of one-component galaxies or classical merging of galaxies with dark halos, although in this latter case the values of σ_0 are sometimes larger than those observed in real galaxies (see discussion at the end of Section 7.6.1).

The results presented above about the effects of multiple merging on the $M_{\text{BH}}\text{-}\sigma_0$ relation are based on the assumption that the BHs of the merging galaxies remain in the remnant, leading of course to an oversimplified scenario. In fact, as already pointed out in Section 6.5, there are at least two basic mechanisms that could be effective in expelling the central BHs. The first is the slingshot effect: if a third galaxy is accreted by a merger remnant still hosting a BH binary, then the escape of one of the three BHs is expected (see, e.g., Milosavljevic & Merritt 2001, Yu 2002, Haehnelt & Kauffmann 2002, Volonteri, Haardt & Madau 2003). Clearly, this process could be particularly effective in the considered situation of multiple merging. We know from our simulations that in the studied galaxy system the multiple merger is expected to happen in few Gyrs (for example, in 2.3 Gyr, involving 5 galaxies), i.e., with time-scales hardly longer than that of BH merging. The second physical mechanism that could produce the ejection of the resulting BH is the so-called “kick-velocity” effect: if, in a gravitationally radiative BH merging, even a very small fraction of the mass of the BH binary is emitted *anisotropically*

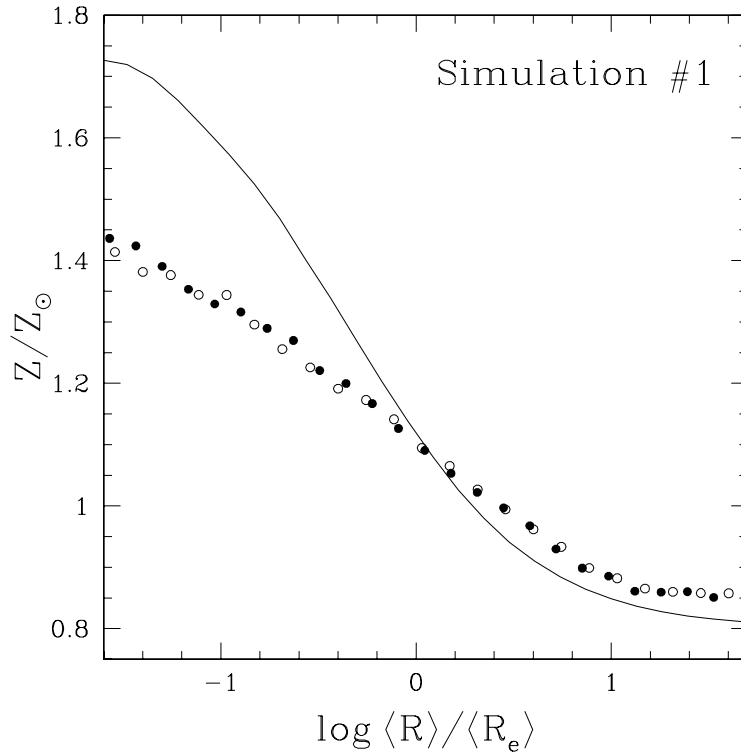


Figure 7.7: Projected metallicity versus circularized radius. Solid line: initial metallicity distribution of each progenitor galaxy. Solid and empty symbols: projections along the major and minor axis, respectively, for the end-product of the simulation #1.

as gravitational waves, the recoil due to linear momentum conservation is sufficient to expel the two merging BHs from the remnant (see, e.g., Flanagan & Hughes 1998, CvA01). We note that, in any case, a substantial amount of BH ejection during merging would necessarily lead to the violation of the observed linear relation between the mass of the central BH and the mass of the host bulge or galaxy (Magorrian et al. 1998).

7.8 Metallicity gradients

As it is well known, metallicity gradients are a common feature of elliptical galaxies (Peletier 1989, Carollo et al. 1993), and their robustness in the context of substantial merging was recognized early as an important constraint for scenarios of galaxy formation. For example, White (1980) found that the remnant of the merging of two equal mass galaxies has a metallicity gradient ~ 20 per cent smaller than its progenitors. This result suggested that in a scenario of (dissipationless) hierarchical merging the gradients could be erased in few subsequent mergers. It is interesting to extend these considerations to the case of multiple mergers like those analysed in this work, even if in the present case their constraining power is substantially reduced. In fact, BCGs normally reside at the center of clusters, where metal rich

intracluster medium flows (such as cooling flows) alter considerably the metallicity distribution.

From a dynamical point of view, the observed projected gradients correspond to phase-space projections of the intrinsic metallicity distribution of stars in their orbits. Ciotti, Stiavelli & Braccetti (1995) described a simple technique in principle able to derive the intrinsic metallicity distribution in the case of spherically symmetric galaxies. By adopting the same approach, in the initial conditions of the one-component simulations we assigned to each particle a metallicity value as a function of Q given by

$$\frac{Z}{Z_{\odot}} = 1.3 \frac{Q}{\Psi_*(0)} + 0.8, \quad (7.5)$$

where Z_{\odot} is the solar metallicity and $\Psi_*(0)$ the central relative potential of each progenitor (see Section 3.1). This choice corresponds to a projected central metallicity $Z(R=0) \simeq 2Z_{\odot}$. In our investigation we assume that the metallicity of each particle remains constant during the dynamical evolution of the system. We quantified the projected metallicity gradients, in both the initial galaxies and the end-products, by measuring the “center-to-edge metallicity difference” as defined by White (1980):

$$\Delta Z = \frac{\langle Z \rangle_{\text{in}} - \langle Z \rangle_{\text{out}}}{\langle Z \rangle}, \quad (7.6)$$

where $\langle Z \rangle$, $\langle Z \rangle_{\text{in}}$, and $\langle Z \rangle_{\text{out}}$ are the metallicities averaged over the whole distribution, inside the projected radius enclosing 1/3 of the total mass, and outside the projected radius enclosing 2/3 of the total mass, respectively. We measured ΔZ of the remnant of mergers of isotropic and anisotropic one-component progenitors, considering the projections along the three principal axes. In all the cases we found that it is significantly lower in the end-products than in the progenitors: the decrease in ΔZ is in the range 30 – 60% of the initial value. This result is presented with an example in Fig. 7.7, where we plot the projected metallicity as a function of the circularized radius for the end-product of the merging of 4 galaxies (simulation #1), and, for comparison, for its progenitors. On the basis of the described results, we can conclude that in case of multiple merging the observed reduction of the metallicity gradient is consistent with the repeated application of “White’s 20% rule”. However, this is not necessarily at odds with observations, as Carollo et al. (1993) find that the correlation between mass and the metallicity gradient fails for high mass Es, indicating that in some cases very massive galaxies have smaller gradient than less luminous Es. In addition, if the merging galaxies contain a substantial gas fraction, the metallicity gradient could be restored by a significant star formation event.

7.9 Discussion and conclusions

The group of five Es in the core of the galaxy cluster C0337-2252 is a concrete example of candidate for galactic cannibalism, observed in the phase before galaxy merging. In this Chapter we explored, with the aid of N-body simulations based on the known phase-space information, the hypothesis that this system will evolve,

as a consequence of galactic mergers, into a giant elliptical or a cD galaxy. We summarize below the main results.

- In all of the explored cases at least 3 galaxies merge before $z = 0$. For some values of the parameters all the 5 galaxies are involved in the merging. The number of merging galaxies depends on the cluster structure and, in some cases, also on the particular realization of the initial condition. The driving mechanism of the merging process is actually the dynamical friction of the galaxies against the diffuse cluster DM. If the live halo is substituted by a fixed potential the number of merging is drastically reduced.
- The merger remnant will be similar in its main structural and dynamical properties to a real BCG. Its SB profile is quite well fitted with the de Vaucouleurs law up to $\sim 10\langle R \rangle_e$, with no evidence of the diffuse extended profile typical of cD galaxies.
- The merging end-product is found near the FP relation, under the hypothesis that the five galaxies initially satisfy the FP relation. On the other hand, its central velocity dispersion is expected to be only marginally consistent with the FJ relation (with σ_0 lower than predicted by the FJ relation), in agreement with the results of Chapter 6, and also with the central velocity dispersion measured in many BCGs.
- If the initial galaxies are assumed radially anisotropic, the corresponding end-products are found significantly outside the FP. This is mostly due to quite low values of their projected central velocity dispersion, as indicated by a substantial violation of the FJ relation. A possible interpretation is that the multiple merger remnants are more globally isotropic than their radially anisotropic progenitors.
- The main characteristics of the final stellar system, in case of progenitors with associated DM halos, are similar to those of the one-component remnant. We note only that the merger remnants of models with galactic DM halo in general are found closer to the FJ relation, having quite high central velocity dispersion.
- The behavior of this multiple merging with respect to the $M_{\text{BH}}\text{-}\sigma_0$ relation depends on both the properties of the progenitor galaxies and the details of BH merging. Assuming that each galaxy initially hosts at its center a supermassive BH, whose mass follows the observed $M_{\text{BH}}\text{-}\sigma_0$ relation, the remnant is expected to satisfy the same relation between BH mass and galaxy central velocity dispersion only in special cases.
- The metallicity gradient in the remnant is 30 – 60% lower than in the initial galaxies. This result is consistent with an extension of the results of binary merging obtained by White (1980), and not at variance with Carollo et al. (1993) who find a range of metallicity gradient in the most massive Es.

From a theoretical point of view, it is well known that galactic cannibalism can be an effective mechanism in the formation of BCGs. On the other hand, just

circumstantial evidence of this process comes from the observations, and only of the phase after merging (for example, BCGs with multiple nuclei). The results presented in this Chapter suggest that *the observed system of five galaxy in the galaxy cluster C0337-2252 is actually a BCG in formation in the phase before merging*. Thus, our study confirms, with a practical example, that galactic cannibalism is a real mechanism for the formation of BCGs. The remnant is expected to be characterized by several properties of the observed giant Es. It will have a $R^{1/4}$ SB profile over a large radial range, without indication of the diffuse extended luminous halo typical of cDs. In addition, under reasonable hypotheses on the properties of the progenitors, it is expected to satisfy the very tight FP relation, and to have central velocity dispersion comparable with that of BCGs. Some problems arise when considering the very tight $M_{\text{BH}}\text{-}\sigma_0$ relation, in this scenario of multiple merging. Also as expected from theoretical considerations, it is difficult to reconcile the existence of this relation with a major role of multiple merging in galaxy formation, though our analysis show that under certain assumptions on the properties of the progenitors and on the BH merging, the remnant is expected to be close to the observed relation.

Comparing the results of our *multiple merging* simulations with those of Chapter 6, where we considered hierarchies of *binary* galaxy merging, we find good agreement in the main structural and dynamical properties of the remnants. However, we would like to stress that the interpretation of the results is quite different in the two cases. In Chapter 6 we showed that it is unlikely that *dissipationless* galaxy merging is the dominant mechanism for the formation of normal Es, as it fails to reproduce some of their observed scaling relations over a large range in luminosity. The results of the present Chapter indicate that many properties of the (peculiar) brightest Es observed in the center of galaxy clusters are reproduced by dissipationless merging of *a few* luminous Es. In particular, the numerical simulations of both Chapter 6 and this Chapter indicate that *few* merging events are compatible with the existence of the observed *thin* FP of Es, though the remnants have in general lower central velocity dispersion and larger effective radius, with respect to real Es. Remarkably, the BCGs do follow quite closely the FP, and, on the other hand, many of them have lower σ_0 and mean effective SB than predicted by the FJ and the radius-luminosity relation of normal Es, respectively (see, e.g., Oegerle & Hoessel 1991). In addition, also the peculiar behavior of the most massive Es with respect to the correlation between mass and the metallicity gradient seems to be compatible with the considered mechanism of formation. However, as already pointed out, this quite successful scenario is unable to reproduce the diffuse low luminosity halo of cD galaxies, which are a substantial fraction of BCGs. We speculate that the interaction of a central massive galaxies (like that produced in the considered multiple merging) with smaller and lower density galaxies could be responsible of its formation. This hypothesis needs further numerical simulations to be verified.

8. Conclusions

In the present work we considered the implications of the scaling relations of elliptical galaxies from the point of view of stellar dynamics. With this approach we obtained new, interesting results on the formation and evolution history of Es. In particular, we explored the interplay between the FP and the radial orbital anisotropy of Es, also considering the effects of radial orbit instability. In addition, we investigated what could be the role of dissipationless merging in the formation history of Es. Finally, we studied, with a concrete, specific example, the process of formation of BCGs, as a consequence of the dynamical evolution of galaxies in clusters.

For what concerns the first point, we showed that the processes that lead to the formation of Es are not required to produce systems with fine tuned radial orbital anisotropy. In fact, *the observed FP thickness results consistent with whatever spread in radial orbital anisotropy, when the effect of radial orbit instability is taken into account*. In other words, one of the problems related to the existence of the FP was how its small thickness could be reconciled with the expected spread in radial orbital anisotropy (and then in σ_0) of Es (de Zeeuw & Franx 1991). Our numerical simulations indicate that radial orbit instability actually limits the effective amount of possible spread in anisotropy and contributes to maintain the FP thinness. Thus, even if the mechanism responsible for elliptical galaxy formation (whatever it is) produced galaxies with a large spread in orbital anisotropy, this spread would be early reduced as a consequence of instability.

The results of our study on radial orbital anisotropy are also very interesting when interpreted from the point of view of the FP tilt. In particular, they provide evidence that the tilt cannot be due to a systematic increase of radial orbital anisotropy with galaxy luminosity. In other words, *purely dynamical non-homology is not sufficient to explain the FP tilt*. Clearly, this is just another consequence of the limits put by radial orbit instability on the amount of radial orbital anisotropy that Es can sustain. Therefore, our theoretical approach leads to the conclusion that Es are a dynamical homologous family of stellar systems, in accordance with observational findings (see, e.g., Gerhard et al. 2001).

The failure to reproduce the FP tilt with structurally homologous, but dynamically non-homologous galaxy models gives interesting indications when considering a *dissipationless* merging scenario for elliptical galaxy formation. In this case, by definition, neither gas dissipation nor star formation are involved in the process, and the stellar mass-to-light ratio Υ_* is constant during the merging

hierarchy. Therefore, the FP tilt (in other words, the dependence of the ratio Υ_*/K_V on L_B as given in equation 5.3) can be ascribed only to K_V decreasing with L_B , i.e., to structural and/or dynamical non-homology effects. Thus, the fact that the FP tilt cannot be explained in terms of purely dynamical non-homology could be interpreted as a first indication that a dissipationless merging scenario could be unable to reproduce the FP of Es. However, we recall here that this is just a qualitative indication, because galaxy merging, besides dynamical non-homology, is expected to introduce also structural non-homology effects. For this reason, the problem of the effect of galaxy merging on the FP has required a direct exploration.

Therefore, we performed numerical simulations of dissipationless merging hierarchies, considering both accretion and major merging, also exploring the effects of the presence of galactic DM halos and orbital angular momentum in the galaxy encounters. As a general result, we found that this scenario is unable to form stellar systems with the properties of the observed Es, as apparent by a substantial violation of their scaling laws (such as the FP, the FJ, and the Kormendy relations). In addition, our simulations show that the exact behavior of the end-products of the merging hierarchy, with respect to the scaling relations, is quite dependent on the details of the merging history (especially on the mass ratio between the objects involved and on the amount of orbital angular momentum). This result, when interpreted in the general context of structure formation, is in accordance to the claim that the inner density profile of DM halos depends on the mass function of their constituents subunits (Subramanian, Cen & Ostriker 2000; Ricotti 2002). However, we would like to stress that, in spite of these differences among the explored galaxy merging hierarchies, our results seem to rule out a dissipationless merging scenario, because, in any case, it fails to reproduce at least one of the global scaling laws of Es.

In particular, we find that *whatever dissipationless merging hierarchy results unable to reproduce the FJ relation*: the central velocity dispersion does not increase with galaxy luminosity as instead observed in real Es. This important result can be qualitatively interpreted as a combination of two simple theoretical considerations. On the one hand, the virial velocity dispersion σ_V is expected to be almost unaffected by dissipationless merging (see equations 6.1 and 6.3). On the other hand, as discussed above, radial orbit instability limits the amount of dynamical non-homology, that is one of the main factor in principle able to produce a large spread in σ_0 for fixed σ_V (see the results of Chapter 5).

Remarkably, *most of the merger remnants are placed rather close to the FP*. Only the end-products of the head-on accretion hierarchy deviate substantially from the edge-on FP, with a trend in k_1 - k_3 opposite with respect to what observed for real Es. However, this quite surprising reproduction of the FP, obtained for most of the models, could be somewhat misleading. In fact, *these merger remnants, though satisfying the tight edge-on FP relation, are definitely not similar in their structural and dynamical properties to the observed Es*. Besides having too low σ_0 , as outlined above, they also violate the Kormendy relation, having systematically too low surface brightness, with respect to what expected for their luminosity. This

is reflected also by the very large displacement produced by galaxy merging in the face-on FP, which is however characterized by a small constraining power, due to its large intrinsic dispersion. Rather curiously, the deviations from the FJ and the Kormendy relations compensate, with the effect that the remnants do follow quite well the edge-on FP, even if their properties differ substantially from those of real Es. Anyway, from this picture we must clearly conclude that dissipationless merging is unable to form Es with all their observed properties. Thus, we would like to stress the importance of considering also other scaling relations, besides the edge-on FP, when trying to constrain a galaxy formation scenario. In fact, other similar studies on dissipationless merging were unable to detect the failure of such a scenario to reproduce the scaling laws, because they considered only the FP, and few steps of the merging hierarchy (see, e.g., Dantas et al. 2003, Gonzalez-Garcia & van Albada 2003).

A strictly related result is our finding that a dissipationless merging hierarchy fails to reproduce either the $M_{\text{BH}}\text{-}\sigma_0$ relation or the Magorrian relation. In practice, we showed that the exact behavior of the remnants with respect to these correlations is dependent on the details of BH merging, which is a quite complex physical process, currently studied in detail by several authors (see, e.g., Yu 2002, Merritt & Ekers 2002; Hughes & Blandford 2002). In the present work, we introduce the problem of BH merging adopting the simple, but conservative approach suggested by Ciotti & van Albada (2001). Even in this simplified scenario, our results are actually quite robust, indicating that *it is very difficult to reconcile substantial dissipationless merging with the existence of both the $M_{\text{BH}}\text{-}\sigma_0$ and the Magorrian relations*. In addition, qualitative considerations indicate that a more detailed treatment of BH merging could even strengthen our claim that dissipationless merging cannot reproduce the correlations between M_{BH} and the properties of the host bulge or galaxy. In fact, in a scenario in which supermassive BHs accrete most of their mass via BH merging, at least two mechanism are expected to be effective in expelling the BHs from the galaxies. In particular, in case of subsequent galaxy mergers (with characteristic time shorter than the BH merging timescale¹¹) the lightest BH would be expelled as a consequence of the slingshot effect. Furthermore, the recoil due to anisotropic emission of gravitational waves, in radiative BH merging, would be sufficient to eject the merging BH binary from the remnant. Clearly, both these mechanisms would produce a large scatter in the $M_{\text{BH}}\text{-}\sigma_0$ relation, and would also lead to a systematic deviation from the Magorrian relation.

Finally, we directly investigated the dynamical evolution of group of five Es in the core of the galaxy cluster C0337-2522. Our study, based on ESO-VLT data, suggested that this system of galaxy is actually going to form a BCG in few Gyrs via multiple merging (see also Nipoti et al. 2003c). This results is relevant because indicates that *the five Es in C0337-2522 represent a rare case of BCG formation through galactic cannibalism observed in the phase before merging*. Our finding

¹¹The BH merging timescale depends strongly on both the BH mass ratio and the properties of the host galaxy. However, at least in some cases, it can be very long, even exceeding the Hubble time (Yu 2002). On the other hand, our *multiple merging* simulations predict a time between subsequent merging events of about 1 Gyr, or shorter (see Chapter 7).

gives further support to the theory that multiple merging is a viable mechanism of formation for the superluminous Es observed in the center of galaxy clusters. In addition, observing the early stage of BCG formation is very interesting also because we can know directly the properties of the progenitors, which, in the case of C0337-2522, are gas poor early-type galaxies. Thus, it is apparent that the core of C0337-2522 is hosting a multiple dissipationless merging event. As already pointed out, other cases of merging between gas poor galaxies in cluster are known (see, e.g., van Dokkum 1999), so we conclude that the case of C0337-2522 is not exotic.

The situation could seem somewhat puzzling. On the one hand, we know from observations that dissipationless merging is a process not completely unusual in nature, while, on the other hand, as discussed above, our results indicate that it is not a viable mechanism to form Es. A few considerations are needed to explain this apparent discrepancy. As a first point, we recall that our investigation leads to the conclusion that Es cannot be the end-products of *several* dissipationless merging events. On the contrary, on the basis of our results, an elliptical galaxy, which during its lifetime experiences one or two merging episodes, is expected to remain near the observed scaling laws. In fact, the violation of the scaling relations becomes evident when many steps of the merging hierarchy are considered, while are negligible in the first steps. Thus, *few*, rare merging episodes are not excluded, even in the dynamical evolution of normal Es.

On the other hand, it is important to recall that BCGs are different from normal Es in many respects, not only for their huge luminosity. In particular, BCGs (both giant Es and cDs), though following quite closely the FP (Oegerle & Hoessel 1991), generally violate (even if not dramatically) the FJ and the Kormendy relations, having too low σ_0 and mean effective surface brightness, respectively (Malumuth & Kirshner 1981, 1985). Interestingly, these deviations are in the same direction as those found for the remnants of dissipationless merging. Thus, the picture deriving from our study on merging hierarchies and galactic cannibalism indicates that *dissipationless merging does not work as dominant mechanism for the formation of the normal Es, while it seems reliable that BCGs are the end-product of multiple merging involving a few galaxies*, for example luminous Es as in the concrete case of the cluster C0337-2522. This is in accordance with other observational tracers of mergers found in a substantial fraction of BCGs, such as multiple nuclei or shallow inner surface brightness profiles (see, e.g., Laine et al. 2003)

Of course, a fundamental question still remains without answer: how did normal Es form? If the dissipationless merging hypothesis has to be excluded for the reasons presented above, possible solutions are a monolithic scenario, or a hierarchical merging scenario in which gas dissipation plays a major role. Clearly, the latter solution would be preferable, because it could be reconciled with the currently adopted Λ CDM cosmological model (see, e.g., Cole et al. 2000 and references therein). Interestingly, gas dissipation would have the effect to modify the end-products of the considered merger hierarchies, making them more similar to real Es. In particular, if the merging galaxies contain non negligible amount of gas, the effect of dissipation would be to shrink the density distribution of the remnant, which

would be characterized by larger σ_0 and smaller $\langle R \rangle_e$. However, it is well known that too much gas dissipation and star formation at low redshift is excluded, because Es are gas-poor systems with old stellar populations. For this reason, our results suggest that if merging had a role in the formation of Es, it was at quite high redshift, and with a significant amount of associated gas dissipation and star formation (see, e.g., Mihos & Hernquist 1994, Meza et al. 2003 and reference therein).

In addition, in this gas-rich merging scenario, in order to preserve the observed Magorrian relation, a fraction of the dissipating gas must be accreted by the central BH, producing QSO activity. This speculation suggests that the cosmic history of QSO activity and the galaxy merging history must be strongly coupled. Observations indicate that the comoving space density of QSOs peaks at $z \sim 2$ (e.g., Hartwick & Schade 1990). Thus, the picture above would also be in accordance with the constraints posed by the old age of the stellar populations of Es.

Appendix

A.1 Numerical realization of the Osipkov-Merritt models

Monte Carlo methods allow to construct a numerical realization of a given distribution function (DF) in phase-space $f(\mathbf{x}, \mathbf{v})$, using N -point particle coordinates $(\mathbf{x}_i, \mathbf{v}_i)$ as random variables having $f(\mathbf{x}_i, \mathbf{v}_i)$ as probability distribution. To that purpose, the basic, general algorithm is provided by the von Neumann rejection method (see, e.g., Aarseth, Henon & Wielen 1974), in which a realization of any given density probability function is constructed starting from the numerical generation of random uniform deviates.

As described in Chapter 3, the models chosen as initial conditions in the present work are spherically symmetric. Thus, for simplicity we assign the phase-space variables in spherical coordinates, (r, ϑ, φ) for positions, and $(v_r, v_\vartheta, v_\varphi)$ for velocities. The DF of the models can be considered in the form $f(\mathbf{x}, \mathbf{v}) = \rho(r) \times g(v_r, v_t|r)$, where $v_t = \sqrt{v_\vartheta^2 + v_\varphi^2}$. In this approach, the space coordinates are first assigned according to the given density function $\rho(r)$ and then, for each radial position r_i , the velocity coordinates are assigned as independent random variables, consistently with the associated DF. For a spherically symmetric density distribution $\rho(r)$, the mass within a radius r is given by

$$M(r) = 4\pi \int_0^r \rho(r') r'^2 dr'. \quad (\text{A.1})$$

In particular, for spherical γ -models, $r(M)$ can be written explicitly and the Monte Carlo procedure for the numerical representation of the radial profile simplifies noticeably. The inversion relation $r = r(u)$, where $u(r) = M(r)/M$ and $M = \lim_{r \rightarrow \infty} M(r)$ is the total mass, is available in analytical form. Thus, the radial coordinate $r_i = r(u_i)$ can be assigned, for each sorted u_i value, using a random uniform deviate variable $0 < u < 1$. Alternatively, in cases where low-noise initial conditions are needed, the quiet start method is usually preferred (Sellwood 1983). In this approach, non-random radial positions are sampled by fixing the uniform grid

$$u_i = u_{\max}/N_c, \quad i = 1, 2, \dots, N_c, \quad (\text{A.2})$$

where typical values $N_c = 256$, $u_{\max} = 0.999$ suffice to assure acceptable representation of both the core and the halo regions. In this way it is possible to reproduce the particle potential on a prefixed grid $r_i = r(u_i)$ up to the maximum

sampled radius $r_{\max} = r(u_{\max})$. Finally, for each particle radius r_i , angular variables are assigned by sorting φ as uniform deviate in $[0, 2\pi]$ and $\cos\vartheta$ as uniform deviate in $[-1, 1]$.

To assign the velocity coordinates, one takes advantage of the particular form of the DF of the Osipkov-Merritt models $f = f(Q)$ (see equation 3.5). In practice, we introduce the dimensionless vector of components (u_1, u_2, u_3) , related to $(v_r, v_\vartheta, v_\varphi)$ by

$$v_r = \sqrt{2\Psi_T}u_1, \quad v_\vartheta = \frac{\sqrt{2\Psi_T}}{\nu_a}u_2, \quad v_\varphi = \frac{\sqrt{2\Psi_T}}{\nu_a}u_3, \quad (\text{A.3})$$

where

$$\nu_a = \sqrt{1 + \frac{r^2}{r_a^2}}. \quad (\text{A.4})$$

We recall here that Ψ_T is the total relative potential per unit mass, and r_a is the anisotropy radius (see Section 3.1). With the parameterization above, Q can be written as $Q = (1 - u^2)\Psi_T$. Thus, the DF $f(Q)$ with $Q = (1 - u^2)\Psi_T$ depends only on the vector modulus $u = \sqrt{u_1^2 + u_2^2 + u_3^2}$, with $0 < u < 1$. The corresponding statistical sampling in velocity space follows then the computational steps:

- the DF $f(Q)$ is first pre-computed using a numerical integration on a fine grid Q_j , $j = 1, 2, \dots, N_g$;
- for each given particle radial position r_i , corresponding to a total relative potential $\Psi_T(r_i)$, the i -th triplet $(u_1, u_2, u_3)_i$ of random uniform deviates with modulus $u_i < 1$ is chosen, and the values $Q_i = (1 - u_i^2)\Psi_T(r_i)$ and $f(Q_i)$ are computed;
- the rejection procedure is then activated: by choosing the random uniform deviate w as a test probability variable, the triplet $(u_1, u_2, u_3)_i$ of uniform deviates is accepted if $w f_{\max,i} < f(Q_i)$, where $f_{\max,i} = f[\Psi_T(r_i)]$ is the maximum value of f for a particle at r_i . If the condition above is satisfied, the physical variables $(v_r, v_\vartheta, v_\varphi)$, related to the (u_1, u_2, u_3) coordinates through equations (A.3), can be recovered.

Finally, the phase-space components so obtained are converted into Cartesian coordinates, which are adopted in the N -body codes used in the present work (see Chapter 4).

A.2 Diagnostics of the numerical simulations end-products

For the purpose of our work, we need to determine the structural and kinematic properties of the end-products of the numerical simulations. In addition, we want to compare their “observational” properties with those of real galaxies. Here we summarize the techniques used to derive the intrinsic and projected quantities, starting from the set of positions and velocities output of the simulations.

As a preliminary, we define *end-product* of a given simulation, as the sub-set of (stellar and dark) particles which initially belonged to the considered galaxy models, and are *bound* at the end¹² of the simulation itself. In other words, the i -th particle is selected for further analysis if its energy per unit mass satisfies

$$E_i = \frac{1}{2}|\mathbf{v}_i|^2 + \Phi(\mathbf{x}_i) \leq 0, \quad (\text{A.5})$$

where \mathbf{x}_i and \mathbf{v}_i are the position and velocity of the i -th particle in any inertial reference system and $\Phi(\mathbf{x}) < 0$ is the computed particle potential.

Intrinsic properties

We consider here an end-product made up of N bound particles, with total mass M_{tot} . As a first step we calculate the phase-space coordinates of the *center of mass* of the system

$$\mathbf{x}_{\text{cm}} = \frac{1}{M_{\text{tot}}} \sum_{i=1}^N m_i \mathbf{x}_i, \quad (\text{A.6})$$

and

$$\mathbf{v}_{\text{cm}} = \frac{1}{M_{\text{tot}}} \sum_{i=1}^N m_i \mathbf{v}_i. \quad (\text{A.7})$$

In the following we consider positions and velocities of the particles relative to the center of mass. In addition, we assume that all the particles have the same mass, as it happens in all our simulations.

The *virial velocity dispersion* of the system is calculated simply by applying the definition and summing over all the particles:

$$\sigma_V = \sqrt{\frac{1}{N} \sum_{i=1}^N |\mathbf{v}_i|^2}. \quad (\text{A.8})$$

We also compute by direct summation the *total angular momentum* of the system, given by

$$\mathbf{L}_{\text{tot}} = \sum_{i=1}^N m_i \mathbf{v}_i \times \mathbf{r}_i. \quad (\text{A.9})$$

For the analysis of the three-dimensional shape of the system, we consider the *intrinsic ellipticities* associated with its inertia ellipsoid. These quantities are a measure of the departure from spherical symmetry of a self-gravitating system and

¹²Clearly, the definition of the time of end of a simulation depends on the purpose of the simulation and on the physical process under investigation. In any case, in all the simulations considered in this work, at the final time the large scale relaxation processes in the end-products can be considered almost completed, as can be checked by a nearly constant virial ratio (see tests in Section 4.4).

are particularly useful for the stability analysis (see Chapter 5). Thus, for the end-product of each numerical simulation we compute the inertia tensor $I_{ij} = \sum_k x_i^{(k)} x_j^{(k)}$ associated with the density distribution of interest (i.e., stars or halo). Following Meza & Zamorano (1997), the sum is extended over all the particles inside r_{70} , the radius of the sphere centered on the center of mass of the galaxy and enclosing the 70% of the total mass. The inertia tensor is diagonalized and the ratios of the square root of its eigenvalues are used to obtain a first estimate of the ellipticities of the density distribution, according to the standard definition $1 - b_{70}/a_{70}$ and $1 - c_{70}/a_{70}$. The orthogonal matrix corresponding to the diagonalization is also obtained, and the density distribution is rotated accordingly. This procedure is then applied iteratively to the ellipsoid characterized by $a = r_{70}$, and intermediate and minor axes obtained from the ellipticities computed at each stage, up to convergence at some prescribed accuracy level of the ellipticities.

The end-products of the simulations considered in the present work are expected to be very inhomogeneous systems and to deviate significantly from spherical symmetry. We take into account these characteristics when deriving their *angle-averaged density profile*. In particular, we measure the density by considering a logarithmic radial sampling and counting the particles within ellipsoidal shells. We assume that these shells have *constant* ellipticities, given by $1 - b_{70}/a_{70}$ and $1 - c_{70}/a_{70}$. When the angle-averaged density distribution is determined, we compute r_M the *angle-averaged half-mass radius*, defined as

$$r_M \equiv (a_M b_M c_M)^{1/3}, \quad (\text{A.10})$$

where (a_M, b_M, c_M) are the semi-axes of the ellipsoid enclosing half of the total mass of the system. In a similar way we calculate any $\langle r \rangle_x \equiv (a_x b_x c_x)^{1/3}$, i.e., the angle-averaged radius of the ellipsoid enclosing a fraction $x/100$ of the total mass. Of particular interest are $\langle r \rangle_{10}$, and $\langle r \rangle_{90}$, which allow to estimate the dimension of the core and the total extension of the system, respectively. Clearly, with this notation $r_M = \langle r \rangle_{50}$.

Projected properties

In order to convert the intrinsic galaxy properties, as derived from numerical simulations, into projected quantities having “observational” relevance, we calculate the following variables only for the *stellar* component: the isophotal ellipticity ϵ , the circularized effective radius $\langle R \rangle_e$, the circularized surface brightness profile, the mean effective surface brightness $\langle I \rangle_e$, and the central velocity dispersion σ_0 .

The line-of-sight direction is fixed by the arbitrary choice of ϑ and φ , the two angles of spherical coordinates, expressed in the reference frame where the inertia ellipsoid is diagonal. We apply to the system the rotation matrix $\mathcal{R} = \mathcal{R}_2(\vartheta)\mathcal{R}_3(\varphi)$, where

$$\mathcal{R}_3(\varphi) = \begin{bmatrix} \cos\varphi & \sin\varphi & 0 \\ -\sin\varphi & \cos\varphi & 0 \\ 0 & 0 & 1 \end{bmatrix}, \quad (\text{A.11})$$

$$\mathcal{R}_2(\vartheta) = \begin{bmatrix} \cos\vartheta & 0 & -\sin\vartheta \\ 0 & 1 & 0 \\ \sin\vartheta & 0 & \cos\vartheta \end{bmatrix}. \quad (\text{A.12})$$

In this coordinate system, the line-of-sight direction coincides with the z axis, while (x, y) is the projection plane. Thus, the reference system for the observational quantities is given by the three coordinates of the center of mass x_{cm} , y_{cm} , and $v_{z,\text{cm}}$.

In our treatment we always assume that the stellar mass-to-light ratio is independent of the position. Thus, we can simply convert projected mass into luminosity modulo the free parameter $\Upsilon_* = M_*/L_{\text{B}}$, where M_* and L_{B} are the total stellar mass and Blue luminosity of the end-product, respectively. The isophotal axis ratio b/a and the associated *ellipticity* $\epsilon = 1 - b/a$ in the projection plane are determined by using a two-dimensional version of the iterative scheme described above, where now only particles with projected radius smaller than R_{70} (the projected radius of the circumference enclosing $0.7M_*$) are considered in the first step of the computation of the projected inertia tensor.

The *surface brightness profile* is obtained in analogy with the derivation of the density profile. We adopt a logarithmic radial sampling and concentric ellipses of *constant* ellipticity, fixed at the value corresponding to the isophote enclosing 70% of the total luminosity. Thus, also the semi-axes a_e and b_e , of the effective isophote (enclosing half of the total luminosity) are determined under the assumption that the ellipticity of the projected density is constant. Finally, the *circularized effective radius* is obtained:

$$\langle R \rangle_e \equiv \sqrt{a_e b_e} = a_e \sqrt{1 - \epsilon}. \quad (\text{A.13})$$

The *mean effective surface brightness* $\langle I \rangle_e \equiv L_{\text{B}}/2\pi\langle R \rangle_e^2$ follows directly from the knowledge of $\langle R \rangle_e$.

The projected *central velocity dispersion* σ_0 is computed by restricting to the central ellipse corresponding to a circularized radius $\langle R \rangle_e/d$, where d is a dimensionless parameter. Thus, we use

$$\sigma_0 = \sqrt{\frac{1}{N_0} \sum_{i=1}^{N_0} (v_{z_i} - \bar{v}_z)^2}, \quad (\text{A.14})$$

where N_0 is the number of stellar particles in the projected central ellipse of semi-axes a_e/d and b_e/d , v_{z_i} is the line-of-sight velocity of the i -th particle, and \bar{v}_z is the mean velocity integrated along the line-of-sight. In most of the present work we adopt $d = 8$, which is the standard value used in the observations of low redshift galaxies (see, e.g., JFK96). Note however that the results presented in Chapter 7 are obtained with $d = 4$, that we consider a better choice in that particular context (see Section 7.6.1). In addition, in Section 5.2 we discuss the effects, on the results of Chapter 5, of choosing $d = 4$ or $d = 8$.

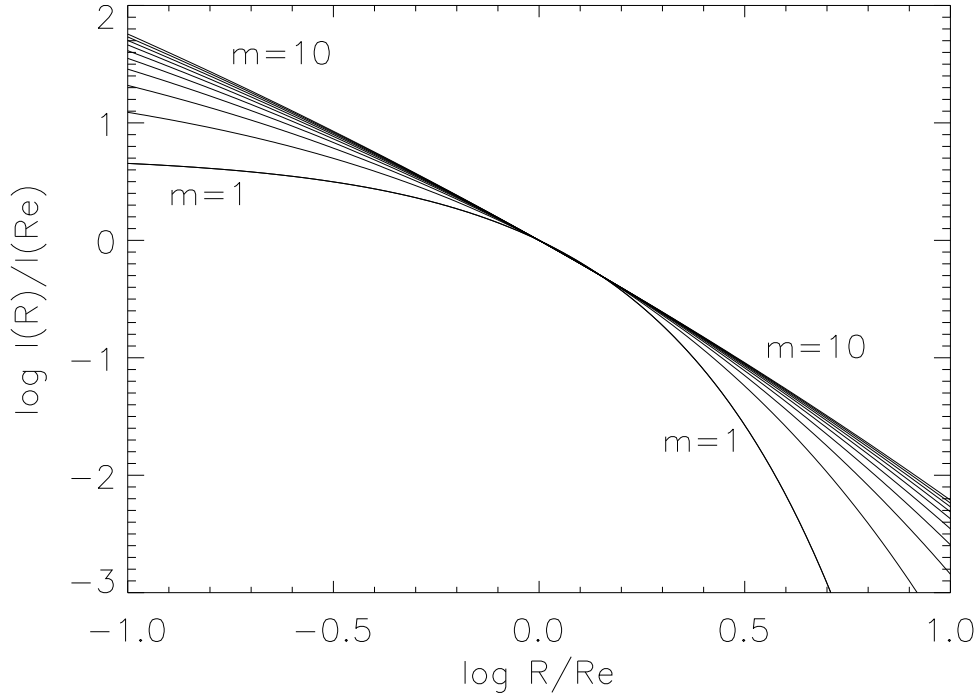


Figure A.1: Sersic (1968) $R^{1/m}$ profiles for $m = 1, 2, \dots, 10$.

A.3 Surface brightness profiles fitting

To fit the circularized surface brightness profiles of the galaxy models we use the Sersic (1968) $R^{1/m}$ law, defined as

$$I(R) = I_0 \exp \left[-b(m) \left(\frac{R}{R_e} \right)^{1/m} \right], \quad (\text{A.15})$$

where R_e is the effective radius, $I_0 = I(0)$ is the central surface brightness, m is a positive real number, and $b(m) \sim 2m - 1/3 + 4/405m$. The total luminosity is given by

$$L = I_0 R_e^2 \frac{2\pi m}{b^{2m}} \Gamma(2m), \quad (\text{A.16})$$

where Γ is the complete gamma function (Ciotti & Bertin 1999). The Sersic profile can be considered a generalization of the well known de Vaucouleurs (1948) $R^{1/4}$ law, which is obtained from equation (A.15), when adopting $m = 4$. The parameter m characterizes the shape of the profile. This is apparent from the diagram in Fig. A.1, where we plot $I(R)$, normalized to $I(R_e)$, as a function of the radius, for $m = 1, 2, \dots, 10$. A radial range $0.1 \lesssim R/R_e \lesssim 10$ is considered. At radii much larger than R_e , the luminosity profile is steeper for smaller values of m . The opposite

happens for $R/R_e \ll 1$. Note that we assume that the total luminosity, given in equation (A.16) above, is the same for all values of m .

For the fitting procedure, we follow the scheme described in Bertin et al. (2002), who fit observational data. The best-fitting parameters are obtained by minimizing the function

$$\chi^2 = \sum_{i=1}^N \frac{[\mu(R_i) - \mu_{\text{fit}}(R_i)]^2}{\sigma^2(R_i)(N - N_{\text{par}})}, \quad (\text{A.17})$$

where $\mu = -2.5\log I$ is the circularized surface brightness profile of the N -body system, N is the number of considered bins, σ is the dispersion due to the finite number of particles in each bin, and N_{par} is the number of free parameters in the fitting function μ_{fit} .

Besides the χ^2 function, other useful estimates of the quality of the fit are the average residuals between the data and the fits

$$\langle \Delta\mu \rangle \equiv \sqrt{\sum_{i=1}^N \frac{[\mu(R_i) - \mu_{\text{fit}}(R_i)]^2}{N}}, \quad (\text{A.18})$$

and the maximum deviation

$$(\Delta\mu)_{\text{max}} \equiv \max_{i=1, N} |\mu(R_i) - \mu_{\text{fit}}(R_i)|. \quad (\text{A.19})$$

For the purpose of the present work, the main goal of the luminosity profile fitting is the comparison with the slope of the projected luminosity density distribution in the models and in real galaxies. Thus, we are only interested in the determination of the Sersic parameter m . In particular, we recall here that throughout this work we *do not* use any measure of effective radius obtained with surface brightness profile fitting. Indeed, when discussing the scaling relations involving the effective radius, we always measure it as the circularized radius of the effective isophote $\langle R \rangle_e$, as given in equation (A.13), independently of any luminosity profile fitting.

As well known, the best-fitting value of the Sersic parameter m , for a given observed galaxy or galaxy model, is expected to be dependent on both the details of the fitting procedures and the adopted radial range. The Sersic law is characterized by the three parameters I_0 , R_e , and m . A possible technique is to consider all these three parameter as free when looking for the best-fitting Sersic function. A different approach is to fix R_e and/or I_0 , and let m as only free parameter. This latter method is possible because, as pointed out above, the effective radius can be measured independently, and, in addition, we know the total luminosity of our N -body models. Thus, using equation (A.16), we can write I_0 as a function of m of R_e .

We performed several tests, fitting both the initial spherical γ -models and the end-products, for various choice of the number of free parameters. In general, we find that the best-fitting values of m are not very sensitive to the adoption of fixed or free R_e and I_0 . As a rule, in order to determine m for our models, we perform the fits using as free parameters both I_0 and R_e , besides m .

The situation is different when the effects of the adopted radial range are considered. As a result of our tests, we find that in any case the best-fitting values of m are quite dependent on the radial range. For example, for the spherical $\gamma = 1$ model $m = 2.6$ turns out to be the best-fitting value of the Sersic parameter, over the radial range $0.1 \lesssim R/\langle R \rangle_e \lesssim 4$ (adopted in Chapter 5), with $\langle \Delta\mu \rangle = 0.08$ and $(\Delta\mu)_{\max} = 0.19$, while $m = 3.5$ over $0.1 \lesssim R/\langle R \rangle_e \lesssim 10$ (adopted in Chapters 6 and 7), with $\langle \Delta\mu \rangle = 0.15$ and $(\Delta\mu)_{\max} = 0.33$.

Acknowledgments

I would like to acknowledge the contributions of all those who have helped me with this work.

Special thanks to Luca Ciotti, for everything and in particular for his *fundamental* lessons, and to Pasquale Londrillo, for his help and for *numerous* reasons. I am also grateful to Massimo Stiavelli, my guide at STScI. In addition, I would like to thank Andrew Benson, Reinaldo de Carvalho, Walter Dehnen, Myriam Gitti, Oleg Gnedin, Barbara Lanzoni, Silvia Pellegrini, Lucia Pozzetti, Andrea Riciputi, Piero Rosati, Giancarlo Setti, Tommaso Treu, Cristian Vignali, Marta Volonteri.

Others (for their good luck) have not been involved directly with my thesis, my simulations and so on, but they have been very important for this work. Thus, I thank all those, at Dipartimento and Osservatorio (in Bologna), and STScI (in Baltimore), who have helped me during these years. My former and present flatmates (“The Brothers”). My wonderful family: Angela, Piero, Maria and Bernardo. Finally, Silvia: for having patience.

Bibliography

- Aarseth S.J., Henon M., Wielen R., 1974, A&A, 37, 183
- Athanassoula E., Fady E., Lambert J. C., Bosma A., 2000, MNRAS, 314, 475
- Barnes J. E., Hut P., 1986, Nature, 324, 446 (BH86)
- Barnes J. E., Hut P., 1989, ApJS, 70, 389
- Barnes J. E., 1992, ApJ, 393, 484
- Baugh C.M., Cole S., Frenk C.S., 1996, MNRAS, 283, 1361
- Begelman M.C., Blandford R.D., Rees M.J., 1980, Nature, 287, 307
- Bekki K., 1998, ApJ, 496, 713
- Bender R., 1988, A&A, 193, 7
- Bender R., Burstein D., Faber S. M., 1992, ApJ, 399, 462 (BBF92)
- Bender R., Burstein D., Faber S. M., 1993, ApJ, 411, 153
- Bender R., Saglia R.P., Ziegler B., et al., 1998, ApJ, 493, 529
- Bernardi M. et al., 2003, preprint (astro-ph/0301624)
- Bertin E., Arnouts S., 1996, A&AS, 117, 393
- Bertin G., 2000, Dynamics of Galaxies, Cambridge University Press, Cambridge
- Bertin G., Stiavelli M., 1989, ApJ, 338, 723
- Bertin G., Pegoraro F., Rubini F., Vesperini E., 1994, ApJ, 434, 94
- Bertin G., Ciotti L., Del Principe M., 2002, A&A, 386, 1491
- Binney J., Tabor G., 1995, MNRAS, 276, 663
- Binney J., Tremaine S., 1987, Galactic Dynamics, Princeton University Press, Princeton
- Bower R. G., Lucey, J.R., Ellis R.S., 1992, MNRAS, 254, 601
- Burstein D., Davies R.L., Dressler A., Faber S.M., Lynden-Bell D., 1988. In: *Towards understanding galaxies at large redshift; Proceedings of the Fifth Workshop of the Advanced School of Astronomy*, Dordrecht, Kluwer Academic Publishers.
- Caon N., Capaccioli M., D'Onofrio M., 1993, MNRAS, 265, 1013
- Capelato H.V., de Carvalho R.R., Carlberg, R.G., 1995, ApJ, 451, 525
- Capuzzo-Dolcetta R., Mocchi P., 1998, Journal of Computational Physics, 143 , 29
- Carollo C.M., Danziger I.J., Buson L., 1993, MNRAS, 265, 553
- Carollo C.M., de Zeeuw P.T., van der Marel R.P., 1995a, MNRAS, 276, 1131
- Carollo C.M., de Zeeuw P.T., van der Marel R.P., Danziger I.J., Qian E.E., 1995b, ApJ, 441, L25
- Ciotti L., 1991, A&A, 249, 99

- Ciotti L., 1994, *Celestial Mechanics & Dynamical Astronomy*, 60, 401
- Ciotti L., 1996, *ApJ*, 471, 68
- Ciotti L., 1997. In: *3rd ESO-VLT Workshop - Galaxy Scaling Relations: Origins, Evolution and Applications*, L. da Costa and A. Renzini eds., Dordrecht, Kluwer.
- Ciotti L., 1999, *ApJ*, 520, 574
- Ciotti L., Bertin G., 1999, *A&A*, 352, 447
- Ciotti L., Lanzoni B., 1997, *A&A*, 321, 724 (CL97)
- Ciotti L., Ostriker J.P., 1997, *ApJ*, 487, L105
- Ciotti L., Ostriker J.P., 2001, *ApJ*, 551, 131
- Ciotti L., van Albada, T.S., 2001, *ApJ*, 552, L13 (CvA01)
- Ciotti L., Lanzoni B., Renzini A., 1996, *MNRAS*, 282, 1
- Ciotti L., Stiavelli M., Braccesi A., 1995, *MNRAS*, 276, 961
- Cole, S., Lacey, C.G., 1996, *MNRAS*, 281, 716
- Cole, S., Lacey, C.G., Baugh, C.M., Frenk, C.S., 2000, *MNRAS*, 319, 168
- Crone M.M., Evrard A.E., Richstone D.O., 1994, *ApJ*, 434, 402
- Dantas C.C., Capelato H.V., Ribeiro A.L.B., de Carvalho R.R., 2003, preprint (astro-ph/0211251)
- Davies R.L., Efstathiou G., Fall S.M., Illingworth G., Schechter P.L., 1983, *ApJ*, 266, 41
- Dehnen W., 1993, *MNRAS*, 265, 250
- Dehnen W., 2000, *ApJ*, 536, L39
- Dehnen W., 2001, *MNRAS*, 324, 273
- Dehnen W., 2002, *Journal of Computational Physics*, 179, 27 (D02)
- de Vaucouleurs G., 1948, *Ann. d'Astroph.*, 11, 247
- de Zeeuw T., 2001, in *Black Holes in Binaries and Galactic Nuclei*, Proceedings of the ESO Workshop held at Garching, Germany, 6-8 September 1999, ESO Astrophysics Symposia (Springer), 78
- de Zeeuw T., Franx M., 1991, *ARA&A*, 29, 239
- Djorgovsky M., Davis S., 1987, *ApJ*, 313, 59
- Dressler A., 1984, *ARA&A*, 22, 185
- Dressler A., Lynden-Bell D., Burstein D., Davies R.L., Faber S.M., Terlevich R., Wegner G., 1987, *ApJ*, 313, 42
- Eggen O.J., Lynden-Bell D., Sandage A.R., 1962, *ApJ*, 136, 748
- Evstigneeva E.A., Reshetnikov V.P., Sotnikova N.Y., 2002, *A&A*, 381, 6
- Faber S.M., Jackson R.E., 1976, *ApJ*, 204, 668

- Ferrarese L., 2002, preprint (astro-ph/0203047)
- Ferrarese L., Merritt D., 2000, ApJ, 539, L9
- Fisher D., Franx M., Illingworth G., 1995, ApJ, 448, 119
- Flanagan E.E., Hughes S.A., 1998, PhRvD, 57, 4535
- Fridman A. M., Polyachenko V.L., 1984, Physics of Gravitating Systems (Springer, New York) (FP84)
- Gebhardt K. et al., 2000, ApJ, 539, L13
- Gerhard O., Kronawitter A., Saglia R.P., Bender R., 2001, AJ, 121, 1936
- Ghigna S., Moore B., Governato F., Lake G., Quinn T., Stadel J., 1998, MNRAS, 300, 146
- Gonzalez-Garcia A.C., van Albada T.S., 2003, submitted
- Graham A., Colless M., 1997, MNRAS, 287, 221
- Graham A.W., Erwin P., Caon N., Trujillo L., 2001, ApJ, 563, L11
- Greengard L., Rokhlin V., 1987, Journal of Computational Physics, 73, 325
- Greengard L., Rokhlin V., 1997, Acta Numerica, 6, 229
- Haehnelt M.G., Kauffmann G., 2000, MNRAS, 318, L35
- Haehnelt M.G., Kauffmann G., 2002, MNRAS, 336, 61
- Hartwick F.D.A., Schade D., 1990, ARA&A, 28, 437
- Hausman M.A., Ostriker J.P., 1978, ApJ, 224, 320
- Hernquist L., 1987, ApJS, 64, 715
- Hernquist L., 1990, ApJ, 356, 359
- Hernquist L., 1993, ApJ, 409, 548
- Hockney R.W., Eastwood J.W., 1981, Computer Simulation Using Particles, McGraw-Hill, New York
- Hughes S.A., Blandford R.D., 2002, preprint (astro-ph/0208484)
- Jaffe W., 1983, MNRAS, 202, 995
- Jørgensen I., Franx M., Kjærgaard P., 1996, MNRAS, 280, 167 (JFK96)
- Kauffmann G., 1996, MNRAS, 281, 487
- King I.R., 1966, AJ, 71, 64
- Koopmans L.V.E., Treu T., 2003, ApJ, 583, 606
- Kormendy J., 1977, ApJ, 218, 333
- Kormendy J., Richstone D., 1995, ARA&A, 33, 581
- Labbé I. et al., 2002, preprint (astro-ph/0212236)

- Laine S., van der Marel R.P., Lauer T.R., Postman M., O'Dea C.P., Owen F.N., 2003, AJ, 125, 478
- Larson R.B., 1975, MNRAS, 173, 671
- Lauer T.R. et al., 2002, AJ, 124, 1975
- Londrillo P., Nipoti C., Ciotti L., 2003, in press (astro-ph/0212130)
- Magorrian J. et al., 1998, AJ, 115, 2285
- Malumuth E.M., Kirshner R.P., 1981, ApJ, 251, 508
- Malumuth E.M., Kirshner R.P., 1985, ApJ, 291, 8
- Malumuth E.M., Richstone D.O., 1984, ApJ, 276, 413
- Matthews T. A., Morgan W.W., Schmidt M., 1964, ApJ, 139, 781
- Merritt D., 1984, ApJ, 276, 26
- Merritt D., 1985, AJ, 90, 102
- Merritt D., 1996, AJ, 111, 2462
- Merritt D., Aguilar L.A., 1985, MNRAS, 217, 787
- Merritt D., Ekers R.D., 2002, Science, 297, 1310
- Merritt D., Ferrarese L., 2001, Apj, 547,140
- Merritt D., Trembley B., 1994, AJ, 108, 514
- Meza A., Zamorano N., 1997, AJ, 490, 136
- Meza A., Navarro J.F., Steinmetz M., Eke V.R., 2003, preprint (astro-ph/0301224)
- Mihos J.C., Hernquist L., 1994, ApJ, 437, L47
- Miller G.E., 1983, ApJ, 268, 495
- Milosavljevic M., Merritt D., 2001, ApJ, 563, 34
- Naab T., Burkert A., Hernquist L., 1999, ApJ, 523, L133
- Navarro J.F., Frenk C.S., White S.D.M. 1996, ApJ, 462, 563
- Nipoti C., Londrillo P., Ciotti L., 2002, MNRAS, 332, 901 (NLC02)
- Nipoti C., Londrillo P., Ciotti L., 2003a, MNRAS, in press (astro-ph/0302423) (NLC03a)
- Nipoti C., Londrillo P., Ciotti L., 2003b, in *The Mass of Galaxies at Low and High Redshift*, Proceedings of the ESO Workshop held in Venice, Italy, 24-26 October 2001, R. Bender and A. Renzini eds (Berlin: Springer), 70 (NLC03b)
- Nipoti C., Stiavelli M., Treu T., Ciotti L., Rosati P., 2003c, MNRAS, submitted
- Oegerle W.R., Hoessel J.G., 1991, ApJ, 375, 150
- Osipkov L.P., 1979, Soviet Astron. Lett., 5, 42
- Ostriker J.P., Tremaine S.D., 1975, ApJ, 202, L13

- Pahre M.A., de Carvalho R.R., Djorgovski S.G., 1998, AJ, 116, 1606
- Pahre M.A., Djorgovski S.G., de Carvalho R.R., 1998, AJ, 116, 1591
- Peebles P. J. E., 2002, preprint (astro-ph/0201015)
- Peletier R., 1989, PhD thesis, Univ. Groningen
- Pentericci L., Ciotti L., Renzini, A., 1995, Astrophysical Letters and Communications, 33, 213
- Prugniel P., Simien F., 1997, A&A, 321, 111
- Quinn T., Katz N., Stadel J., Lake G., 1997, preprint (astro-ph/9710043)
- Renzini A., Ciotti L., 1993 ApJ, 416, L49
- Ricotti M., 2002, preprint (astro-ph/0212146)
- Saha P., 1991, MNRAS, 148, 494
- Saha P., 1992, MNRAS, 254, 132
- Sarazin C.L., 1986, Rev. Mod. Phys., 58, 1
- Schneider D.P., Gunn J.E., Hoessel J.G., ApJ, 268, 476
- Sellwood J.A., 1983, Journal of Computational Physics, 50, 337
- Sersic J.L., 1968, Atlas de galaxias australes. Observatorio Astronomico, Cordoba
- Spitzer L., 1969, ApJ, 158, L139
- Springel V., Yoshida N, White S.D.M., 2001, New Astronomy, 6, 79 (SYW01)
- Stiavelli M., Sparke L.S., 1991, ApJ, 382, 466
- Subramanian K., Cen R., Ostriker J.P., 2000, ApJ, 538, 528
- Tabor G., Binney J., 1993, MNRAS, 263, 323
- Tonry J.L., 1987, IAUS, 127, 89
- Treu T., Stiavelli M., Casertano S., Moeller P., Bertin G., 1999, MNRAS, 308, 1037
- Treu T., Stiavelli M., Møller P., Casertano S., Bertin G., 2001, MNRAS, 326, 221
- Treu T. et al., in preparation
- Tremaine S., Richstone D.O., Yong-Ik B., Dressler A., Faber S.M., Grillmair C., Kormendy J., Laurer T.R., 1994, AJ, 107, 634
- Tremaine S. et al. 2002, ApJ, 574, 740
- van Albada, T.S., 1982, MNRAS, 201, 939
- van der Marel, R.P., 1999, AJ, 117, 744
- van der Marel R.P., Magorrian J., Carlberg R.G., Yee H.K.C., Ellingson E., 2000, AJ, 119, 2038
- van Dokkum P., Franx M., 1996, MNRAS, 281, 985

- van Dokkum P.G., Franx M., Fabricant D., Kelson D.D., Illingworth G.D., 1999, ApJ, 520, 95
- Volonteri M., Haardt F., Madau P., 2003, ApJ, 582, 559
- White S.D.M., 1980, MNRAS, 191, 1
- White S.D.M., Rees M.J., 1978, MNRAS, 183, 341
- Yu Q., 2002, MNRAS, 331, 953
- Zhang B., Wyse R.F.G., Stiavelli M., Silk J., 2002, MNRAS, 332, 647
- Ziegler B.L., Saglia R.P., Bender R., Belloni P., Greggio L., Seitz S., 1999, A&A, 346, 13

Related publications

With referee

1. **Nipoti C.**, Londrillo P., Ciotti L., “*Radial orbital anisotropy and the Fundamental Plane of elliptical galaxies*”, 2002, MNRAS, 332, 901
2. **Nipoti C.**, Londrillo P., Ciotti L., “*Galaxy merging, the Fundamental Plane of elliptical galaxies and the $M_{\text{BH}} - \sigma_0$ relation*”, 2003, MNRAS, in press (preprint: astro-ph/0302423)
3. **Nipoti C.**, Stiavelli M., Ciotti L., Treu T., Rosati P., “*Galactic cannibalism in the galaxy cluster C0337-2522 at $z \simeq 0.59$* ”, 2003, submitted to MNRAS

Without referee

1. **Nipoti C.**, Londrillo P., Ciotti L., “*Galaxy merging and the Fundamental Plane of elliptical galaxies*”, 2002, in *The Mass of Galaxies at Low and High Redshift*, Proceedings of the ESO Workshop held in Venice, Italy, 24-26 October 2001, R. Bender and A. Renzini eds (Berlin: Springer), 70
2. Londrillo P., **Nipoti C.**, Ciotti L., “*A parallel implementation of a new fast algorithm for N-body simulations*”, 2002, in “Computational astrophysics in Italy: methods and tools”, Proceedings of the workshop, Bologna, July 4-5, 2002, R. Capuzzo Dolcetta ed., SAI Proc. on line, in press (preprint: astro-ph/0212130)

